

Gauge Invariant Spectral Cauchy Characteristic Extraction of Gravitational Waves in Computational General Relativity

Thesis by

Casey J. Handmer

In Partial Fulfillment of the Requirements

for the Degree of

Doctor of Philosophy



California Institute of Technology

Pasadena, California

2016

(Defended May 14, 2015)

© 2016

Casey J. Handmer

All Rights Reserved

Theoretical Astrophysics 350-17
California Institute of Technology
Pasadena California 91125 USA
casey.handmer@gmail.com

Acknowledgements

Alison, Bruce, Marcus, Annie — you are my bedrock support from across the sea. Come visit more often. Marilyn, Tim, Walter, Norma, Roz, Poppy, Rosemary — profound examples of astonishing careers and courage in the face of adversity. John, Amanda, Tom, Hannah, Ginny, Jeff, Noah, Tessa, Bryn, Josh, Alex, Georgie, Suzie, Charles, Sheena, Andrew, Lindsay, Jay, Chris, Judy, Alistair, Christina, John, Ramona — you can choose your friends but you can't choose your family. Most of you remind me that there are reasons to return to the old country, and some of you are participating in the infiltration of this one.

Amy, Ben, Holly, Lisa, Ken, Esteban, Peter, Oliver, Ramla, Kate, Michael, Joel, Kathy, Artemis, thanks for sharing a roof and scheming of a work-life balance, and Dustin, Ananda, Branimir, Wilton, Kris, for hanging out enough to make housing suspicious.

J, K, C, T, S, P, for putting up with me and teaching me the most important lessons.

Ed, Bruce, Mary Anne, Stef, Jony, Cat, Lisa, Giles, Andrew, Elly, Ricky, Chris, Deon, Lily, for visiting from far away lands. Sam, for being the other Australian, especially on election day. Bruce, Suzie, Katie, Audrey — family by another mother on the east coast.

I have had the privilege of teaching the smartest, most wonderful children of the 1990s during my time at Caltech, too many to list by name. Like a terse compiler, each holds up a mirror to my alleged logic and thought, a constant and invaluable challenge to simplify and unify knowledge.

My intrepid advisers/colleagues/committee Mark, Béla, Jeff, Yanbei, Christian, Christian, Dan, Tom, Frank, Gil, Sterl, Ryan, Alan, when I needed help you were there to provide it, in one way or another. Dealing with me is not always easy, and your patience, generosity, expertise, and example were invaluable.

Kip, for making Caltech gravity what it is, and for hosting the most excellent parties. Libby and Alex, for the example of a life of generosity and agitation. Roger,

for getting the whole thing started. The team at the Australian Physics Olympiad, for pushing it along.

My fellow TAPIRs. Kevin, Jonathan, Joshua, Hannalore, Matthew, Sarah, Dávid, Bassam, Io, John, Kristen, Jonas, Jing, Belinda, Xiangcheng, Zach, Keith, Abhilash, Antonija, Masha, Sherwood — what a privilege and pleasure to spend time with such brilliant people!

My Öcsi Bácsi brothers and sisters — David, Aaron, Jeff, Teja, Lena. Much more I cannot say.

Donna, Chris, Laura, Dan, Ken, JoAnn, Shirley, Alice, Divina, Jeannie — your support made all the difference at the most crucial times. Thank you for going out of your way to help me!

Felicia and Joe, thank you for keeping your eye on the ball. It's not easy to be the person who no one ever approaches with a small problem.

To my colleagues in the geology department: your wit and charm, large white SUVs, and limitless supplies of pasta, passion for rocks, and empiricism served to remind me what academia was all about. Joe, thank you for Ge136 and Martian magnetite. Your example of generosity and gentlemanly science is a model and inspiration. Frank, Max, Steve, Sean, Sarah, Hayden, Jason, Monica, Suzanne, Connor, and all the other TAs/regulars: I wish I could be as cool. Classmates too numerous to name, you kept me awake on long drives and let me borrow your handouts.

To my colleagues in the aero department, who do work that is both fun and useful: Melanie, Heather, Ilana, Yamuna, Thibaud, Niko, Hayden, Jay, I want to make things fly! Stephanie, Utkarsh, Paraj, and the band of merry astronomers Jackie, Mike, Seb, Sirio, Swarnima, what would Caltech be like without you?

Friends in Fluid Dynamics, my family at Caltech. Emma, Marissa, June, Kevin, Kenzie, Eric, Sarah, Chris, Jetson, Will, Jeff, Kim, Alina, Juliet, Peter, David, Tara, NotKevin, Sandhya, Irene, Ninj, Roel, Emily, Sanji, Shyam, Sally, Kelvin, Lucy, Catherine, Graham, Alex, Ashwin, Tiffany, Audrey: I moved house seven times, switched version control software, grew grey hairs, and still saw all of you for two hours, three times a week, week after week, year after year. We are now older and a

little wiser, and it is time for me to make room for younger blood!

Hamik, Lauren, Kedron, BG, PT, Raphaela, Patrick, Dan, Danielle, Rich, Robb, Nick, Eyrún, Stephen, Bryan, Danica, and all the rest in the Caltech Alpine Club: finer people with whom to race suffocation and freezing to death I cannot imagine.

Russ, for showing me how to fly, and my various passengers for braving the heights.

The Caltech theatre program, for nearly reducing my productivity to zero in the best possible way. Jordan, Supriya, Dan, Holly, Alex, Lynne, Christine, Annette, Sophie, Ben, Jan, Jon, Daniel, Alex, Crystal, Meg, Kim, Teek, Ben, Klavdia. How good was *Little Shop of Horrors*? Alexis, Achiamar, Daniel, Giulia, Penelope, Larissa, Erisa, Elizabeth, Dan, Tiff, Harrison, Becky, Paul, Kristine, Melany, Julia, Emily, Angela, Evan, Brenda, Manan, Steve, Amit, Lindsay, Kari, Cierina, Jasmine, Andre, Megan, Amit, Peabo. *RENT* rocked! And you wonderful recidivists, Ed, Stella, Doug, Miranda, Brian, Teagan, Missy, Andy, Andy, Elena, Zach, Kayla, Dave, Ella, Anne, Marty: I aspire to equivalent levels of greatness.

To my fellow leaders in the Caltech Y, Jeremy, Dorothy, Howard, Becky, Koen, Dan, Kevin, Tess, Sharon, Laura, Katja, and the staff Greg, Athena, Liz, Amy, Camila, Chris: too many adventures to name, but what wonderful opportunities for service, growth, and sharing the love of nature.

To my supportive editors at The California Tech. Neera and Nehaly Shah, and Stanford and Jonathan Schor: your encouragement and editorial prowess continues to inspire me. I will never write for non-identical twins again.

Vladimir, your book “*Dragon Songs*” about your PhD both inspired me and helped me to keep my challenges in perspective.

To Shaun, Matthew, David, Dan, and all the rest: your generosity and infectious excitement made *Coup de Foudre* and the entire *Burn* such a wonderful experience.

Abstract

We present a complete system for Spectral Cauchy characteristic extraction (Spectral CCE). Implemented in C++ within the Spectral Einstein Code (SpEC), the method employs numerous innovative algorithms to efficiently calculate the Bondi strain, news, and flux.

Spectral CCE was envisioned to ensure physically accurate gravitational waveforms computed for the Laser Interferometer Gravitational wave Observatory (LIGO) and similar experiments, while working toward a template bank with more than a thousand waveforms to span the binary black hole (BBH) problem's seven-dimensional parameter space.

The Bondi strain, news, and flux are physical quantities central to efforts to understand and detect astrophysical gravitational wave sources within the Simulations of eXtreme Spacetime (SXS) collaboration, with the ultimate aim of providing the first strong field probe of the Einstein field equation.

In a series of included papers, we demonstrate stability, convergence, and gauge invariance. We also demonstrate agreement between Spectral CCE and the legacy Pitt null code, while achieving a factor of 200 improvement in computational efficiency.

Spectral CCE represents a significant computational advance. It is the foundation upon which further capability will be built, specifically enabling the complete calculation of junk-free, gauge-free, and physically valid waveform data on the fly within SpEC.

Contents

| | |
|--|------|
| Acknowledgements | iii |
| Abstract | vi |
| List of Figures | viii |
| Statement of Originality | 1 |
| Advisers | 2 |
| What does this thesis contain? | 2 |
| Chapter 1 – Gravitational waves? | 3 |
| A general introduction | 3 |
| A technical introduction | 6 |
| Chapter 2 – Technical note on data presentation | 13 |
| Chapter 3 – Characteristic evolution | 15 |
| Chapter 4 – Gauge free Bondi news | 55 |
| Chapter 5 – Strain, news, and flux | 92 |
| Chapter 6 – Current Status of Spectral CCE Project | 139 |
| Chapter 7 – Avenues of future research | 142 |
| Appendix A – Fourier Continuation in SpEC | 143 |

List of Figures

| | | |
|---|--|-----|
| 1 | Coordinate compactification. | 9 |
| 2 | Cauchy and characteristic evolution. | 10 |
| 3 | Typical convergence graph. | 13 |
| 4 | Screen cap from CQG+ website. | 17 |
| 5 | Diagram of Spectral CCE compute item dependencies. | 139 |
| 6 | Commit History. | 140 |

Statement of Originality

This section lays out precisely by whom contributions were made. This section is sufficiently detailed that reference to the code repository might be necessary for perfect resolution.

The main innovations in the development of Spectral CCE were the use of a Laurent expansion and a Magnus expansion to numerically solve the Bondi hypersurface equations. The adaptation of these analytic complex analysis methods to numerics is an unusual and surprisingly effective method. I performed the calculations, coding, and testing completely for both of these methods. Yanbei Chen helped confirm the result of one calculation in an earlier iteration of the method.

Implementation of the numerics in Spectral CCE was a collaborative effort with Béla Szilágyi, who has since moved to JPL. His contribution cannot be overstated—without his patience I would not have learned enough of `SpEC` and C++ to get very far. In the final code, Béla implemented the `worldtube` file reader, the `SphericalShellsSW` coordinate map, and the indefinite integral virtual base class. I greatly modified and debugged all of these routines, which function at the interface of my code and the rest of `SpEC`.

The remainder of the approximately 200 C++ files (totalling around 20,000 lines) in the `Characteristic` directory were written, tested, and debugged by me, with occasional help from Béla. The `sYlmSpinsfast` and `FourierContinuation` basis functions were also implemented by me, and built upon, respectively, the `Spinsfast` and `fftw` transform libraries.

The `Characteristic Observers` routine was written by Dan Hemberger. Mark Scheel wrote the `MultiVars` module, which allows simultaneous evolution of different drivers and will eventually permit Spectral CCE to be run in tandem with `SpEC`'s Cauchy evolution. Jonathan Blackman contributed to the domestication of the input files scheme necessary to run Spectral CCE.

All new mathematical formalism for inertial strain, news, and flux was developed by Jeffrey Winicour, with some contributions to design, rigor, and correctness by me.

Advisers

Christian Ott (2010-2013)

Yanbei Chen (2013-2015)

What does this thesis contain?

This thesis begins with a general introduction to the gravitational wave extraction problem in Chapter 1, followed by a brief discussion of the presentation of convergence data in Chapter 2.

Chapters 3 through 5 present papers containing the core results of this thesis. Each chapter begins with a short introduction to motivate and contextualize the subject matter. The papers have their own subject-specific introductions and provide relevant citations.

Chapter 6 discusses the current status of the Spectral Cauchy characteristic extraction project, while Chapter 7 lays out a roadmap for future work in the area.

Finally, Appendix A discusses the implementation of the Fourier Continuation basis function in SpEC, which was not used in the final characteristic extraction module.

Some additional published research conducted in parallel to work on Cauchy characteristic extraction included work on optimizing high speed transport networks using genetic algorithms, which can be found at <http://arxiv.org/abs/1503.01524>, and hazards to Earth orbiting satellites from captured asteroid disruption in distant Lunar retrograde orbits, which can be found at <http://arxiv.org/abs/1505.03800>.

Chapter 1 – Gravitational waves?

A general introduction

Black holes are perhaps one of the most surprising discoveries of all time. Initially predicted on the basis of pure logic, their later astrophysical discovery attests to the strangeness of our universe. So peculiar, so foreign to our intuition, are these mysterious and distant entities that even now, after nearly a century of formal study, we are still learning about them.

All objects with mass exert a mutual gravitational pull. Newton's discovery of the underlying mathematical relation showed that gravity is the same force, whether it propels a dropped hammer onto one's foot or holds the galaxy together. The Earth exerts a gravitational pull on us, satellites, the moon, and everything else in the universe. When NASA sends a robot to Mars, it must be launched on a rocket at a speed that is fast enough to escape Earth's pull forever. That speed is 11.2 km/s, roughly 25,000 mph. This speed is known as an escape velocity - provided you can travel faster, you can escape that planet or star.

When stars larger than ten of our suns end their relatively short, violent lives they form a black hole. Lacking thermal and light pressure to counteract their enormous gravity, they collapse to a density where their escape velocity exceeds the speed of light. There is effectively a surface, a place in space, where light can only just escape. This is known as the "event horizon," as observers outside the black hole can never see what happens inside. Indeed, we are causally disconnected.

The gravity of a black hole is so strong it is an ideal laboratory for testing our physical theories. Gravity is described by Einstein's General Theory of Relativity, one of the most successful predictive theories of all time, together with the Standard Model of particle physics. The Standard Model describes every physical thing we can see, except gravity. Physicists have been unable to conclusively combine the two into a single unifying framework — the holy grail of physics. A better understanding of General Relativity can only come from tests in the strongest gravity possible — a black hole.

Black holes are, all things considered, rather small. For black holes resulting from the death of big stars, up to ten times more massive than our sun, a size of a few kilometers is typical. The best telescopes aren't (yet!) able to clearly resolve the event horizon of known black holes in our galaxy.

Incredibly, black holes warp space and time to such an extent that when perturbed they generate measureable gravitational radiation. Radio waves and light represent oscillations of the electromagnetic field, and are the primary means by which astronomers can observe stars and galaxies. Gravitational waves represent oscillations in the gravitational field, and we hope to use them to infer things about black holes and other astrophysical cataclysms we cannot directly observe.

An electromagnetic wave is an interacting thicket of transient electric and magnetic fields, which can be detected with a dipole antenna, which is basically a wire containing free electrons. Similarly, gravitational waves manifest as transient gravitational fields changing as a quadrupole stretching and squeezing of spacetime. Experimenters have built a series of large quadrupole antenna detectors designed to observe gravitational waves. The Laser Interferometer Gravitational Wave Observatory (LIGO) and its sister detectors around the world are designed to detect rapid but minute stretching and squeezings — equivalent to the entire Earth squeezing by less than the width of a proton a few hundred times a second. LIGO is currently undergoing a series of upgrades and is expected to reach design sensitivity and full detection capability later in 2015.

LIGO's detection capability is enhanced through the use of matched filtering, wherein actual (noisy) data is compared with an expected waveform, to improve the signal to noise ratio. The research in this thesis has been part of the effort to compute a comprehensive catalogue of waveforms with which to scour LIGO's data in search of events.

Generating waveforms requires a computational simulation of the expected event. This thesis focuses on waveforms generated by binary black hole events, where two black holes inspiral, then merge into a single black hole which subsequently rings down like a struck bell. The Simulating Extreme Spacetimes collaboration has developed

the Spectral Einstein Code (**SpEC**), a very powerful program that can simulate a black hole binary merger on a super computer cluster in only weeks.

The main problem that this thesis seeks to address is one of waveform validity. **SpEC**'s computational domain is necessarily finite and waveforms generated directly from its output data are contaminated by gauge effects, technical “noise” associated with the “gauge freedom” of coordinate systems in General Relativity. The computational domain's coordinate system has to respond dynamically — the gauge — to the shifting coordinate system to avoid getting sucked into the black holes it is simulating. As a result, the coordinates get shaken by outgoing gravitational radiation — the gauge effect.

In more detail, simulations of General Relativity are typically performed by splitting the equations into three spatial dimensions and one time dimension (“3+1”). Complete field information is specified throughout the 3D volume at a particular time (the “time slice”) and used to calculate a derivative, from which the next time slice can be computed. Because General Relativity mixes space and time, a simulation has to specify how one (3D) time slice fits onto the next, parameterized by the quantities known as “time lapse” and “spatial coordinate shift.” The simplest choice corresponds to a lapse of one and a shift of zero. This is termed “geodesic gauge” as coordinates follow the path of inertial observers (geodesics).

Free falling inertial observers quickly fall inwards and vanish behind the event horizon, so another choice must be made. **SpEC** uses a gauge termed “damped harmonic” but, as a dynamically evolved coordinate system, it is sensitive to local conditions. Sailors cast about in terrible seas are notorious for overestimating the size of waves, and **SpEC**'s gauge contaminated waveforms suffer a similar problem. Unable to tell the difference between a relatively slowly varying background gravitational field and gravitational waves, the coordinate system is wiggled by the radiation. While the simulation is no less physically valid, waveforms derived from such a coordinate system are contaminated by this non-inertial coordinate motion, and must be fixed to be useful for physical investigations using matched filtering.

This thesis demonstrates a method to remove gauge contamination and other

confounding factors by propagating the gravitational waves to a point infinitely far away and, thus, infinitely far in the future, a point termed “future null infinity,” or \mathcal{I}^+ . This method, called Spectral Cauchy characteristic extraction (CCE), is a substantial improvement over previous attempts and also permits calculation of other physically interesting quantities.

The principal quantities we obtain from Spectral CCE are the strain, the Bondi news, Ψ_4 , and various fluxes. The strain (h) is the quantity measured by LIGO, the degree to which spacetime is actually stretched and warped by a gravitational wave, by an observer very far from the source. The Bondi news (N) is equivalent to an inertial time derivative of the strain and represents the flux of energy. Inertial time derivative refers to an operation carried out in an unaccelerated, inertial frame. Ψ_4 is technically defined as a part of the Weyl (conformal) curvature tensor at \mathcal{I}^+ , but is also equivalent to the inertial time derivative of the news. In summary, $\Psi_4 = N_{,\bar{u}} = h_{,\bar{u}\bar{u}}$.

Various fluxes represent the flow of conserved quantities corresponding to various symmetries. In brief, they are generated by one time translation — energy, three space translations — momentum, three rotations — 3D angular momentum, and three Lorentz boosts — boost angular momentum. Together, they represent important quantities to track for the study of the physical dynamics of black hole binary systems.

This thesis represents a substantial advance in the capability of binary black hole merger simulations using **SpEC**. Spectral CCE is robust, accurate and, above all, computationally efficient. It bridges the gap between numerical results and physically valid waveform templates; a crucial step for the detection and study of gravitational waves and their sources by the advanced detector network.

A technical introduction

Here, we shall describe the simulation architecture used in Cauchy characteristic extraction in more detail.

Near field Cauchy evolution

SpEC simulations are performed using a Cauchy evolution, a numerical technique wherein a constant time slice is given initial data and then evolved forward in time according to an evolution equation. In General Relativity, there is no unique way to pick slices of constant time. Nevertheless, the methodology is strongly analogous to a standard 3D wave equation evolution, with a carefully constructed initial condition and evolution equation for each of the coupled variables. The state at one time slice is used to compute the fields' time derivative, which in turn is used to compute the next slice.

In SpEC, the initial condition specifies two separated black holes with velocities carefully tuned to replicate the physical state of a binary black hole inspiral some time, perhaps tens of orbits or a few seconds, before merger. The initial condition can be expressed as an elliptic equation and solved to recreate a snapshot of an actual astrophysical binary. In practice, tightly bound binaries have tidal interactions and very low residual eccentricity that is difficult to solve exactly. The degree to which the initial condition solving algorithm is unable to provide a perfectly astrophysical initial condition will result in junk radiation, in which the holes rapidly radiate gravitational waves until they reach pseudo-equilibrium. Junk radiation is difficult to resolve numerically but typically only affects the very beginning of the simulation.

In SpEC, the Einstein field equations are written as 50 simultaneous coupled highly nonlinear first order partial differential equations. Time slicing is regulated by a particular gauge (damped harmonic) in which all points on a given 3D time slice (“foliation”) are space-like separated, or causally disconnected. Simulations are performed in hundreds of parallel subdomains.

The Cauchy evolution represents the pinnacle of nearly five decades of computational innovation. It is important to remember that there are no general theorems which guarantee stability and convergence for such highly coupled, nonlinear systems as binary black hole mergers in full General Relativity. Nonetheless, finite computational resources necessitate the computational domain being finite in both space and

time. Ideally, we would like to simulate the entirety of the radiative field within the Cauchy evolution to extract the most accurate waveforms. One possible approach to include spatial infinity in a finite domain is to apply a conformal transformation to compactify the space-like Cauchy foliations. Compactification is a standard procedure that uses a well-behaved function such as $r = \tan(r_{comp})$ to provide a coordinate map between a compact and an infinite domain.

For simulations with wavelike solutions, however, spatial compactification fails as an infinite number of wave crests get shoehorned into a finite domain. The compactified wavelength rapidly decreases in size beneath the Nyquist sampling limit as radius increases to infinity, resulting in a total loss of information. Additionally, the increase in spatial frequency and characteristic wave speed towards the outer boundary breaks a numerical stability requirement known as the Courant or CFL condition. The CFL condition places a limit on the time difference between adjacent foliations, regulated by the spacing of collocation points. Typically expressed as $\Delta t < a\Delta x_{min}$, a is a constant related to the wave speed, or the speed at which information is propagated across the domain. Heuristically, time slices must move more slowly than the waves they simulate to allow time for the information to propagate.

As the outer boundary of the Cauchy domain is some finite distance from the black holes, the outer boundary condition must be carefully chosen to avoid reflections which, converging on the origin, disrupt the simulation. On the outer boundary, the field is processed to suppress ingoing radiation and allow outgoing radiation to escape with a minimum of reflections. While this condition is acceptable, a method that enables a smaller Cauchy evolution domain is highly desirable if `SpEC` is to successfully compute extremely long runs of hundreds of orbits.

Far field characteristic evolution

In contrast to the Cauchy evolution, a characteristic evolution sidesteps the Nyquist limit by using a null retarded time coordinate ($u = r + t$), where spacetime foliations are null, just like a future light cone. In these coordinates, outgoing waves appear as constant across the domain, so the code doesn't have to resolve an infinite number of

waves, as shown in Fig. 1.

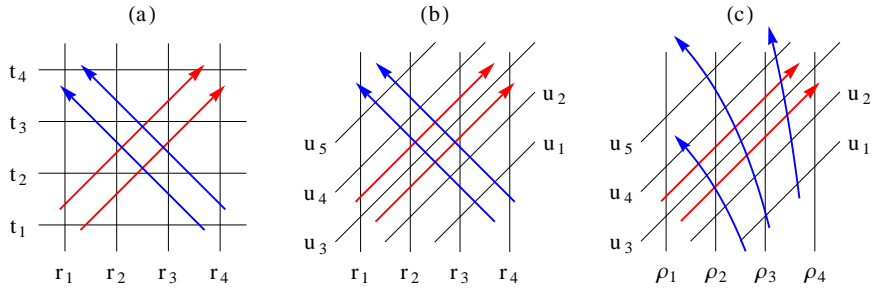


Figure 1: a) Ingoing (blue) and outgoing (red) characteristic worldlines on a radial (r) grid coordinate system. b) Retarded time ($u = r + t$) grid null coordinate parallels *outgoing* characteristics. c) Compactified null radial ($\rho = r/(R + r)$) grid coordinates bring \mathcal{I}^+ into a finite domain. Ingoing characteristics appear curved in this coordinate system.

In these coordinates the full, unabridged vacuum Einstein field equations are expressed in the Bondi form, a formalism and coordinate system that, surprisingly, permits radial spatial derivative equations for each term in the metric to be expressed in a nested, hierarchical fashion. With a conformal compactification of the radial coordinate, \mathcal{I}^+ (future null infinity) is included within the domain. Provided a mechanism for radial integration (the primary innovation presented in this thesis), a gravitational wave on the inner boundary can be readily propagated to infinity, resolving numerous issues with obtaining waveforms directly from the Cauchy evolution.

Despite the conveniences of the characteristic evolution formulation, it cannot be used to replace the Cauchy evolution by running the innermost parts of the simulation, for a variety of reasons. In particular, strong gravitational fields near the black holes lead to the formation of caustics, wherein outgoing wave characteristics collide, breaking coordinate uniqueness and resulting in a catastrophic loss of stability for any null foliated simulation. As a result, the spheroidal worldtube that forms the inner boundary of the characteristic domain must be positioned within the Cauchy domain sufficiently far from the origin to avoid caustics.

In addition to inner boundary data, the characteristic evolution also requires an initial condition. Freedom in the choice of an initial condition does affect the extracted waveform, although the structure of the characteristics typically advect the initial

condition out of the system before junk radiation passes through. We use a condition where initial boundary data is smoothly rolled off to zero at \mathcal{I}^+ , imposed at $u = 0$.

As discussed in Chapter 3, the Cauchy and characteristic evolutions can fully simulate both the strong field black hole merger and its radiation field to \mathcal{I}^+ , shown in Fig. 2.

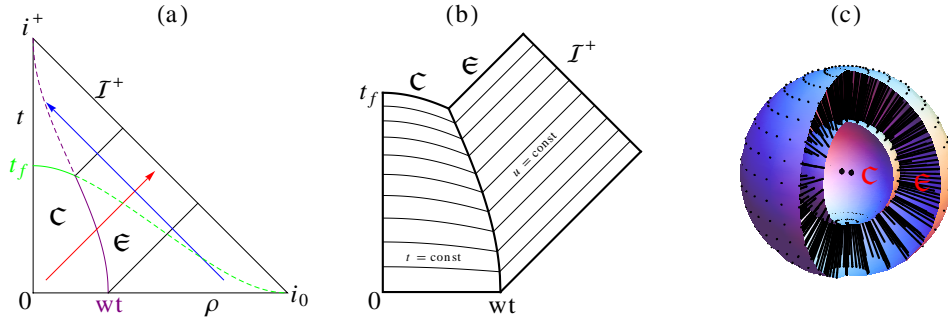


Figure 2: a) Penrose compactification of Minkowski (flat) space. The space-like foliated Cauchy evolution domain exists in the world-sphere \mathcal{C} , bounded by the worldtube “wt” and space-like global final time t_f . The null foliated characteristic evolution domain in hollow world-sphere \mathcal{E} extends the worldtube to \mathcal{I}^+ . Blue and red arrows represent ingoing and outgoing characteristics respectively. Dashed lines extrapolate constant time and radius lines to i^+ and i_0 . b) A closer look at the two computational domains with space-like foliation in \mathcal{C} and null foliations in \mathcal{E} shown for clarity. The worldtube boundary between the two domains is the extraction surface, and doesn't necessary reside on the outer boundary of the Cauchy evolution. Initial conditions are imposed at the space-like $t = 0$ and null $u = 0$ on the bottom of the diagram. c) A 3D rendering showing black radial compactified spokes with the equiangular gridpoint spacing used in our evolution.

Cauchy characteristic matching

An alternative approach at the worldtube is Cauchy characteristic matching (CCM). Instead of running the Cauchy evolution with transparent boundary conditions and later interpolating data on a virtual worldtube within the Cauchy domain, the outer boundary would be welded directly to the characteristic evolution's inner boundary. This would allow free movement of gravitational radiation in both directions across the worldtube, solving the reflection problem. Additionally, the common boundary radius could be dynamically updated during a run to balance computational loads. Additionally, CCM can help solve the initial condition without junk radiation by

stepping inwards during the initialization procedure, then resuming forward stepping. CCM has never been implemented in full generality, though the algorithms developed for this thesis are fully consistent with a CCM-specific inner boundary procedure.

Characteristic extraction of waveforms at \mathcal{I}^+

With a functional characteristic evolution system propagating metric information to \mathcal{I}^+ , it only remains to extract gauge invariant waveforms.

The coordinate system used in the characteristic evolution is derived from that at the worldtube, thus, a naive calculation of the strain, news, or any other quantity remains contaminated by gauge. The metric quantities in the characteristic coordinates must be transformed into an inertial, free falling coordinate system. Being infinitely far away, inertial coordinates can be safely used at \mathcal{I}^+ without them falling into the black holes.

It is possible to write an expression for the gauge-free inertial news in terms of the characteristic coordinates. This was first done using the Pitt null code, a finite difference Cauchy characteristic extraction code. In Chapter 4, we re-implement this method as an intermediate step and operational test, before moving entirely to the inertial coordinate system.

Characteristic extraction in the inertial frame

The inertial coordinates are co-evolved in the characteristic evolution, and permit the transformation of a contaminated conformal metric to a gauge-free inertial one according to standard procedures involving Jacobians. There is a freedom in the choice of the initial condition for the inertial coordinates, which manifests mathematically as the supertranslations: generators of asymptotic symmetries surplus to the Poincaré group. In practice, sane coordinate choices (reflecting asymptotically flat space) deliver repeatably reliable waveforms.

Once you have the inertial metric and its derivatives, one may compute a broad cornucopia of physically interesting quantities, as discussed in Chapter 5. These

quantities are termed strain, news, Ψ_4 , and fluxes. Combined, they represent complete information about a gravitational wave field measured at \mathcal{I}^+ .

The strain (what we measure) and its inertial time derivative the Bondi news (the energy) can be expressed very compactly in terms of inertial spherical metric components.

The Einstein field equations in General Relativity are expressed in terms of the Riemann curvature tensor. In four dimensions it has 20 independent components, which completely describe the local curvature of spacetime. If you subtract the trace, you are left with the 10 component Weyl curvature tensor, which is also known as the conformal tensor as it is invariant under conformal (angle preserving) transformations when expressed in the (1,3) form. The Weyl tensor contains all the curvature information at \mathcal{I}^+ , from which we can readily compute Ψ_4 , the spherical component relevant to gravitational waves.

Finally, the Spectral Cauchy characteristic formalism and algorithms permit the computation of momentum fluxes conjugate to each asymptotic symmetry. At \mathcal{I}^+ there are ten such symmetries, corresponding to the generators of the Poincaré group. Sequentially, they are time translation (energy), spatial translation (momentum), rotation (angular momentum), and Lorentz boosts, which are the relativistic equivalents of rotation that mix time and space, and represent transformations between frames with different linear velocities. Each symmetry can be expressed in terms of a field of Killing vectors on \mathcal{I}^+ , from which more general forms of the Bondi news are computed. In turn, this is combined with Ψ_4 to find the corresponding flux.

In the following chapters, I motivate and explain each result before presenting the relevant paper.

Chapter 2 – Technical note on data presentation

In numerical physics, it is customary to test accuracy and estimate error by calculating the convergence of simulations that differ only in their resolution. Increasing

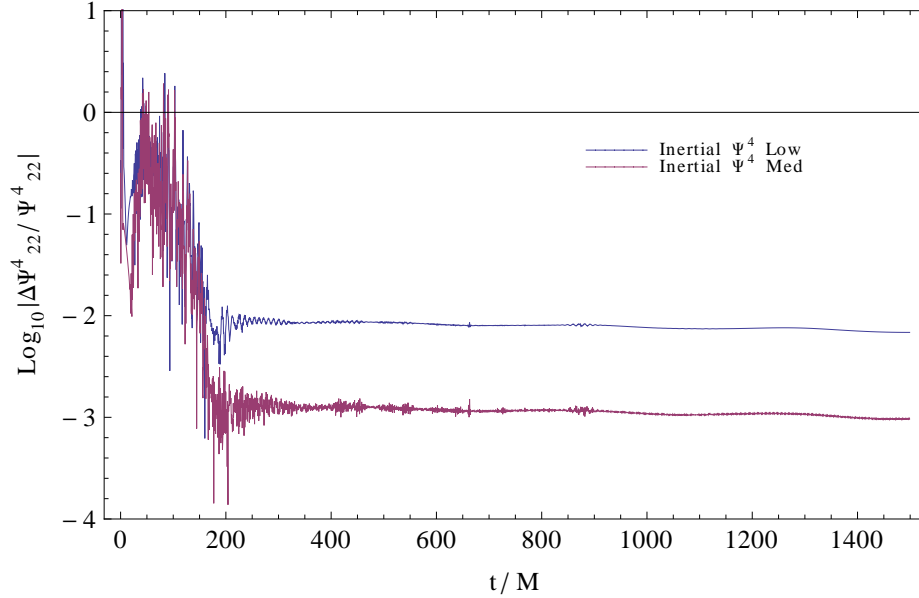


Figure 3: Typical convergence graph showing $\log_{10}(E_{rel})$ vs time t , with a consistent reduction in error for an increase in resolution. In this instance, E_{rel} is expressed as $|\Delta\Psi_{22}^4/\Psi_{22}^4|$, the absolute error in the (2,2) mode of Ψ_4 normalized by the function itself. As the highest resolution run is used to estimate the error of the medium resolution run, its own error cannot easily be estimated.

the resolution by some fixed factor α between runs yields a set of results that should be rapidly converging to the exact solution. This relative error is typically calculated by comparing the data from runs of adjacent resolutions (A_0, A_1, A_2, \dots) and normalizing, according to

$$E_i = \log_{10} \left(\frac{|A_i - A_{i+1}|}{|A_{i+1}|} \right),$$

where the resolution increases with i . Normalizing the data by dividing through by the higher resolution dataset allows consistent comparison of a signal that varies in magnitude by more than an order of magnitude, but it can be deceptive in cases where the magnitude of the signal gets very small, such as in the post-ringdown phase.

On a log scale, estimated error between adjacent resolutions should reduce by a

known factor to verify convergence at the required order. As an example, consider Fig. 3 taken from Chapter 5. After some initial noise associated with junk radiation, the graphed errors stabilize at about $10^{-2.2}$ and $10^{-2.9}$. This difference of $10^{0.7} \approx 5$ is consistent with the greatest source of error — the 4th order Runge-Kutta 4 time integrator. The medium resolution run has a timestep 50% smaller than the low resolution run, resulting in a factor $1.5^4 \approx 5$ decrease in error.

Chapter 3 – Characteristic evolution

The core of any prospective characteristic evolution code is the algorithm that performs the evolution. This algorithm solves the equations that govern General Relativity in vacuum, in the appropriate compactified null coordinate system. The equations are derived using the Bondi formulation, a simplified way of writing down the metric on a null hypersurface, and can be solved in a nested, heirarchical fashion. That is, given the spherical part of the metric on one 3D foliation, the remaining parts of the metric are reconstructed with a series of radial integrals. Once the complete metric is derived, the time derivative of the spherical part is calculated and the process begins again.

We were fortunate to have the Pitt null code, an existing evolution code, upon which to base our efforts. In the Pitt null code, radial integrals were computed a single step at a time, using a variety of tools common to finite difference methods, such as predictor-corrector methods and manually regularized equations at the outer boundary.

SpEC uses spectral methods to increase accuracy and speed. Spectral methods compute derivatives and other elementary calculus operations by representing fields with a spanning set of basis functions, each of which has analytic derivatives. As such, accuracy is proportional not to the size of the stencil, but the collocation point density of the entire domain.

Spectral methods are not conducive to recycling the algorithmic methods employed by the Pitt null code. Instead, we began with the same equations and formalism and rebuilt the algorithm to exploit the advantages of the spectral method while avoiding its pitfalls. The principal advantage of spectral methods in this context is the ability to perform a highly accurate radial integral in a single step. The main pitfall is that the function to be integrated must be finite everywhere on the domain.

In the Bondi formulation, the hypersurface equations are not regular at \mathcal{I}^+ , diverging with terms in powers of r , the areal or Bondi radius. We solved this problem by expressing the integrand as a Laurent series and then regularizing the pole by

sequentially applying integration by parts. This method, which requires the calculation of derivatives up to 4th order, is inadvisable using finite differences. Spectral methods are accurate enough, however, that we find the correct answer with plenty of precision to spare.

One other major issue solved in Chapter 3 is that of the variable being present in nonlinear terms on the right hand side of one of the hypersurface equations. Pitt null code solved this problem using predictor-corrector methods, an inelegant approach when using spectral methods. We determined that the problem terms could be factorized with a Magnus expansion once the equations were expressed in matrix form, in a generalization of the integrating factor method. Fortunately, the terms in the Magnus expansion converge very quickly, and this method survived implementation with double precision floating point arithmetic.

With the analytic challenges of the hypersurface equations squared away, the spectral characteristic evolution algorithm was subjected to a battery of tests to ensure stability and the appropriate order of convergence with increased resolution. Finally, its results were compared with the Pitt null code running on the same inner boundary data. The results were consistent and convergent, until the somewhat temperamental Pitt null code gradually lost convergence while running on our test case. With better stability, robustness, accuracy, and about 200 times more speed, spectral characteristic evolution had arrived.

In September 2014, the nine month effort to establish stability and convergence of Spectral Characteristic Evolution was more or less complete, and I passed candidacy. The results of this work were published in *Classical and Quantum Gravity*. The paper describes the method using modern notation and four appendices. It also establishes consistency with the legacy Pitt null code, which is part of the Einstein toolkit, an open source library of General Relativity-related software.

Subsequent to publication, and somewhat to my surprise, the paper was recognized for its significance with a feature in CQG+. It was also featured in IOPSelect, an open access portal for selected CQG+ papers.

<http://arxiv.org/abs/1406.7029>

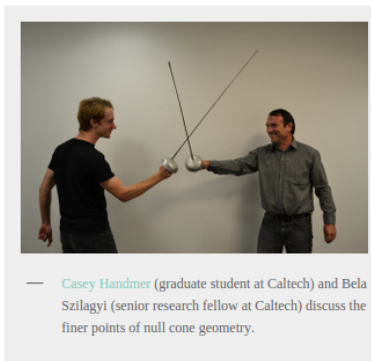
<http://iopscience.iop.org/0264-9381/32/2/025008/article>

<http://cggplus.com/2015/01/06/a-new-algorithm-for-gravitational-wave-propagation/>



Posted on January 6, 2015 by [publisherad](#)

A new algorithm for gravitational wave propagation



filtering.

Gravitational wave evolution – spectral style.

Colliding black holes create powerful ripples in spacetime. Of this we are certain. Directly detecting these ripples, or gravitational waves, is one of the hardest unsolved problems in physics. Inferring physical characteristics of black hole binaries and other gravitationally energetic events from their radiation requires accurate numerical simulation for matched

Figure 4: Screen cap from CQG+ website.

Spectral Characteristic Evolution: A New Algorithm for Gravitational Wave Propagation

Casey J. Handmer, Béla Szilágyi

Theoretical Astrophysics 350-17, California Institute of Technology, Pasadena,
California 91125, USA

E-mail: chandmer@caltech.edu

Abstract. We present a spectral algorithm for solving the full nonlinear vacuum Einstein field equations in the Bondi framework. Developed within the Spectral Einstein Code (SpEC), we demonstrate spectral characteristic evolution as a technical precursor to Cauchy Characteristic Extraction (CCE), a rigorous method for obtaining gauge-invariant gravitational waveforms from existing and future astrophysical simulations. We demonstrate the new algorithm’s stability, convergence, and agreement with existing evolution methods. We explain how an innovative spectral approach enables a two orders of magnitude improvement in computational efficiency.

1. What is Characteristic Evolution, and why?

As an international network of gravitational wave observatories come online, the race to the first direct detection of gravitational waves is expected to herald the beginning of gravitational wave astronomy. Detectors such as Advanced LIGO, VIRGO, GEO, and KAGRA aim for strain sensitivities approaching 10^{-24} [1, 2, 3, 4]. Nevertheless, signal candidates from compact binaries or supernovae will be on the

cusps of detectability, with very poor signal to noise ratios requiring matched filtering for detection[5]. Matched filtering requires a comprehensive template bank, the generation of which has been a primary goal of the field of numerical relativity. These templates cover a range of expected astronomical phenomena, and are generated by a variety of numerical codes, including the Spectral Einstein Code (SpEC)[6]. Filling out the template bank requires a balance of numerical relativity and analytic waveforms (post-Newtonian[7] and effective-one-body[8]), with waveform models often calibrated using numerical results[9, 10, 11].

One technical challenge facing the construction of a large template bank is extraction of gauge invariant waveforms from simulations. In general, large computationally intensive simulations are needed to describe the physics of events such as supernovae and compact object binary inspirals. While a waveform-like signal can readily be extracted from anywhere in the computational domain, waveforms are only rigorously defined at future null infinity. Finite radii waveform approximations are universally contaminated by coordinate system dynamics, or gauge effects, which are poorly understood and nearly impossible to remove or even quantify. Comparison with Cauchy Characteristic Extraction, or CCE, an alternative which applies Characteristic Evolution to enable waveform computation at future null infinity, suggests that extrapolation gauge errors could dominate the global error[12]. Characteristic Evolution has been previously implemented at up to 4th order radial accuracy[13], while complete extraction has been achieved with finite difference/volume methods up to 2nd order[14, 15].

Here we implement inner boundary extraction and evolution. This must be combined with an appropriate outer boundary algorithm to generate the gauge-invariant news at future null infinity. In a hypothetical complete system illustrated

in Figure 1(d), Cauchy Characteristic Matching (CCM) allows inflowing energy to cross the inner boundary (injection) and enter the Cauchy evolution, ameliorating issues with boundary reflections. Matching, however, faces many technical challenges beyond the scope of this paper, and has only been implemented in the linearized limit[16, 17].

Another method is extrapolation[12], which takes metric quantities at a series of increasing radii, then fits them to a function in $l = 1/r$. In this coordinate, $l = 0$ corresponds to infinitely far from the origin, where the extrapolated metric quantities are converted to waveforms. Because each sampling point is subject to an unknown degree of coordinate effect contamination, the extrapolated waveform is itself not gauge invariant.

While characteristic evolution is computationally and conceptually much more involved than extrapolation, it is able to provide gauge invariant waveforms unaffected by coordinate effects. These waveforms are unique modulo the supertranslations, a 4 parameter subgroup of the BMS group, corresponding to arbitrary inertial observer initial conditions at future null infinity[18, 19]. Removing gauge effects through characteristic evolution is essential for obtaining accurate and useful waveforms. Essentially, characteristic evolution takes metric data at a topologically spherical worldtube Γ enclosing the relativistic Cauchy evolution and evolves it, as well as initial data, outward to future null infinity, or \mathcal{I}^+ . At the outer boundary, the metric quantities can be read off and, in combination with an inertial conformal coordinate system, used to calculate the true waveform.

The calculation is performed in the Bondi system, in which radial coordinates are outgoing null rays: normal to the worldtube and to each time slice. The spherical coordinates and time-like foliation is adapted from the Cauchy evolution via the

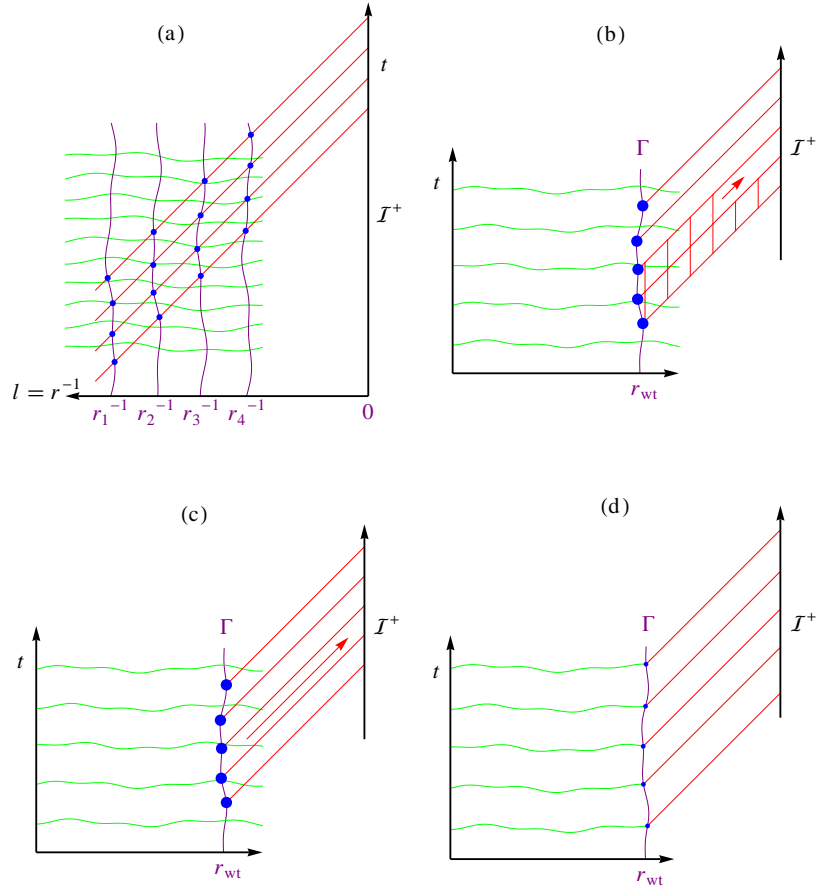


Figure 1. a) Extrapolation methodology. Time-interpolated points (blue) along four nested worldtubes (purple) are derived from metric data on each space-like foliation (green) and used to fit a polynomial in $l = r^{-1}$, which is extrapolated to \mathcal{I}^+ at $l = 0$. b) The finite difference-based characteristic evolution algorithm takes time-interpolated inner boundary conditions and solves each null foliation one null parallelogram at a time in a radial marching algorithm. c) Spectral extraction performs radial integration to \mathcal{I}^+ in a single step. d) A matching algorithm wherein characteristic and Cauchy evolutions share a time parameter and common domain boundary.

worldtube boundary data, illustrated in Figure 1(c).

While this simplifies aspects of the evolution, the domain is still infinite, and must be compactified. We use the compactification $r = R\rho/(1 - \rho)$, where r is the

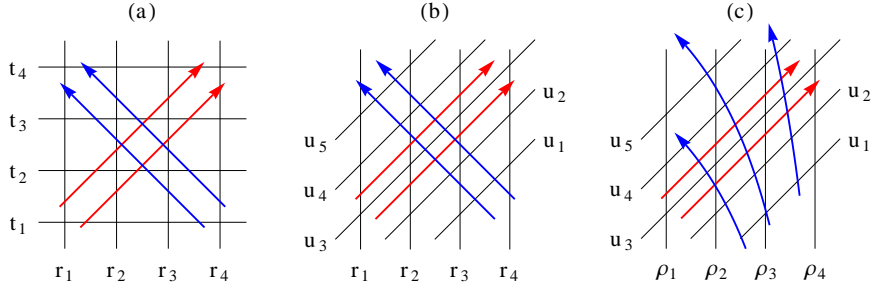


Figure 2. a) Ingoing (blue) and outgoing (red) characteristic worldlines on a radial (r) grid coordinate system. b) Retarded time ($u = r + t$) grid null coordinate parallels outgoing characteristics. c) Compactified null radial ($\rho = r/(R + r)$) grid coordinates bring \mathcal{S}^+ into a finite domain. Ingoing characteristics appear curved in this coordinate system.

Bondi radius, ρ is the compactified null radial coordinate and R the compactification parameter. Setting R to the Bondi radius of the worldtube $R = r_{\Gamma}$ confines $\rho \in [1/2, 1]$, as shown in Figure 2 (c). While the worldtube is defined by a constant coordinate radius sphere, the Bondi radius at this surface is a variable function of time and angles, giving rise to a wobbly, non-spherical shape in the Bondi coordinate system. This variable compactification parameter requires additional terms in the equations.

Fixing $\rho \in [1/2, 1]$ and having a variable compactification parameter is different to the approach used in earlier incarnations of CCE, which either interpolated the boundary's variable position or used a different compactification scheme[20, 12]. While the Pitt null code[14] assumed that a coordinate sphere of constant Cartesian radius formed the worldtube, we lift that constraint here. A fixed computational domain for Characteristic Evolution enables conceptually simple radial integration and dynamically variable extraction radii.

Figure 3 shows a series of diagrams illustrating the derivation of the

computational domain.

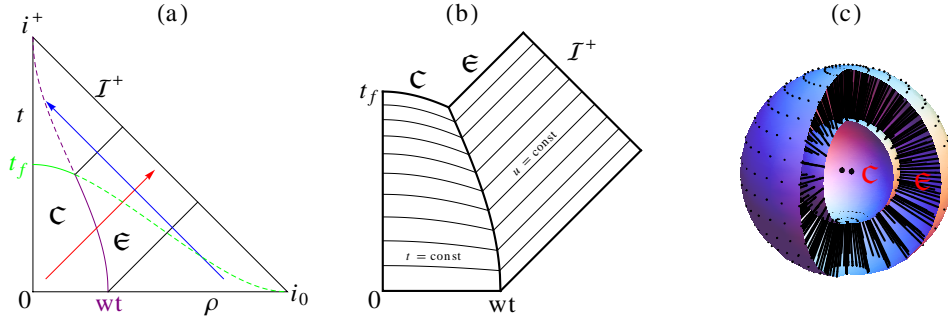


Figure 3. a) Compactified time coordinate yields Penrose-like diagram of global space, depicted here as Minkowski. Space-like foliated Cauchy evolution domain exists in world-sphere \mathfrak{C} , bounded by worldtube ‘wt’. Null foliated characteristic evolution domain in hollow world-sphere \mathfrak{E} extends worldtube to \mathcal{I}^+ . As before, blue and red arrows represent ingoing and outgoing characteristics respectively. t_f represents a space-like global final time of Cauchy evolution. Dashed lines extrapolate constant time and radius lines to i^+ and i_0 . b) A closer look at the two computational domains with space-like foliation in \mathfrak{C} and null foliations in \mathfrak{E} shown for clarity. The worldtube boundary between the two domains is the extraction surface, and doesn’t necessary reside on the outer boundary of the Cauchy evolution. c) A 3D rendering showing black radial compactified spokes with the equiangular gridpoint spacing used in our evolution.

2. Previous Work

An implementation of Characteristic Evolution was developed by the group of Winicour during the mid 1990s [20, 14, 16], and is now part of the publicly available Einstein tool kit (PITNullCode)[21]. In its original form it uses finite differences, achieving 2^{nd} order accuracy. The code has been updated and adapted many times

since, and in its current form takes $\mathcal{O}(\text{days})$ to produce a waveform at an accuracy that matches that of the Cauchy evolution for $\mathcal{O}(1000M)$ SpEC runs. Five years ago an $\mathcal{O}(1000M)$ run was sufficiently challenging that there was no CCE bottleneck. Today, with hundreds of runs exceeding dozens of orbits and a few exceeding $10^5 M$, a faster algorithm is needed. The goal is to have the SpEC characteristic code run alongside the Cauchy evolution at an insignificant additional cost.

This algorithm would build on the formalism of the Pitt null code, but exploit SpEC capabilities to use spectral methods and a much coarser grid to achieve equivalent accuracy. The finite difference algorithm marches outwards one null parallelogram at a time, shown in Figure 1 (b). A spectral algorithm would rapidly calculate high-accuracy radial data in a single step of numerical integration, as shown in Figure 1 (c).

The difficulty of a spectral approach lies in consistently treating divergences. As written, the hypersurface evolution equations' source terms are linear or greater order in r and diverge at infinity. In a finite domain, large but finite terms on either side would numerically cancel, leaving a valid result with no further complications. The Pitt null code uses an asymptotic form to solve the final step to \mathcal{I}^+ . To include a point at infinity within a single domain spectral scheme, however, this divergence has to be understood and pre-emptively cancelled. Here, we present a novel approach to regularizing the full nonlinear system, enabling a fully spectral treatment.

3. A New Algorithm

3.1. General Information

The Bondi metric can be expressed as

$$\begin{aligned}
 ds^2 = & - \left(e^{2\beta}(rW + 1) - r^2 h_{AB} U^A U^B \right) du^2 \\
 & - 2e^{2\beta} dudr - 2r^2 h_{AB} U^B dudy^A + r^2 h_{AB} dy^A dy^B .
 \end{aligned} \tag{3.1}$$

y^A are angular coordinates, where the uppercase Latin indices A, B , and so on range from 2 to 3. The quantities $W, h_{AB}, U^A, Q_A, \beta$ parametrise the metric, representing respectively the mass aspect, the conformal 2-metric, the shift and its radial derivative, and the lapse. Where non-scalar, they are related to complex spin-weighted quantities by contracting them with the appropriate dyad. The dyad q^A is a complex field on the unit sphere satisfying $q^A q_A = 0$, $q^A \bar{q}_A = 2$, $q^A = q^{AB} q_B$, with $q^{AB} q_{BC} = \delta_C^A$ and $q_{AB} = (q_A \bar{q}_B + \bar{q}_A q_B)/2$, the unit sphere metric. Under this convention, the spin-weighted functions $U = U^A q_A$ and $Q = Q_A q^A$, while $J = h_{AB} q^A q^B/2$ uniquely determines the spherical conformal 2-metric component of the general 4-metric[20]. We chose a dyad consistent with our formulation of the eth operator \eth [22], given by $q^A = (-1, -i/\sin\theta)$. This is regular everywhere except the poles, which we can avoid through careful choice of grid points. It is worth noting that any choice of angular coordinates are possible. Other conventions use multiple patches to avoid singularities at the poles, in which the phase dislocation due to spin-weight when moving from patch to patch is explicit.

The key to the Bondi formulation is that all the spin-weighted metric quantities have a heirarchical structure, enabling their natural ordering as a nested series of self-referential equations on the outgoing null hypersurface. This form first appeared in Winicour[23, 16, 20]. In a relatively simple form they are

$$\beta_{,r} = N_\beta , \quad (3.2)$$

$$(r^2 Q)_{,r} = -r^2(\bar{\delta}J + \delta K)_{,r} + 2r^4\delta(r^{-2}\beta)_{,r} + N_Q , \quad (3.3)$$

$$U_{,r} = r^{-2}e^{2\beta}Q + N_U , \quad (3.4)$$

$$(r^2 W)_{,r} = \frac{1}{2}e^{2\beta}\mathcal{R} - 1 - e^\beta\delta\bar{\delta}e^\beta + \frac{1}{4}r^{-2}(r^4(\bar{\delta}\bar{U} + \delta U))_{,r} + N_W , \quad (3.5)$$

where the scalar curvature

$$\mathcal{R} = 2K - \delta\bar{\delta}K + \frac{1}{2}(\bar{\delta}^2 J + \delta^2 \bar{J}) + \frac{1}{4K}(\bar{\delta}\bar{J}\delta J - \bar{\delta}J\delta\bar{J}) , \quad (3.6)$$

and the time derivative term

$$2(rJ)_{,ur} = ((1 + rW)(rJ)_{,r})_{,r} - r^{-1}(r^2\delta U)_{,r} + 2r^{-1}e^\beta\delta^2 e^\beta - (rW)_{,r}J + N_J , \quad (3.7)$$

where

$$1 = K^2 - J\bar{J}. \quad (3.8)$$

The nonlinear terms $N_\beta, N_Q, N_U, N_W, N_J$ are given in Appendix D‡. The radial compactification is given by $r = R\rho/(1 - \rho)$, where the compactification parameter $R(u, \theta, \phi)$ is the (not necessarily constant) Bondi areal radius of the worldtube.

On each hypersurface in the spacetime foliation, each equation is solved in turn. Given J , β is solved, then U , Q , and W in turn, enabling the computation of $J_{,u}$. $J_{,u}$ permits a step forward in time and J is thus defined on the next hypersurface.

Spherical derivatives are implemented using the eth operator $\bar{\delta}$ on spin-weighted spherical harmonics. $\bar{\delta}$ is given by the contraction of the dyad with the derivative operator[22].

‡ Note that W is defined according to the convention in [16], which differs from [20] by a factor of r^2 .

In spherical coordinates, this can be written

$$\bar{\delta}\eta = -(\sin^s \theta) \left(\frac{\partial}{\partial \theta} + \frac{i}{\sin \theta} \frac{\partial}{\partial \phi} \right) (\sin^{-s} \theta \eta), \quad (3.9)$$

$$\bar{\delta}\eta = -(\sin^{-s} \theta) \left(\frac{\partial}{\partial \theta} - \frac{i}{\sin \theta} \frac{\partial}{\partial \phi} \right) (\sin^s \theta \eta). \quad (3.10)$$

$\bar{\delta}$ and $\bar{\delta}$ increment and decrement respectively the spin-weight s of the quantity they act upon. Details are given in Appendix C.

In the Pitt null code approach to CCE, a finite difference-based algorithm is used to solve the hypersurface equations, radially marching from the inner boundary outward, one point at a time. In our algorithm, we use spectral methods to calculate the radial indefinite integral on all collocation points along a spherical radial spoke in a single calculation. A spectral approach is faster and more accurate, but requires the finessing of a few technical difficulties.

The most obvious of these appears in the hypersurface equations for W and Q . To calculate a numerical integral, it is necessary to express the integrand as a bounded function on all radial collocation points, including those at \mathcal{S}^+ . Given that Q is regular and $\mathcal{O}(1)$ at \mathcal{S}^+ , r^2Q is clearly divergent. The integral of the right hand side is similarly divergent for the outermost collocation point, where $r \rightarrow \infty$ or $\rho \rightarrow 1$. Here, we solve this problem by expressing the right hand side as a Laurent series around the pole at $\rho = 1$ and then repeatedly integrating by parts. Mathematically, if the equation is written

$$(r^2Q)_{,\rho} = A + \frac{B}{1-\rho} + \frac{C}{(1-\rho)^2} + \frac{D}{(1-\rho)^3}, \quad (3.11)$$

then, as shown in Appendix A,

$$\begin{aligned}
Q = & Q_0 + \frac{D}{2\rho^2 R^2} - (-C + D'/2) \frac{1-\rho}{\rho^2 R^2} - (B - C' + D''/2) \frac{(1-\rho)^2 \log(1-\rho)}{\rho^2 R^2} \\
& - (B' - C'' + D'''/2) \frac{(\rho + (1-\rho)\log(1-\rho))(1-\rho)^2}{\rho^2 R^2} \\
& + \frac{(1-\rho)^2}{\rho^2 R^2} \int A + (B'' - C''' + D''''/2)(\rho + (1-\rho)\log(1-\rho)) , \tag{3.12}
\end{aligned}$$

where $D' = \frac{\partial D}{\partial \rho}$ and so on. In this context, the \int operator refers to a radial numerical integral where the integration constant is fixed such that the inner boundary value (at the worldtube) vanishes. Note that all terms within the integral are bounded within the domain $\rho \in [1/2, 1]$, including at \mathcal{S}^+ . On the outer boundary, terms in $\log(1-\rho)$ must cancel out to preserve C^∞ differentiability.

A second, less obvious, issue is that the right hand side of the $J_{,u\rho}$ hypersurface equation has nonlinear terms with the desired quantity $J_{,u}$ in them (as seen in the equation for P_1 , Eqn A6, Bishop *et al.* [16]). In order to perform the radial integral and solve for $J_{,u}$ in a single step, these nonlinear terms have to be somehow removed. One approach is to factorise using an integrating factor and, conceptually, that is what is done. We shall illustrate this first with a simple example.

Given

$$J_{,u\rho} + A J_{,u} = B , \text{ then} \tag{3.13}$$

$$\left(e^{\int A} J_{,u} \right)_{,\rho} = e^{\int A} B , \text{ and} \tag{3.14}$$

$$J_{,u} = e^{-\int A} \int e^{\int A} B . \tag{3.15}$$

The actual equations are, however, more difficult as the variable is complex, and the nonlinear term also includes the complex conjugate $\bar{J}_{,u}$ term, which makes a simple factorization impossible. Writing $J_{,u} = \Phi$, the actual equation can be written

$$(r\Phi)_{,\rho} - (rJ)(\Phi\bar{\Gamma} + \bar{\Phi}\Gamma) = A + \frac{B}{1-\rho} + \frac{C}{(1-\rho)^2} , \text{ where} \tag{3.16}$$

$$\Gamma = \left(J_{,\rho} - J \frac{K_{,\rho}}{K} \right). \quad (3.17)$$

The right hand side is a Laurent expansion analogous to the equations for Q and W. The part $(\Phi\bar{\Gamma} + \bar{\Phi}\Gamma)$ is a quantity plus its conjugate and is thus wholly real. This leads to the insight that a real-imaginary split of the equation is productive. Writing $J = J_{\mathcal{R}} + iJ_{\mathcal{I}}$, we can exploit the isomorphism between complex numbers and non-singular 2×2 matrices by writing

$$\begin{pmatrix} r\Phi_{\mathcal{R}} \\ r\Phi_{\mathcal{I}} \end{pmatrix}, \rho - \begin{pmatrix} J_{\mathcal{R}}\Gamma_{\mathcal{R}} & J_{\mathcal{R}}\Gamma_{\mathcal{I}} \\ J_{\mathcal{I}}\Gamma_{\mathcal{R}} & J_{\mathcal{I}}\Gamma_{\mathcal{I}} \end{pmatrix} \begin{pmatrix} r\Phi_{\mathcal{R}} \\ r\Phi_{\mathcal{I}} \end{pmatrix} = \begin{pmatrix} RHS_{\mathcal{R}} \\ RHS_{\mathcal{I}} \end{pmatrix}. \quad (3.18)$$

We have restored the integrating factor form of the equation, only now in matrix form. The use of non-constant matrices for an integrating factor requires the calculation of commutators, which in all but the trivial case are non-zero. The required formalism is the Magnus expansion[24, 25], in which the usual integrating factor is supplemented by integrals of progressively higher order commutators.

Let

$$F = \begin{pmatrix} J_{\mathcal{R}}\Gamma_{\mathcal{R}} & J_{\mathcal{R}}\Gamma_{\mathcal{I}} \\ J_{\mathcal{I}}\Gamma_{\mathcal{R}} & J_{\mathcal{I}}\Gamma_{\mathcal{I}} \end{pmatrix}, \quad (3.19)$$

and

$$\Phi = \begin{pmatrix} \Phi_{\mathcal{R}} \\ \Phi_{\mathcal{I}} \end{pmatrix}. \quad (3.20)$$

Then

$$(r\Phi)_{,\rho} - F.(r\Phi) = \exp(\Omega(\rho)). \left(\exp(-\Omega(\rho)).(r\Phi) \right)_{,\rho}, \quad (3.21)$$

where

$$\Omega(\rho) = \sum_{k=1}^{\infty} \Omega_k(\rho). \quad (3.22)$$

Write $F(\rho_1) = F_1$. Then Ω_k forms a series called the Magnus expansion.

$$\Omega_1(\rho) = \int_{\rho_0}^{\rho} d\rho_1 F_1 , \quad (3.23)$$

$$\Omega_2(\rho) = \frac{1}{2} \int_{\rho_0}^{\rho} d\rho_1 \int_{\rho_0}^{\rho} d\rho_2 [F_1, F_2] , \quad (3.24)$$

$$\Omega_3(\rho) = \frac{1}{6} \int_{\rho_0}^{\rho} d\rho_1 \int_{\rho_0}^{\rho} d\rho_2 \int_{\rho_0}^{\rho} d\rho_3 [F_1, [F_2, F_3]] + [F_3 [F_2, F_1]] , \quad (3.25)$$

and so on.

In practise, this series must be truncated. Fortunately, $|F| \approx 10^{-3} \ll 1$ in practical cases, so the series converges rapidly, necessitating calculation of only the first three terms. Although a formalism exists[19] to deal with the non-linear terms without resorting to the Magnus expansion, it requires transformation in terms of dyads, whose issues around the poles we have been careful to avoid.

With the Magnus expansion, the troublesome nonlinear terms are readily dealt with and the equation can be expressed in the form

$$(r\Phi)_{,\rho} = \tilde{A} + \frac{\tilde{B}}{1-\rho} + \frac{\tilde{C}}{(1-\rho)^2} . \quad (3.26)$$

This is solved analogously to the radial hypersurface equations for W and Q .

3.2. Details specific to our implementation

In our implementation, we used a spherical coordinate system. The Chebyshev pseudospectral method was used for the (1D interval) radial basis function. Spherpac (for real tensor quantities) and Spinsfast (for complex spin-weighted quantities) were used for the 2D spherical basis function[26, 27, 28].

Calculus operations such as integration, differentiation, and computation of δ were performed in each basis function according to standard methods. Time stepping was performed with an adaptive Dormand Prince 5th order routine, or Runge-Kutta

4 with constant time steps. Spectral filtering of spatial quantities ensured that all system modes remained within the time integrators' domains of stability. Specifically, the i^{th} radial coefficient was filtered by a factor $\exp(-108(i/(N_\rho - 1))^{24})$, where i varies between 0 and $N_\rho - 1$. Angular coefficients were set to zero for $l = L_{\text{max}}$ and $l = L_{\text{max}} - 1$. Filtering was applied at the end of each time step and to the hypersurface quantities Q , W , and H after their computation.

4. Stability and Convergence

The spectral characteristic evolution algorithm is analytically derived, but how does it actually perform? We tested the stability and convergence of the code under a variety of circumstances designed to far exceed the demands of any actual CCE run[12].

For a stability test, we ran the algorithm with a variety of settings for a million steps with white noise initial and boundary conditions of magnitude 10^{-6} . The linear setting truncates all nonlinear terms, and represents a baseline condition. The nonlinear setting restores all nonlinear terms in the equations. The most general setting includes a variable inner boundary position, encoded in the magnitude of the compactification parameter R . Each of these three conditions was run, and in all three cases, the norm of J was stable. In particular, all three runs do not grow exponentially, as seen in Figure 4.

The purpose of a spectral algorithm is to obtain faster convergence, particularly with respect to radial integration. We ran a series of tests while varying N_ρ between 6 and 46. The test was run on the generic run discussed in Section 6 between $t = 1000M$ and $t = 1100M$, and the results averaged between $t = 1050M$ and $t = 1100M$ to remove any transient contamination. While our algorithm can use any one-dimensional spectral representation for the radial direction, these tests were

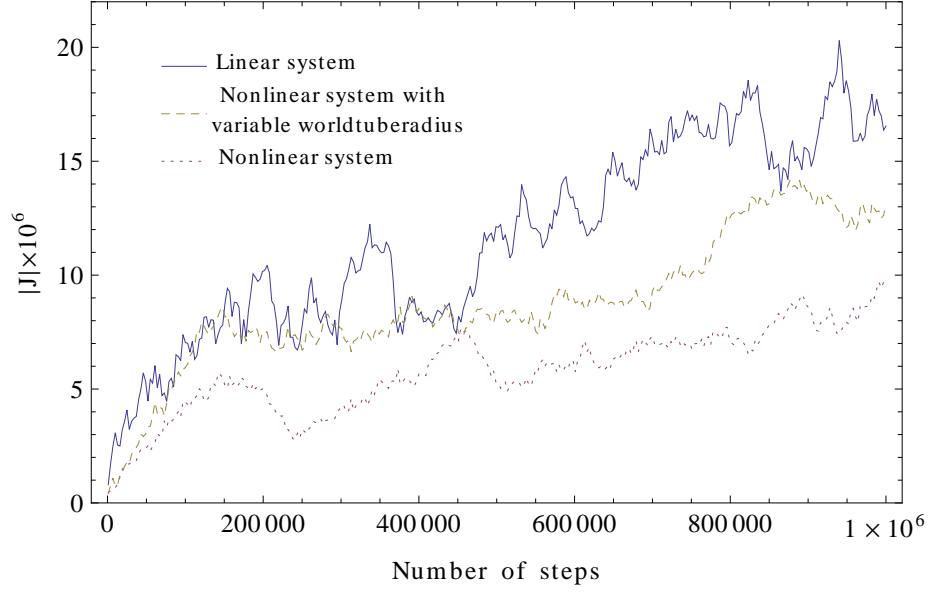


Figure 4. Graph of $|J|$ over a million time steps with a white noise boundary condition. The three lines represent a linear baseline, a nonlinear run, and the full nonlinear system including boundary position variation. All three runs display sub-exponential growth, indicating stability. For the linear test, a minimal resolution of $N_\rho = 4$, $L = 8$ was used. For the nonlinear tests, a minimal resolution of $N_\rho = 8$, $L = 12$ was used. All tests used an adaptive RK3 time stepper.

conducted using Gauss Chebyshev Lobatto polynomial basis functions, as discussed in the previous section. Figure 5 shows that local relative error in J converges exponentially as the number of radial points increases up to around 24, at which point convergence becomes sub-exponential due to roundoff error introduced in the integration algorithm.

Convergence with angular resolution was calculated identically to that for Figure 5, and shows rapid exponential convergence, as seen in Figure 6. Our implementation uses the Spinsfast package[28] for spin-weighted spherical harmonic computation in a manner analogous to Spherepack.

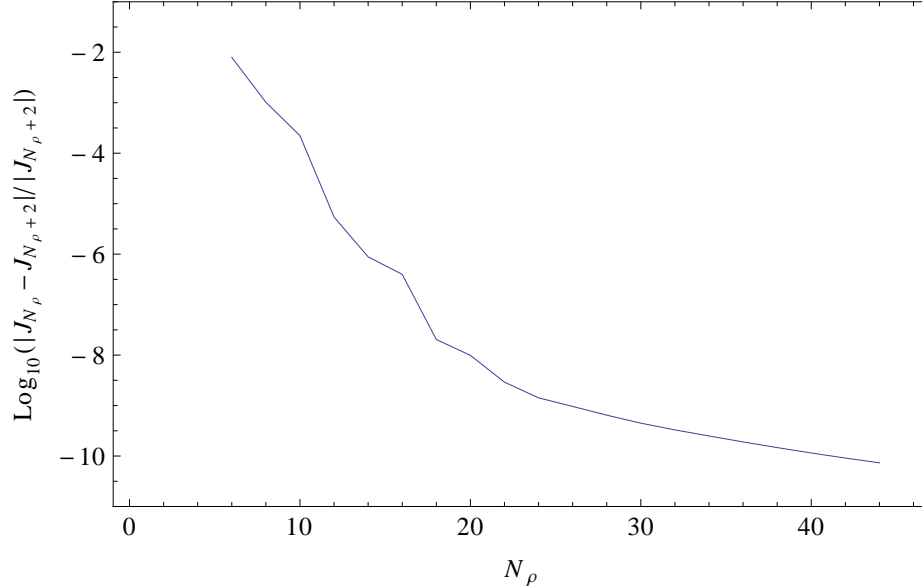


Figure 5. Log(relative error) shows a linear relationship with number of radial points N_ρ , indicating spectral convergence. At $N_\rho \approx 24$, convergence turns sub-exponential. Error is calculated according to $\text{Mean}_{1050M < t < 1100M} \left(\log_{10} \frac{|J_{N_\rho} - J_{N_\rho+2}|_\infty}{|J_{N_\rho+2}|_\infty} \right)$ for the generic precessing run. For these runs, $L = 16$, $\Delta t = 0.4M$, RK4 is used, and N_ρ varies from 6 to 46.

Finally, timestep convergence was analysed. For the purposes of this test, the minimum grid spacing to timestep was held constant, while the timestep was varied over more than an order of magnitude. The code displays 4th order time convergence, consistent with the chosen integrator RK4, as shown in Figure 7.

5. Comparison With Finite Differences Evolution

For longer run comparisons we used the generic precessing Binary Black Hole simulation detailed in Table 1 (case 4) of Taylor *et al.*[12]. Its parameters are mass ratio $q = 3$, black hole spin $\chi_1 = (0.7, 0, 0.7)/\sqrt{2}$ and $\chi_2 = (-0.3, 0, 0.3)/\sqrt{2}$, number of orbits 26, total time $T = 7509M$, initial eccentricity 10^{-3} , initial frequency $\omega_{ini} = 0.032/M$, and extraction (coordinate) radius $R = 100M$. We performed 3 runs

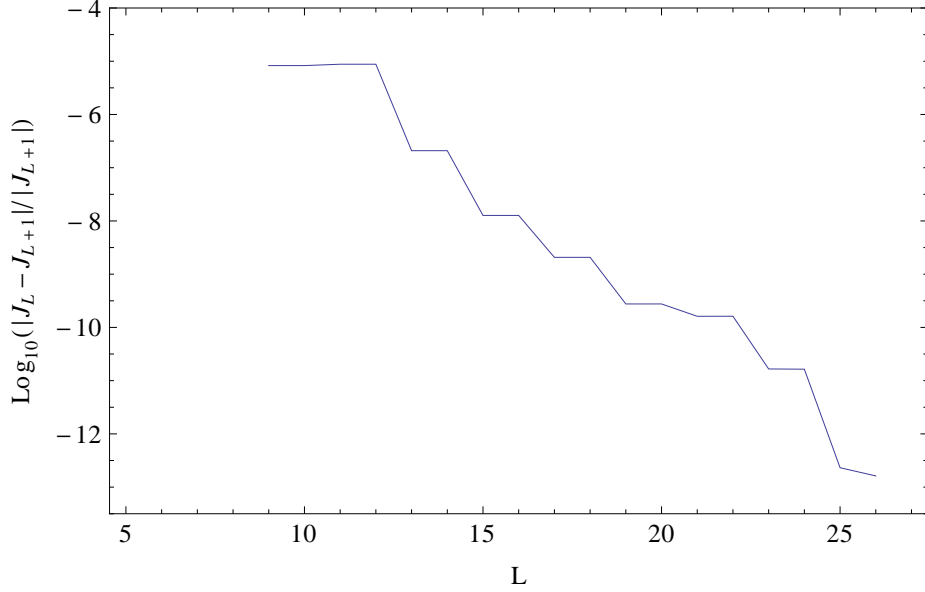


Figure 6. Log(relative error) vs spherical resolution shows rapid spectral convergence. Error is calculated analogously to Figure 5. For these runs, $N_\rho = 24$, $\Delta t = 0.4M$, RK4 is used, and L varies from 8 to 27.

using the PITT null code for baseline comparisons with 3 runs using the new spectral Characteristic Evolution code, using parameters shown in Table 1. The spectral code converges rapidly to within the error implied by the PITT null code, as shown in Figure 8. Parameters for the **SpEC** runs were specifically chosen for comparable levels of error with the Pitt null code. Note that despite **SpEC** code spatial resolution parameters being chosen for consistent minimum grid spacing to time step ratio, rather than equal numbers of points, the global error comparison is not adversely affected. Both codes were run on the same cluster with dense output.

Note also that the resolution of the **SpEC** runs is an order of magnitude lower, the time steps an order of magnitude longer, and the run time more than two orders of magnitude faster for equivalent or superior accuracy. In this case, accuracy is ultimately limited by the order of the time stepper (RK4) and the order of the time interpolation on the inner boundary (also 4th order).

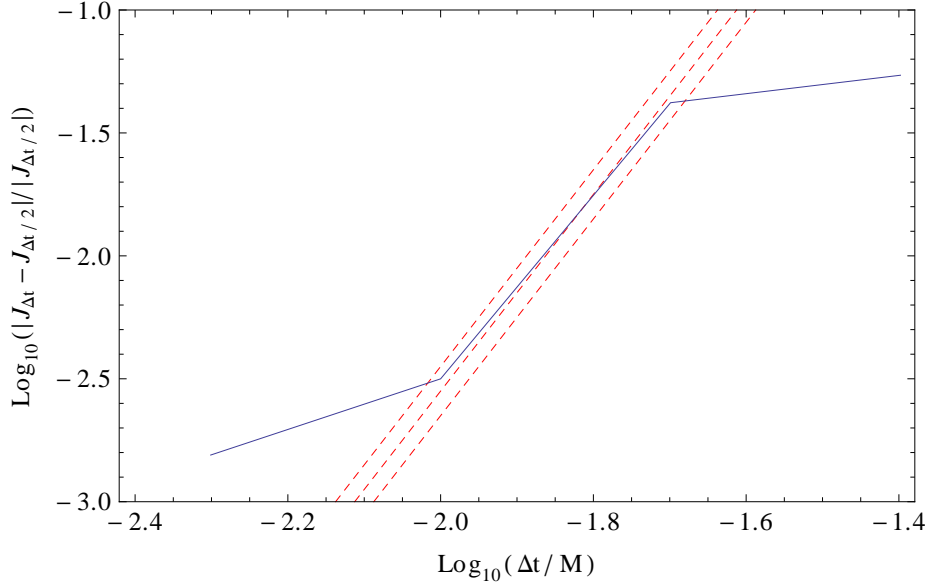


Figure 7. Log plot of relative error vs time step shows 4th order convergence, demarcated by parallel dashed red lines. Error is calculated analogously to Figure 5. For this test the minimum grid spacing is adjusted with time step to maintain a constant ratio. For time steps of $(0.04M, 0.02M, 0.01M, 0.005M, 0.0025M)$, the number of radial points was $(6, 8, 11, 15, 21)$ respectively. Angular resolution was held constant with $L = 9$.

| Run | Pitt 1 | Pitt 2 | Pitt 3 | SpEC 1 | SpEC 2 | SpEC 3 |
|---------------------|--------|-----------|--------|--------|----------|--------|
| N_r | 100 | 150 | 200 | 10 | 12 | 14 |
| N_{stereo} or L | 40 | 60 | 80 | 12 | 14 | 17 |
| $\Delta t/M$ | 0.1 | 0.0666... | 0.05 | 1.0 | 0.666... | 0.5 |
| T (CPU hours) | 2688 | 5760 | 6912 | 12 | 31 | 52 |

Table 1. Parameters used for code comparisons. The Pitt null code uses two stereographic patches of size N_{stereo}^2 . For both codes, the total number of angular points is given by $2N_{stereo}^2$ and $2L^2$ respectively.

Global accuracy and convergence was assessed by graphing the relative complex difference between runs of adjacent accuracy. The errors are computed according to

$$\begin{aligned}
 E_{Pitt\ low\ res} &= \frac{|j_{22Pitt\ 1} - j_{22Pitt\ 2}|}{|j_{22Pitt\ 2}|}, \\
 E_{Pitt\ high\ res} &= \frac{|j_{22Pitt\ 2} - j_{22Pitt\ 3}|}{|j_{22Pitt\ 3}|}, \\
 E_{SpEC\ low\ res} &= \frac{|j_{22SpEC\ 1} - j_{22SpEC\ 2}|}{|j_{22SpEC\ 2}|}, \\
 E_{SpEC\ high\ res} &= \frac{|j_{22SpEC\ 2} - j_{22SpEC\ 3}|}{|j_{22SpEC\ 3}|}, \\
 E_{Pitt\ vs\ SpEC} &= \frac{|j_{22SpEC\ 3} - j_{22Pitt\ 3}|}{|j_{22SpEC\ 3}|},
 \end{aligned}$$

where j_{22} is the $_{22}$ spherical harmonic coefficient of J .

Figure 8 shows strong and consistent convergence of the SpEC runs over the full $7509M$, as well as consistent agreement between the SpEC and Pitt runs. Figure 9 shows convergence during the junk radiation part of the run, where partial loss of agreement between the Pitt and SpEC runs is caused by their respective differences in unphysical junk radiation resolution. The error nevertheless remains well bounded for the entire run.

6. Conclusion

A new algorithm for spectral Characteristic Evolution has been developed, implemented, and demonstrated within the SpEC framework. It exploits analytic regularization of the vacuum hypersurface equations and the accuracy and speed of spectral methods. Stability, self-convergence, and convergent agreement with the existing finite difference Characteristic Evolution code are demonstrated. This algorithm will form the basis for a complete extraction and matching methodology that will enable gauge invariant waveforms and junk radiation-free initial conditions to be computed on the fly.

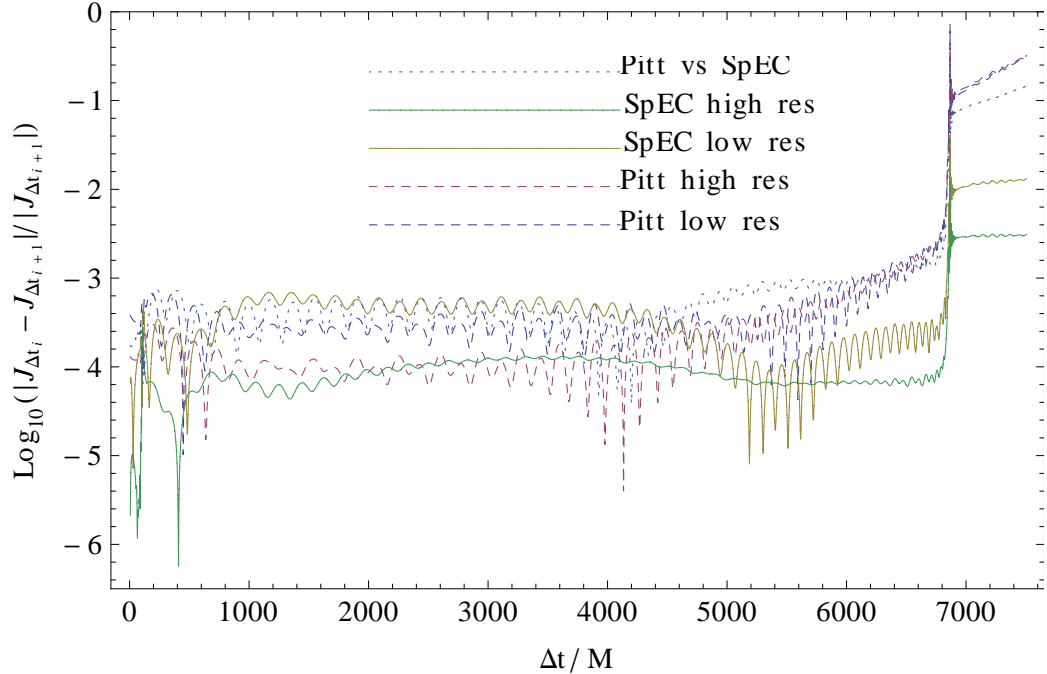


Figure 8. Comparison of convergence of Pitt and SpEC evolution codes. The Pitt runs (dashed) show 2^{nd} order convergence until around $5000M$, when convergence is gradually lost. The SpEC runs (solid), with parameters chosen for comparable levels of error, display higher order time convergence throughout the entire run. The dotted line shows the level of agreement between the highest resolution runs of each code, consistent with their respective resolution of junk radiation. Peak amplitude $J_{,uu}$ occurs at $t = 6832M$, at which point error in relative amplitude and phase is $10^{-2.367}$ and 0.002 respectively. These values represent expected error for a strain calculation.

Acknowledgments

We thank Jeffrey Winicour for his invaluable insight and encyclopædic knowledge of all things Extraction. We thank Nicholas Taylor for his generic spin BBH run we used to test and baseline code performance. We thank Mark Scheel, Yanbei Chen, and Christian Reisswig for their advice, support, and technical

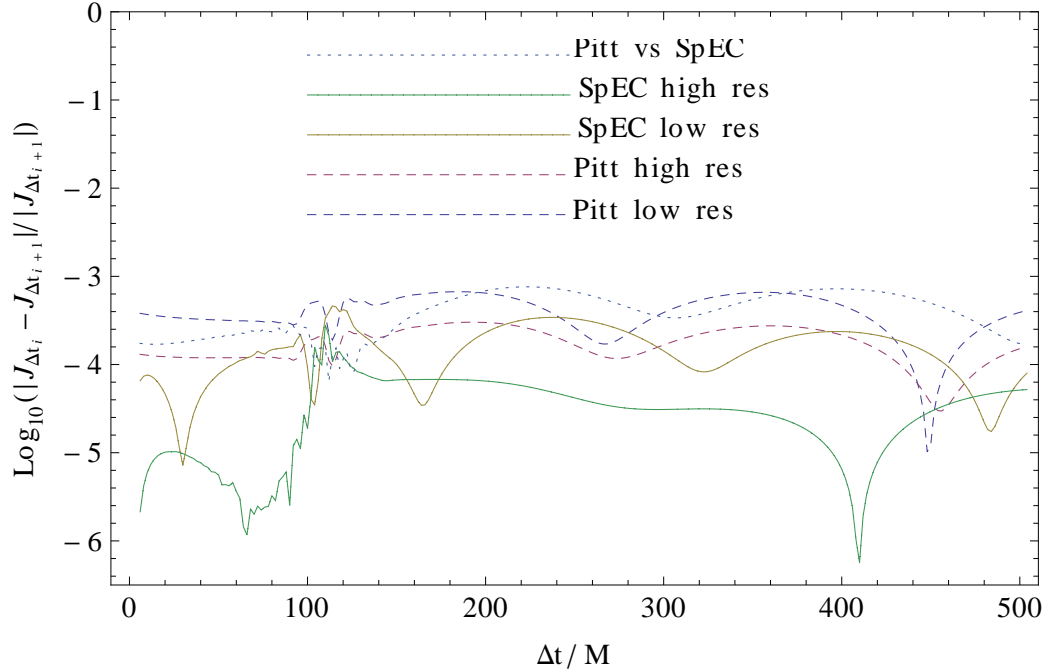


Figure 9. First $500M$ of Figure 8 shows very high initial agreement of codes until evolution of junk radiation. Nevertheless, agreement remains consistently high.

expertise. This research used the Spectral Einstein Code (SpEC)[6]. The Caltech cluster `zwicki.cacr.caltech.edu` is an essential resource for SpEC related research, supported by the Sherman Fairchild Foundation and by NSF award PHY-0960291. This research also used the Extreme Science and Engineering Discovery Environment (XSEDE) under grant TG-PHY990002. The UCSD cluster `ccom-boom.ucsd.edu` was used during code development. This project was supported by the Sherman Fairchild Foundation, and by NSF Grants PHY-1068881, AST-1333520, and CAREER Grant PHY-0956189.

References

- [1] S. J. Waldman, “The advanced ligo gravitational wave detector,” Tech. Rep. LIGO-P0900115-v2, LIGO Project, 2011.

- [2] T. Accadia, F. Acernese, F. Antonucci, P. Astone, G. Ballardin, *et al.*, “Plans for the upgrade of the gravitational wave detector VIRGO: Advanced VIRGO,” in Proceedings of the Twelfth Marcel Grossmann Meeting on General Relativity, T. Damour, R. T. Jantzen, and R. Ruffini, eds., pp. 1738–1742. 2009.
- [3] **LIGO Scientific Collaboration** Collaboration, H. Grote, “The GEO 600 status,” Class. Quantum Grav. **27** (2010) 084003.
- [4] K. Somiya and the KAGRA Collaboration, “Detector configuration of KAGRA—the japanese cryogenic gravitational-wave detector,” Class. Quantum Grav. **29** no. 12, (2012) 124007.
- [5] B. Allen, W. G. Anderson, P. R. Brady, D. A. Brown, and J. D. Creighton, “FINDCHIRP: An Algorithm for detection of gravitational waves from inspiraling compact binaries,” Phys. Rev. D **85** (2012) 122006, [arXiv:gr-qc/0509116](#) [gr-qc].
- [6] A. H. Mroue, M. A. Scheel, B. Szilagy, H. P. Pfeiffer, M. Boyle, D. A. Hemberger, L. E. Kidder, G. Lovelace, S. Ossokine, N. W. Taylor, A. Zenginoglu, L. T. Buchman, T. Chu, E. Foley, M. Giesler, R. Owen, and S. A. Teukolsky, “A catalog of 174 binary black hole simulations for gravitational wave astronomy,” Phys. Rev. Lett. **111** (2013) 241104, [arXiv:1304.6077](#) [gr-qc].
- [7] A. Taracchini, Y. Pan, A. Buonanno, E. Barausse, M. Boyle, T. Chu, G. Lovelace, H. P. Pfeiffer, and M. A. Scheel, “Prototype effective-one-body model for nonprecessing spinning inspiral-merger-ringdown waveforms,” Phys. Rev. D **86** no. 2, (July, 2012) 024011, [arXiv:1202.0790](#) [gr-qc].
- [8] Y. Pan, A. Buonanno, A. Taracchini, L. E. Kidder, A. H. Mroue, *et al.*, “Inspiral-merger-ringdown waveforms of spinning, precessing black-hole binaries in the effective-one-body formalism,” Phys. Rev. D **89** (2013) 084006, [arXiv:1307.6232](#) [gr-qc].
- [9] S. Bernuzzi, M. Thierfelder, and B. Bruegmann, “Accuracy of numerical relativity waveforms from binary neutron star mergers and their comparison with post-Newtonian waveforms,” Phys. Rev. D **85** (2012) 104030, [arXiv:1109.3611](#) [gr-qc].
- [10] T. Hinderer, A. Buonanno, A. H. Mroué, D. A. Hemberger, G. Lovelace, H. P. Pfeiffer, L. E. Kidder, M. A. Scheel, B. Szilagy, N. W. Taylor, and S. A. Teukolsky, “Periastron Advance in Spinning Black Hole Binaries: Comparing Effective-One-Body and Numerical Relativity,” Phys. Rev. D **88** no. 8, (Oct., 2013) 084005, [arXiv:1309.0544](#) [gr-qc].
- [11] **The NRAR Collaboration** Collaboration, I. Hinder *et al.*, “Error-analysis and comparison

- to analytical models of numerical waveforms produced by the NRAR Collaboration,” Classical and Quantum Gravity **31** no. 2, (2014) 025012, [arXiv:1307.5307 \[gr-qc\]](#).
- [12] N. W. Taylor, M. Boyle, C. Reisswig, M. A. Scheel, T. Chu, L. E. Kidder, and B. Szilágyi, “Comparing gravitational waveform extrapolation to Cauchy-characteristic extraction in binary black hole simulations,” Phys. Rev. D **88** (Dec, 2013) 124010, [arXiv:1309.3605 \[gr-qc\]](#). <http://link.aps.org/doi/10.1103/PhysRevD.88.124010>.
- [13] C. Reisswig, N. T. Bishop, and D. Pollney, “General relativistic null-cone evolutions with a high-order scheme,” Gen. Rel. Grav. **45** (5) (2013) 1069–1094, [arXiv:1208.3891 \[gr-qc\]](#).
- [14] M. C. Babiuc, B. Szilágyi, J. Winicour, and Y. Zlochower, “A characteristic extraction tool for gravitational waveforms,” Phys. Rev. D **84** (Aug, 2011) 044057, [arXiv:1011.4223 \[gr-qc\]](#). <http://link.aps.org/doi/10.1103/PhysRevD.84.044057>.
- [15] Oliveira, H. P. and Rodrigues, E. L., “Numerical evolution of axisymmetric vacuum spacetimes: a code based on the galerkin method,” Class. Quantum Grav. **28** (2011) 235011, [arXiv:0809.2837 \[gr-qc\]](#).
- [16] Bishop, Nigel T., Isaacson, R., Gomez, R., Lehner, L., Szilagy, B., and Winicour, J., “Cauchy-characteristic matching,” [arXiv:gr-qc/9801070](#).
- [17] B. Szilagy, B. G. Schmidt, and J. Winicour, “Boundary conditions in linearized harmonic gravity,” Phys.Rev. **D65** (2002) 064015, [arXiv:gr-qc/0106026 \[gr-qc\]](#).
- [18] R. K. Sachs, “Gravitational waves in general relativity. VIII. waves in asymptotically flat space-time,” Proc. R. Soc. Lond. A **270** no. 1340, (October, 1962) 103–126. <http://www.jstor.org/stable/2416200>.
- [19] L. A. Tamburino and J. H. Winicour, “Gravitational fields in finite and conformal Bondi frames,” Phys. Rev. **150** (1966) 1039–1053. <http://link.aps.org/doi/10.1103/PhysRev.150.1039>.
- [20] N. T. Bishop, R. Gomez, L. Lehner, M. Maharaj, and J. Winicour, “High-powered gravitational news,” Phys. Rev. **D56** (1997) 6298–6309, [arXiv:qr-qc/9708065](#).
- [21] F. Löffler, J. Faber, E. Bentivegna, T. Bode, P. Diener, et al., “The Einstein Toolkit: A Community Computational Infrastructure for Relativistic Astrophysics,” Class. Quant. Grav. **29** (2012) 115001, [arXiv:1111.3344 \[gr-qc\]](#).
- [22] R. Gómez, L. Lehner, P. Papadopoulos, and J. Winicour, “The eth formalism in numerical relativity,” Class. Quantum Grav. (01, 1997) , [arXiv:gr-qc/9702002](#).

- [23] J. Winicour, “Newtonian gravity on the null cone,” *J. Math. Phys.* **1193** (1983) .
- [24] W. Magnus, “On the exponential solution of differential equations for a linear operator,” *Commun. Pure Appl. Math.* **7** (1954) 649–673.
- [25] Blanes, S, Casas, F, Oteo, J A, and Ros, J, “The magnus expansion and some of its applications,” *Phys. Rep.* **470 (5-6)** (January, 2009) 151–238, [arXiv:0810.5488](https://arxiv.org/abs/0810.5488) [math-ph].
- [26] J. P. Boyd, *Chebyshev and Fourier Spectral Methods*. Springer-Verlag, Berlin, 1989.
- [27] J. C. Adams and P. N. Swarztrauber, “Spherepack 3.0.”
<http://www.scd.ucar.edu/css/software/spherepack>.
- [28] Hufenberger, Kevin M and Wandelt, Benjamin D, “Fast and exact spin-s spherical harmonic transforms,” *Astro. J. Sup. Ser.* **189** (2010) 255–260, [arXiv:1007.3514](https://arxiv.org/abs/1007.3514) [astro-ph.IM].
- [29] M. Babiuc, B. Szilágyi, I. Hawke, and Y. Zlochower, “Gravitational wave extraction based on Cauchy-characteristic extraction and characteristic evolution,” *Class. Quantum Grav.* **22** no. 23, (2005) 5089–5107, [arXiv:gr-qc/0501008](https://arxiv.org/abs/gr-qc/0501008).
<http://stacks.iop.org/0264-9381/22/5089>.

Appendix A. Regularizing Divergent Equations Using Integration by Parts

This appendix describes the process of future null infinity regularization using integration by parts. A Laurent series is an expansion about a pole of (in this case) finite order. It is the logical extension of a Taylor series to functions that diverge in well defined ways.

We wish to radially integrate the following equation.

$$(r^2 Q)_{,\rho} = A + \frac{B}{1-\rho} + \frac{C}{(1-\rho)^2} + \frac{D}{(1-\rho)^3} . \quad (\text{A.1})$$

Note that $r = R\rho/(1-\rho)$, so both sides are infinite at $\rho = 1$.

The most divergent term is the D term — we integrate by parts.

$$\int \frac{D}{(1-\rho)^3} d\rho = \frac{D/2}{(1-\rho)^2} - \int \frac{D'/2}{(1-\rho)^2} d\rho. \quad (\text{A.2})$$

In practise, limits of integration are $\rho \in [1/2, 1]$ where $\rho = 1/2$ is the worldtube inner boundary of the domain.

This term is now an integral of the same order as the term in C , as well as a term external to the integral that is of the same order. This is cancelled out through division by $r^2 = R^2 \rho^2 / (1-\rho)^2$. In this way, all the terms are regularized, i.e., finite throughout the domain. We include the $D'/2$ term in the C integral, and so on.

$$\begin{aligned} \int \frac{-C + D'/2}{(1-\rho)^2} d\rho &= \int \frac{\partial}{\partial \rho} \left(\frac{1}{1-\rho} \right) (-C + D'/2) d\rho \\ &= \frac{-C + D'/2}{1-\rho} - \int \frac{-C' + D''/2}{1-\rho} d\rho, \end{aligned} \quad (\text{A.3})$$

$$\begin{aligned} \int \frac{B - C' + D''/2}{1-\rho} d\rho &= \\ &- (B - C' + D''/2) \log(1-\rho) + \int (B' - C'' + D'''/2) \log(1-\rho) d\rho, \end{aligned} \quad (\text{A.4})$$

$$\begin{aligned} \int (B' - C'' + D'''/2) \log(1-\rho) d\rho &= \\ &- (B' - C'' + D'''/2) (\rho + (1-\rho) \log(1-\rho)) \\ &+ \int (B'' - C''' + D''''/2) (\rho + (1-\rho) \log(1-\rho)) d\rho. \end{aligned} \quad (\text{A.5})$$

Crucially, the integral term is now bounded in the domain. This means it can be computed numerically. Computationally, the limits of integration are enforced by subtracting the value of the function on the inner boundary. Q_0 is the boundary value of Q . Combining terms, equation 3.11 can be expressed:

$$\begin{aligned}
Q = & Q_0 + \frac{D}{2\rho^2 R^2} - (-C + D'/2) \frac{1-\rho}{\rho^2 R^2} - (B - C' + D''/2) \frac{(1-\rho)^2 \log(1-\rho)}{\rho^2 R^2} \\
& - (B' - C'' + D'''/2) \frac{(\rho + (1-\rho)\log(1-\rho))(1-\rho)^2}{\rho^2 R^2} \\
& + \frac{(1-\rho)^2}{\rho^2 R^2} \int A + (B'' - C''' + D''''/2)(\rho + (1-\rho)\log(1-\rho)) . \tag{A.6}
\end{aligned}$$

Appendix B. Inner Boundary Algorithm Formalism

The boundary algorithm formalism is drawn from Bishop *et al.*[16]. It begins with metric quantities on the worldtube forming the boundary between the space-like foliated numerical GR simulation and the null-foliated CCE domain. It calculates several intermediate helper quantities to simplify the computational complexity. Finally, it produces boundary values for each of the hypersurface or Bondi metric quantities. Note that all quantities in this section refer to inner boundary values only.

Appendix B.1. Initial Metric Quantities

The Metric Quantities are extracted directly from the simulation. They are the covariant 3-metric g_{ij} , the contravariant 3-metric $g^{ij} = (g_{ij})^{-1}$, the co- and contravariant 3-metric derivatives $g_{ij,\alpha}$ and $g^{ij},_{\alpha}$ (calculated using $g^{ij},_{\gamma} = -g^{ik}g^{jl}g_{kl,\gamma}$), and their 4-metric counterparts. The time components are calculated

from the lapse $\alpha = \sqrt{g_{i0}\beta^i - g_{00}}$ and shift $\beta^i = g^{ij}g_{j0}$ as follows.

$$g_{k0} = g_{0k} = g_{ki}\beta^i , \quad (\text{B.1})$$

$$g_{00} = g_{i0}\beta^i - \alpha^2 = g_{ik}\beta^i\beta^k - \alpha^2 , \quad (\text{B.2})$$

$$g_{k0,\gamma} = g_{0k,\gamma} = (g_{ki}\beta^i)_{,\gamma} = g_{ki,\gamma}\beta^i + g_{ki}\beta^i_{,\gamma} , \quad (\text{B.3})$$

$$g_{00,\gamma} = g_{i0,\gamma}\beta^i + g_{i0}\beta^i_{,\gamma} - 2\alpha\alpha_{,\gamma} , \quad (\text{B.4})$$

$$g^{\alpha\beta}_{,\gamma} = -g^{\alpha\delta}g^{\beta\epsilon}g_{\delta\epsilon,\gamma} . \quad (\text{B.5})$$

Appendix B.2. Intermediate Quantities

Additional spherical derivatives are calculated by evaluating the angular derivatives of the spherical harmonic expansions of the quantities on the worldtube.

Appendix B.2.1. Jacobians To perform coordinate transformations, Jacobians and their derivatives were derived. They included the spherical-to-Cartesian $\Lambda_i^{(r,A)}$ and its derivative $\Lambda_i^{(r,A)}_{,\alpha}$, the Cartesian-to-spherical $\Lambda^i_{(r,A)}$ and its derivative $\Lambda^i_{(r,A),\alpha}$.

Appendix B.2.2. Null Generator We calculate the unit normal vectors to the time slice (n^γ) and the sphere (s^γ) to calculate the null generator (l^γ).

$$n^\gamma = (1/\alpha, -\beta^i/\alpha) , \quad (\text{B.6})$$

$$s^\gamma = (0, \frac{g^{ij}x_j}{\sqrt{g^{ij}x_i x_j}}) , \quad (\text{B.7})$$

$$l^\gamma = \frac{n^\gamma + s^\gamma}{\alpha - \beta^i s^j g_{ij}} . \quad (\text{B.8})$$

Their time derivatives are

$$n^\alpha{}_{,t} = \frac{1}{\alpha^2} (-\alpha_{,t}, \alpha_{,t} \beta^i - \alpha \beta^i{}_{,t}) , \quad (\text{B.9})$$

$$s^i{}_{,t} = (-g^{im} + s^i s^m / 2) g_{mn,t} s^n , \quad (\text{B.10})$$

$$s^\alpha{}_{,t} = (0, s^i{}_{,t}) , \quad (\text{B.11})$$

$$l^\alpha{}_{,t} = \frac{n^\alpha{}_{,t} + s^\alpha{}_{,t} - l^\alpha \alpha_{,t} + l^\alpha (g_{ij,t} \beta^i s^j + g_{ij} \beta^i{}_{,t} s^j + g_{ij} \beta^i s^j{}_{,t})}{\alpha - g_{ij} \beta^i s^j} . \quad (\text{B.12})$$

Appendix B.2.3. (Affine) Spherical Metric Quantities Dramatic simplification is possible by calculating a number of auxiliary metric terms in a spherical coordinate system. Here, ${}_{,\lambda}$ denotes a derivative in the null direction, whereas A, B, C etc sub- and superscripts denote indices across the spherical components of the coordinate system, i.e. θ and ϕ .

$$g_{\alpha\beta,\lambda} = l^\gamma g_{\alpha\beta,\gamma} , \quad (\text{B.13})$$

$$\eta_{AB} = \Lambda_A^i \Lambda_B^j g_{ij} , \quad (\text{B.14})$$

$$\eta_{AB,\lambda} = \Lambda_A^k \Lambda_B^l g_{kl,\lambda} + (l^\mu{}_{,A} \Lambda_B^l + l^\mu{}_{,B} \Lambda_A^l) g_{\mu l} , \quad (\text{B.15})$$

$$\eta_{AB,t} = \Lambda_A^i \Lambda_B^j g_{ij,t} , \quad (\text{B.16})$$

$$\eta_{uA,\lambda} = l^t{}_{,A} g_{tt} + \Lambda_A^k g_{tk,\lambda} + l^k{}_{,A} g_{tk} + \Lambda_A^k l^\mu{}_{,t} g_{\mu k} . \quad (\text{B.17})$$

The contravariant quantities are similarly defined.

$$\eta^{AB} \eta_{BC} = \delta_C^A , \quad (\text{B.18})$$

$$\eta^{A\lambda} = \eta^{AB} \Lambda_B^k g_{tk} , \quad (\text{B.19})$$

$$\eta^{\lambda\lambda} = -g_{tt} + \eta^{A\lambda} \Lambda_A^k g_{tk} , \quad (\text{B.20})$$

$$\eta^{AB}{}_{,\lambda} = -\eta^{AC} \eta^{BD} \eta_{CD,\lambda} , \quad (\text{B.21})$$

$$\eta^{A\lambda}{}_{,\lambda} = \eta^{AB} \eta_{uA,\lambda} - \eta^{AB} \eta^{C\lambda} \eta_{CB,\lambda} . \quad (\text{B.22})$$

Appendix B.2.4. Dyad Quantities The dyad allows construction of spin-weighted scalars on the sphere. Given $r = \sqrt{x^2 + y^2 + z^2}$,

$$q^i = \frac{1}{r\sqrt{x^2 + y^2}} (-xz + iyr, -yz - ixr, x^2 + y^2) , \quad (\text{B.23})$$

$$q_A = \Lambda_A^i q^i / r , \quad (\text{B.24})$$

since $q_i = q^i$. Explicitly,

$$q_A = \left(-1, -i\frac{r_c}{r} \right) , \quad (\text{B.25})$$

$$q^A = \left(-1, -i\frac{r}{r_c} \right) , \quad (\text{B.26})$$

where $r_c = \sqrt{x^2 + y^2}$, and its derivatives are defined

$$\begin{aligned} q_{,t}^i &= \frac{1}{r^3 r_c^3} (z((x^4 - y^2(y^2 + z^2))x_{,t} + xy(2r_c^2 + z^2)y_{,t}) - xr_c^4 z_{,t} + ir^3(x(-yx_{,t} + xy_{,t})), \\ &\quad z(xy(2r_c^2 + z^2)x_{,t} - (x^4 - y^4 + x^2 z^2)y_{,t}) - yr_c^4 z_{,t} + ir^3(y(-yx_{,t} + xy_{,t})), \\ &\quad r_c^2(z(z(xx_{,t} + yy_{,t}) - r_c^2 z_{,t}))) , \end{aligned} \quad (\text{B.27})$$

$$q_{,x}^i = \frac{1}{r^3 r_c^3} (z(x^4 - y^2(y^2 + z^2)) - ir^3 xy, xyz(2r_c^2 + z^2) - ir^3 y^2, xz^2 r_c^2) , \quad (\text{B.28})$$

$$q_{,y}^i = \frac{1}{r^3 r_c^3} (xyz(2r_c^2 + z^2) + ix^2 r^3, -z(x^4 - y^4 + x^2 z^2) + ixyr^3, yz^2 r_c^2) , \quad (\text{B.29})$$

$$q_{,z}^i = \frac{r_c}{R^3} (-x, -y, -z) . \quad (\text{B.30})$$

Then $q^i_{,\lambda} = l^\alpha q^i_{,\alpha}$. Note that the q^i are not necessarily constant ($q^i_{,t} \neq 0$) as the properties of the worldtube are time-dependent. This approach differs from the Pitt null code.

Appendix B.2.5. The Bondi r The Bondi radius r_b is an areal radius, not a coordinate radius. The value of the Bondi radius r_b at every point on the worldtube provides the compactification parameter. Given $|q_{AB}| = \sin^2 \theta = \frac{x^2 + y^2}{x^2 + y^2 + z^2}$,

$$r_b = \left(\frac{|\eta_{AB}|}{|q_{AB}|} \right)^{\frac{1}{4}}, \quad (\text{B.31})$$

$$r_{b,\lambda} = \frac{r_b}{4} \eta^{AB} \eta_{AB,\lambda}, \quad (\text{B.32})$$

$$r_{b,t} = \frac{r_b}{4} \eta^{AB} \eta_{AB,t}. \quad (\text{B.33})$$

In contrast, derivatives of the coordinate radius r are

$$r_{,\lambda} = l^\alpha r_{,\alpha}, \quad (\text{B.34})$$

$$r_{,t} = \frac{xx_{,t} + yy_{,t} + zz_{,t}}{r}, \quad (\text{B.35})$$

$$r_{,\alpha} = \frac{1}{r} (x^i x_{i,t}, x^i). \quad (\text{B.36})$$

In the present algorithm the cartesian extraction radius r is held constant, but derivatives are included for the general case of a variable extraction coordinate radius.

Appendix B.2.6. Derivatives of Hypersurface Quantities Calculation of Q and $\Phi = J_{,u}$ require the null-derivatives of several other hypersurface quantities.

$$\beta_{,\lambda} = \frac{r_b}{8r_{b,\lambda}} \left(J_{,\lambda} \bar{J}_{,\lambda} - \frac{1}{1 + J\bar{J}} \mathbb{R}(\bar{J}J_{,\lambda})^2 \right), \quad (\text{B.37})$$

$$J_{,\lambda} = 2J \left(\frac{r_{,\lambda}}{r} - \frac{r_{b,\lambda}}{r_b} \right) + \frac{r^2}{r_b^2} (g_{ij} q^i_{,\lambda} q^j + \frac{1}{2} g_{ij,\lambda} q^i q^j), \quad (\text{B.38})$$

$$U_{,\lambda} = 2\beta_{,\lambda} U + 2\beta_{,\lambda} \eta^{A\lambda} q_A - \eta^{A\lambda}_{,\lambda} q_A - r_{b,\lambda B} \eta^{AB} q_A + r_{b,B} \eta^{AB}_{,\lambda} q_A. \quad (\text{B.39})$$

Appendix B.3. Hypersurface Quantities

The hypersurface quantities are J , K , β , U , Q , and W , as well as the time derivative $J_{,u}$.

$$J = \frac{r^2}{2r_b^2} g_{ij} q^i q^j, \quad (\text{B.40})$$

$$\Phi = J_{,u} = 2J \left(\frac{r_{,t}}{r} - \frac{r_{b,t}}{r_b} \right) + \frac{r^2}{r_b^2} (g_{ij} q^i{}_{,t} q^j + \frac{1}{2} g_{ij,t} q^i q^j), \quad (\text{B.41})$$

$$K = \sqrt{1 + J\bar{J}}, \quad (\text{B.42})$$

$$\beta = -\frac{1}{2} \log(r_{b,\lambda}), \quad (\text{B.43})$$

$$U = -\left(\eta^{\lambda A} + \frac{r_{b,B}}{r_{b,\lambda}} \eta^{AB} \right) q_A, \quad (\text{B.44})$$

$$Q = r_b^2 (J\bar{U}_{,\lambda} + \sqrt{1 + J\bar{J}} U_{,\lambda}), \quad (\text{B.45})$$

$$W = \frac{r_{b,\lambda} \eta^{\lambda\lambda}}{r_b} - \frac{2r_{b,u}}{r_b} - \frac{1}{r_b} + \frac{2r_{b,A} \eta^{A\lambda}}{r_b} + \frac{r_{b,A} r_{b,B} \eta^{AB}}{r_{b,\lambda} r_b}. \quad (\text{B.46})$$

Appendix B.4. Bondi Metric Reconstruction

J , K , β , U , Q , and W can be combined to reconstruct the Bondi metric, with standard coordinate 4-vector ordering (u, r, θ, ϕ) [20].

$$\eta^{\alpha\beta} = \begin{pmatrix} 0 & -e^{-2\beta} & 0 & 0 \\ -e^{-2\beta} & (rW + 1)e^{-2\beta} & \frac{1}{2}(U + \bar{U})e^{-2\beta} & -\frac{ir}{2r_c}(U - \bar{U})e^{-2\beta} \\ 0 & \frac{1}{2}(U + \bar{U})e^{-2\beta} & \frac{1}{2r^2}(2K - J - \bar{J}) & \frac{i}{2rr_c}(J - \bar{J}) \\ 0 & -\frac{ir}{2r_c}(U - \bar{U})e^{-2\beta} & \frac{i}{2rr_c}(J - \bar{J}) & \frac{1}{2r_c^2}(2K + J + \bar{J}) \end{pmatrix}, \quad (\text{B.47})$$

$$\eta_{\alpha\beta} = \begin{pmatrix} -(rW + 1)e^{2\beta} & \frac{r^2}{2}((J + K)\bar{U} & \frac{irr_c}{2}(\bar{J}U - J\bar{U}) \\ +\frac{r^2}{2}(2KU\bar{U} + J\bar{U}^2 + \bar{J}U^2) & -e^{2\beta} + (\bar{J} + K)U & +K(\bar{U} - U) \\ -e^{2\beta} & 0 & 0 & 0 \\ \frac{r^2}{2}((J + K)\bar{U} + (\bar{J} + K)U) & 0 & \frac{r^2}{2}(J + \bar{J} + 2K) & \frac{irr_c}{2}(\bar{J} - J) \\ \frac{irr_c}{2}(\bar{J}U - J\bar{U} + K(\bar{U} - U)) & 0 & \frac{irr_c}{2}(\bar{J} - J) & -\frac{r_c^2}{2}(J + \bar{J} - 2K) \end{pmatrix}. \quad (\text{B.48})$$

Appendix C. $\bar{\partial}$ Operator and Spin-Weighted Spherical Harmonics

The hypersurface equations are written making use of the $\bar{\partial}$ formalism[22], which simplifies equations with spherical symmetry. In our implementation, we use a basis capable of multiple values on the poles, so only a single patch is necessary to cover the entire sphere.

Rank 2 tensors on the sphere can be broken down and expressed as a sum of spin-weighted spherical harmonics when contracted with an appropriate dyad q^A . Following [22](Eqn. 8), a generic tensor can be written as the sum of respectively a symmetric trace free part, a trace part, and an antisymmetric part:

$$w_{AB} = t_{AB} + \frac{p}{2}q_{AB} + i\frac{u}{4}(q_A\bar{q}_B - \bar{q}_Aq_B) . \quad (\text{C.1})$$

$p = q^{CD}w_{CD}$ and $u = i(q^C\bar{q}^D - \bar{q}^Cq^D)w_{CD}/2$ are both real scalar fields with spin-weight 0. Writing $t = t_{AB}q^Aq^B$ yields a complex scalar field with spin-weight 2. Together, these three scalars p , u , and t completely specify the tensor field independent of choice of basis.

$\bar{\partial}$ is a spherical derivative operator on spin-weighted spherical harmonics. In spherical coordinates,

$$\bar{\partial}\eta = -(\sin^s\theta) \left(\frac{\partial}{\partial\theta} + \frac{i}{\sin\theta} \frac{\partial}{\partial\phi} \right) (\sin^{-s}\theta\eta) , \quad (\text{C.2})$$

$$\bar{\partial}\eta = -(\sin^{-s}\theta) \left(\frac{\partial}{\partial\theta} - \frac{i}{\sin\theta} \frac{\partial}{\partial\phi} \right) (\sin^s\theta\eta) . \quad (\text{C.3})$$

This can be thought of as a contraction of the dyad with the spherical derivatives operator.

In terms of spin-weighted spherical harmonics,

$$\bar{\partial}({}_sY_{lm}) = +\sqrt{(l-s)(l+s+1)}_{s+1}Y_{lm} , \quad (\text{C.4})$$

$$\bar{\partial}({}_sY_{lm}) = -\sqrt{(l+s)(l-s+1)}_{s+1}Y_{lm} . \quad (\text{C.5})$$

Used in combination, these definitions allow the $\bar{\partial}$ formalism to be used in the spectral domain. We used the package Spinsfast[28] to implement spin-weighted spherical harmonics.

$\bar{\partial}$ assumes a spherical domain. However, in general the compactification parameter $R = r_{b|\Gamma}$ is not constant on the sphere. The corrected operation is

$$\bar{\partial}\eta = \tilde{\bar{\partial}}\eta - \eta_{,\rho} \frac{\rho(1-\rho)}{R} \tilde{\bar{\partial}}R, \quad (\text{C.6})$$

where $\tilde{\bar{\partial}}$ denotes the naive operator in the affine coordinate system.

This correction is the same that operates at the end of the calculation of $J_{,u} = \Phi$ in Appendix D, only in reverse[29].

Appendix D. All Evolution Algorithm Terms

These are largely drawn from Bishop *et al.*[20], with some re-arrangement of terms to ensure internal consistency with the Magnus expansion formalism, and the compactification transformation $\rho = r/(R+r)$. Additionally, terms are grouped by their order in the Laurent expansion, where relevant.

Appendix D.1. β terms

$$\beta_{,r} = N_{\beta}, \quad (\text{D.1})$$

$$N_{\beta} = \frac{\rho(1-\rho)^3}{8R} (J_{,\rho} \bar{J}_{,\rho} - K^2_{,\rho}). \quad (\text{D.2})$$

Appendix D.2. Q terms

$$(r^2 Q)_{,\rho} = \frac{Q_C + Q_{CNL}}{(1-\rho)^2} + \frac{Q_D}{(1-\rho)^3}. \quad (\text{D.3})$$

$$Q_C = -R^2 \rho^2 \bar{\partial} J_{,\rho} - R^2 \rho^2 \bar{\partial} K_{,\rho} + 2R^2 \rho^2 \bar{\partial} \beta_{,\rho} , \quad (\text{D.4})$$

$$Q_{CNL} = R^2 \rho^2 (1 - K) (\bar{\partial} K_{,\rho} + \bar{\partial} J_{,\rho}) + \bar{J} \bar{\partial} J_{,\rho} + J_{,\rho} \bar{J}_{,\rho} + J \bar{\partial} K_{,\rho} \\ + K_{,\rho} \bar{\partial} J - J_{,\rho} \bar{\partial} K + \frac{\bar{\partial} \bar{J} (J_{,\rho} - J^2 \bar{J}_{,\rho}) + \bar{\partial} J (\bar{J}_{,\rho} - \bar{J}^2 J_{,\rho})}{2K^2} , \quad (\text{D.5})$$

$$Q_D = -4R^2 \rho \bar{\partial} \beta . \quad (\text{D.6})$$

Appendix D.3. U terms

$$U_{,\rho} = U_A + U_{ANL} . \quad (\text{D.7})$$

$$U_A = \frac{e^{2\beta}}{R\rho^2} Q , \quad (\text{D.8})$$

$$U_{ANL} = \frac{e^{2\beta}}{R\rho^2} (KQ - Q - J\bar{Q}) . \quad (\text{D.9})$$

Appendix D.4. W terms

$$(r^2 W)_{,\rho} = \frac{W_C + W_{CNL}}{(1 - \rho)^2} + \frac{W_D}{(1 - \rho)^3} . \quad (\text{D.10})$$

$$W_C = \mathcal{R} - R^2 e^{2\beta} (\bar{\partial} \beta \bar{\partial} \beta + \bar{\partial} \bar{\partial} \beta) + \frac{R^2 \rho^2}{4} (\bar{\partial} \bar{U}_{,\rho} + \bar{\partial} U_{,\rho}) , \quad \text{where} \quad (\text{D.11})$$

$$\mathcal{R} = \frac{R e^{2\beta}}{2} \left(2K - \bar{\partial} \bar{\partial} K + \frac{1}{2} (\bar{\partial}^2 J + \bar{\partial}^2 \bar{J}) + \frac{1}{4K} (\bar{\partial} \bar{J} \bar{\partial} J - \bar{\partial} J \bar{\partial} \bar{J}) \right) , \quad (\text{D.12})$$

$$W_{CNL} = R e^{2\beta} \left((1 - K) (\bar{\partial} \bar{\partial} \beta + \bar{\partial} \beta \bar{\partial} \beta) + \frac{1}{2} (J \bar{\partial} \beta^2 + \bar{J} \bar{\partial} \beta^2) \right. \\ \left. - \frac{1}{2} (\bar{\partial} \beta (\bar{\partial} K - \bar{\partial} \bar{J}) + \bar{\partial} \beta (\bar{\partial} K - \bar{\partial} J)) + \frac{1}{2} (J \bar{\partial}^2 \beta + \bar{J} \bar{\partial}^2 \beta) \right) \\ - e^{2\beta} \frac{R^3 \rho^4}{8} (2K U_{,\rho} \bar{U}_{,\rho} + J \bar{U}_{,\rho}^2 + \bar{J} U_{,\rho}^2) , \quad (\text{D.13})$$

$$W_D = R^2 \rho (\bar{\partial} \bar{U} + \bar{\partial} U) . \quad (\text{D.14})$$

Appendix D.5. $J_u = \Phi$ terms

$$(r\Phi)_{,\rho} - (rJ)(\Phi\bar{\Gamma} + \bar{\Phi}\Gamma) = \Phi_A + \Phi_{ANL} + \frac{\Phi_B + \Phi_{BNL}}{1 - \rho} + \frac{\Phi_C + \Phi_{CNL}}{(1 - \rho)^2} . \quad (\text{D.15})$$

$$\Gamma = \left(J_{,\rho} - J \frac{K_{,\rho}}{K} \right) . \quad (\text{D.16})$$

$$\Phi_A = (1 - \rho)J_{,\rho} + \frac{1}{2}R\rho^2 W_{,\rho} J_{,\rho} + \frac{\rho}{2}(1 - \rho + R\rho W)J_{,\rho\rho} , \quad (\text{D.17})$$

$$\Phi_B = \left(\frac{3}{2}R\rho - R\rho^2 \right) W J_{,\rho} - \frac{1}{2}R\rho \bar{\partial}U_{,\rho} + \frac{e^{2\beta}}{\rho} (\bar{\partial}^2\beta + \bar{\partial}\beta^2) , \quad (\text{D.18})$$

$$\Phi_C = -R\bar{\partial}U , \quad (\text{D.19})$$

$$\Phi_{ANL} = -4J\beta_{,\rho} , \quad (\text{D.20})$$

$$\begin{aligned} \Phi_{BNL} = & N_{1B} + N_{2B} + N_{3B} + N_{4B} + N_{5B} + N_{6B} + N_{7B} \\ & + P_{1B} + P_{2B} + P_{3B} + P_{4B} , \end{aligned} \quad (\text{D.21})$$

$$\Phi_{CNL} = N_{2C} + N_{3C} + P_{3C} . \quad (\text{D.22})$$

N terms are as in Bishop *et al.*[20], with a prefactor $\frac{R}{2(1-\rho)^2}$ and the usual compactification transformation.

$$N_{1B} = -\frac{e^{2\beta}}{2\rho} (K(\partial J \bar{\partial} \beta + 2\partial K \bar{\partial} \beta - \bar{\partial} J \partial \beta) + J(\bar{\partial} J \bar{\partial} \beta - 2\partial K \bar{\partial} \beta) - \bar{J} \partial J \bar{\partial} \beta) , \quad (\text{D.23})$$

$$N_{2B} = -\frac{R\rho}{4} (\partial J \bar{U}_{,\rho} + \bar{\partial} J U_{,\rho}) , \quad (\text{D.24})$$

$$N_{2C} = -\frac{R}{2} (\partial J \bar{U} + \bar{\partial} J U) , \quad (\text{D.25})$$

$$N_{3B} = \frac{R\rho}{2} ((1-K)\partial U_{,\rho} - J\partial \bar{U}_{,\rho}) , \quad (\text{D.26})$$

$$N_{3C} = R(1-K)\partial U - RJ\partial \bar{U} , \quad (\text{D.27})$$

$$N_{4B} = \frac{e^{-2\beta}}{4} R^2 \rho^3 (K^2 U^2_{,\rho} + 2JKU_{,\rho} \bar{U}_{,\rho} + J^2 \bar{U}^2_{,\rho}) , \quad (\text{D.28})$$

$$N_{5B} = -\frac{R\rho}{4} J_{,\rho} (\partial \bar{U} + \bar{\partial} U) , \quad (\text{D.29})$$

$$N_{6B} = \frac{R\rho}{2} \left(\frac{1}{2} (\bar{U} \partial J + U \bar{\partial} J) (J \bar{J}_{,\rho} - \bar{J} J_{,\rho}) + \bar{U} \bar{\partial} J (JK_{,\rho} - K J_{,\rho}) - \bar{U} (\partial J_{,\rho} - 2K \partial K J_{,\rho} + 2J \partial K K_{,\rho}) - U (\bar{\partial} J_{,\rho} - K \bar{\partial} \bar{J} J_{,\rho} + J \bar{\partial} \bar{J} K_{,\rho}) \right) , \quad (\text{D.30})$$

$$N_{7B} = \frac{R\rho}{2} (K J_{,\rho} - J K_{,\rho}) (\bar{U} (\bar{\partial} J - \partial K) + U (\bar{\partial} K - \partial \bar{J}) + K (\bar{\partial} U - \partial \bar{U}) + (J \bar{\partial} \bar{U} - \bar{J} \partial U)) . \quad (\text{D.31})$$

P terms are as in Bishop *et al.*[20] except for the terms in $J_{,u}$, which have been moved to the left hand side of the equation. They have a prefactor $\frac{J}{2\rho(1-\rho)}$ and the

usual compactification transformation.

$$P_{1A} = -4J\beta_{,\rho} , \quad (\text{D.32})$$

$$P_{1B} = -4R\rho J\beta_{,\rho} W , \quad (\text{D.33})$$

$$P_{2B} = \frac{e^{2\beta}}{2\rho} J \left(-2K(\bar{\partial}\bar{\partial}\beta + \bar{\partial}\beta\bar{\partial}\beta) - (\bar{\partial}\beta\bar{\partial}K + \bar{\partial}\beta\bar{\partial}K) + J(\bar{\partial}^2\beta + \bar{\partial}\beta^2) \right. \\ \left. + \bar{J}(\bar{\partial}^2\beta + \bar{\partial}\beta^2) + (\bar{\partial}J\bar{\partial}\beta + \bar{\partial}\bar{J}\bar{\partial}\beta) \right) , \quad (\text{D.34})$$

$$P_{3B} = \frac{R\rho}{4} J(\bar{\partial}U_{,\rho} + \bar{\partial}\bar{U}_{,\rho}) , \quad (\text{D.35})$$

$$P_{3C} = \frac{R}{2} J(\bar{\partial}U + \bar{\partial}\bar{U}) , \quad (\text{D.36})$$

$$P_{4B} = -\frac{e^{-2\beta}}{2} R^2 \rho^3 J (2KU_{,\rho}\bar{U}_{,\rho} + J\bar{U}^2_{,\rho} + \bar{J}U^2_{,\rho}) . \quad (\text{D.37})$$

The non-spherical and non-constant inner boundary creates a discrepancy between the Bondi and affine coordinates. The corrective factor is given by

$$f_{,\tilde{u}} = f_{,u} + f_{,r} r_{,u} = f_{,u} + \rho(1 - \rho) \frac{R_{,u}}{R} f_{,\rho} , \quad (\text{D.38})$$

where once again $_{,\tilde{u}}$ denotes a derivative performed in the affine coordinate system, whereas $_{,u}$ is the regular derivative in the Bondi coordinate system. Time steps are performed in the affine coordinate system, whereas the hypersurface equations are calculated and solved in the Bondi coordinate system.

This term must be added at the end of the calculation in any instance where $R_{,u}$ is nonzero.

Chapter 4 – Gauge free Bondi news

Following the completion of the Spectral Characteristic Evolution algorithm, Béla and I pushed to complete a news extraction capability before he took up a position at JPL. In collaboration with Jeffrey Winicour, we adapted the method used in the Pitt null code and were able to produce consistent and convergent results in relatively short order.

The characteristic evolution algorithm allows the reconstruction of the conformal metric at \mathcal{I}^+ . This metric contains all the far-field gravitational wave information, but remains scrambled by gauge effects. It is possible to write down a formula for the unscrambled Bondi news in terms of the conformal metric by effectively performing a transformation. While this calculation is quite involved, it is the most computationally lean method to extract the news and forms an excellent baseline alternative to the Pitt null code for later development. An inertial coordinate system was defined and evolved at \mathcal{I}^+ , onto which the news was interpolated before being transformed into its constituent spin-weighted spherical harmonic modes.

The main technical challenge we faced in this paper was demonstrating both gauge invariance and consistency with the Pitt null code. To show gauge invariance, Béla Szilágyi produced two **SpEC** head-on black hole collisions in two different gauges. While physically the same, their coordinate systems were very different. Both codes removed gauge effects so effectively it was difficult to assess their comparative performance however, with a worldtube extraction radius comparable to the initial distance between the black holes, the gauge effects were significant enough that they dominated over other sources of error. In order to gain comparable results, **SpEC**'s resolution had to be substantially decreased, at which point it didn't resolve all the features of the junk radiation. Conversely, Pitt null code's non-spectral methods struggled to resolve rapid motion of the worldtube at the test extraction radius. In search of a sufficiently challenging test case, we operated both codes far beyond their nominal use cases. Despite these challenges, we found that gauge-contaminated news differed between the runs in both Pitt and **SpEC** by more than the implied error, while the gauge-free

news agreed to within that same implied error across all codes and runs.

With the completion of the Bondi news extraction module, spectral characteristic extraction was functionally complete. The code was finalized and is already being used as a preferred alternative to the Pitt null code for Cauchy characteristic extraction.

The paper was submitted to CQG on February 27, 2015, and was published on November 2015 with minor revisions. <http://arxiv.org/abs/1502.06987>

Gauge Invariant Spectral Cauchy Characteristic Extraction

Casey J. Handmer¹, Béla Szilágyi¹, Jeffrey Winicour²

¹Theoretical Astrophysics 350-17, California Institute of Technology, Pasadena,
California 91125, USA

²Department of Physics and Astronomy University of Pittsburgh, Pittsburgh, PA
15260, USA

E-mail: chandmer@caltech.edu

Abstract. We present gauge invariant spectral Cauchy characteristic extraction. We compare gravitational waveforms extracted from a head-on black hole merger simulated in two different gauges by two different codes. We show rapid convergence, demonstrating both gauge invariance of the extraction algorithm and consistency between the legacy Pitt null code and the much faster Spectral Einstein Code (SpEC).

1. What is CCE? What is gravitational waveform gauge invariance?

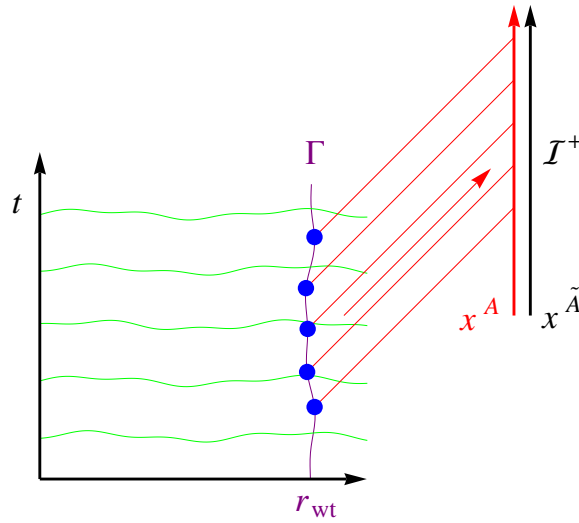


Figure 1: Cauchy characteristic extraction. A Cauchy evolution of the Einstein field equation proceeds on a space-like foliation (green). A finite spheroidal worldtube Γ at areal radius r_{wt} forms the inner boundary to a characteristic evolution on a null foliation (red). Based on a coordinate system x^A derived from the Cauchy data on the worldtube, gravitational information is propagated to compactified future null infinity \mathcal{I}^+ . At \mathcal{I}^+ an inertial coordinate system $x^{\tilde{A}}$ is co-evolved, in which the desired gauge-invariant waveform can be expressed.

The strong gravitational radiation produced in the inspiral and merger of binary black holes has been a dominant motivation for the construction of gravitational wave observatories. The details of the gravitational waveform supplied by numerical simulation is a key theoretical tool to fully complement the sensitivity of the LIGO, Virgo, GEO, and KAGRA observatories, by enhancing detection and providing useful scientific interpretation of the gravitational signal[1, 2, 3, 4]. Characteristic evolution coupled to Cauchy evolution via Cauchy-characteristic extraction (CCE) provides the most accurate numerical computation of the Bondi news function, which determines both the waveform and the radiated energy and momentum at null infinity.

In CCE, the Cauchy evolution is used to supply boundary data on a timelike inner worldtube necessary to carry out a characteristic evolution extending to future null infinity \mathcal{I}^+ , where the radiation is computed using the geometric methods developed by Bondi *et al.*[5], Sachs[6], and Penrose[7], as depicted in Fig. 1. More intuitive methods, including intrinsically inertial compactified hyperboloidal formulations[8, 9, 10] have not yet found adoption in the evolution of binary black holes. CCE is an initial-boundary value problem based upon a timelike worldtube[11]. It has been implemented as a characteristic evolution code, the Pitt null code[12, 13], which incorporates a Penrose compactification of the spacetime, and which has subsequently been extended to higher order methods by Reisswig *et al.*[14]. It has more recently been implemented as a spectral code within the Spectral Einstein Code (SpEC) by Handmer and Szilágyi[15], upon which the present work is based.

One technical complication introduced by CCE is that the coordinates induced on \mathcal{I}^+ by the computational Cauchy coordinates on the inner worldtube do not correspond to inertial observers, i.e., to the coordinates intrinsic to a distant freely falling and non-rotating observatory. The gravitational waveform first obtained in the “computational coordinates” of CCE is in a scrambled form. This gauge ambiguity in the waveform is removed by constructing the transformation between computational coordinates and inertial coordinates at \mathcal{I}^+ . There still remains the freedom in the choice of inertial observers. In special relativistic theories, this freedom is reduced to the translations and Lorentz transformations of the Poincaré group. As explained in Sec. 3, in an asymptotically flat space time the corresponding asymptotic symmetry group consists of supertranslations and Lorentz transformations. This freedom governs the redshift and initial phase of the waveform.

A physically relevant calculation of the radiation flux must also be referred

to such inertial coordinates at \mathcal{I}^+ . In this paper, the calculation of the energy-momentum flux via the Bondi news function is first carried out in the induced worldtube coordinates and then transformed to the inertial coordinates.

2. Characteristic Formalism

The characteristic formalism is based upon a family of outgoing null cones emanating from an inner worldtube and extending to infinity where they foliate \mathcal{I}^+ into spherical slices. We let u label these hypersurfaces, y^A ($A = 2, 3$) be angular coordinates that label the null rays, and r be a surface area coordinate along the outgoing null cones.

Employing the conventions used in [15], in the resulting $x^\alpha = (u, r, y^A)$ coordinates, the metric takes the Bondi-Sachs form

$$ds^2 = - \left(e^{2\beta}(rW + 1) - r^2 h_{AB} U^A U^B \right) du^2 - 2e^{2\beta} dudr - 2r^2 h_{AB} U^B dudy^A + r^2 h_{AB} dy^A dy^B, \quad (2.1)$$

where $h^{AB}h_{BC} = \delta_C^A$ and $\det(h_{AB}) = \det(q_{AB})$, with q_{AB} a unit sphere metric. In analyzing the Einstein equations, we also use the intermediate variable

$$Q_A = r^2 e^{-2\beta} h_{AB} U_{,r}^B. \quad (2.2)$$

The metric coefficients $W, h_{AB}, U^A, Q_A, \beta$ represent respectively the mass aspect, the spherical 2-metric, the shift and its radial derivative, and the lapse. The vector and tensor fields h_{AB}, U^A, Q_A are expressed as spin-weighted fields by contracting them with the complex dyad q^A for the unit sphere metric satisfying $q^A q_A = 0$, $q^A \bar{q}_A = 2$, $q^A = q^{AB} q_B$, with $q^{AB} q_{BC} = \delta_C^A$ and $q_{AB} = (q_A \bar{q}_B + \bar{q}_A q_B)/2$. Under this convention, the spin-weighted functions $U = U^A q_A$ and $Q = Q_A q^A$, while $J = h_{AB} q^A q^B/2$ uniquely determines the spherical 2-metric component of the general 4-metric[13]. We chose a dyad consistent with the computational formulation of the

spin-weight raising $\bar{\delta}$ operator [16], given by $q^A = (-1, -i/\sin\theta)$ in standard spherical coordinates (θ, ϕ) . This is regular everywhere except the poles, which we can avoid through careful choice of grid points. It is worth noting that any choice of angular coordinates are possible. Other conventions use multiple patches to avoid singularities at the poles.

A key feature of the Bondi-Sachs formulation is that the Einstein equations can be integrated along the outgoing characteristics in a sequential order. We use a form which first appeared in [17] and was implemented as the Pitt code in [13, 18]:

$$\beta_{,r} = N_\beta , \quad (2.3)$$

$$(r^2 Q)_{,r} = -r^2(\bar{\delta}J + \bar{\delta}K)_{,r} + 2r^4\bar{\delta}(r^{-2}\beta)_{,r} + N_Q , \quad (2.4)$$

$$U_{,r} = r^{-2}e^{2\beta}Q + N_U , \quad (2.5)$$

$$(r^2 W)_{,r} = \frac{1}{2}e^{2\beta}\mathcal{R} - 1 - e^\beta\bar{\delta}\bar{\delta}e^\beta + \frac{1}{4}r^{-2}(r^4(\bar{\delta}\bar{U} + \bar{\delta}U))_{,r} + N_W , \quad (2.6)$$

and the evolution equation

$$2(rJ)_{,ur} = ((1 + rW)(rJ)_{,r})_{,r} - r^{-1}(r^2\bar{\delta}U)_{,r} + 2r^{-1}e^\beta\bar{\delta}^2e^\beta - (rW)_{,r}J + N_J , \quad (2.7)$$

where

$$\mathcal{R} = 2K - \bar{\delta}\bar{\delta}K + \frac{1}{2}(\bar{\delta}^2J + \bar{\delta}^2\bar{J}) + \frac{1}{4K}(\bar{\delta}\bar{J}\bar{\delta}J - \bar{\delta}J\bar{\delta}\bar{J}) , \quad (2.8)$$

is the curvature scalar associated with h_{AB} , $K^2 = 1 + J\bar{J}$ and N_β, N_Q, N_W, N_J are nonlinear terms given in [13].

On each constant u hypersurface of the spacetime foliation, these equations are integrated in turn. Given J , β is solved, then U , Q , and W in turn, enabling the computation of $J_{,u}$. $J_{,u}$ permits a step forward in time and J is thus defined on the next hypersurface. The radial compactification of infinity is given by

$$r = r_{wt}\rho/(1 - \rho) , \quad \frac{1}{2} \leq \rho \leq 1 , \quad (2.9)$$

where the compactification parameter $r_{wt}(u, y^A)$ is the (not necessarily constant) areal radius coordinate on the worldtube.

Angular derivatives are implemented using the action of the $\bar{\delta}$ operator on spin-weighted spherical harmonics, e.g., $\bar{\delta}U = q^A q^B U_{A:B}$, where a colon denotes the covariant derivative with respect to q_{AB} [16]. In spherical coordinates, this takes the explicit form for a spin-weight- s field η

$$\bar{\delta}\eta = -(\sin^s \theta) \left(\frac{\partial}{\partial \theta} + \frac{i}{\sin \theta} \frac{\partial}{\partial \phi} \right) (\sin^{-s} \theta \eta) , \quad (2.10)$$

$$\bar{\delta}\eta = -(\sin^{-s} \theta) \left(\frac{\partial}{\partial \theta} - \frac{i}{\sin \theta} \frac{\partial}{\partial \phi} \right) (\sin^s \theta \eta) . \quad (2.11)$$

$\bar{\delta}$ is the associated spin-weight lowering operator.

The spectral algorithm used to solve these equations and the treatment of the nonlinear terms $N_\beta, N_Q, N_U, N_W, N_J$ are detailed in Handmer and Szilágyi[15]. Here, we extend the characteristic spectral algorithm to calculating the gauge invariant Bondi news at \mathcal{I}^+ .

3. Waveforms at \mathcal{I}^+

For technical simplicity, the theoretical derivation of the waveform at infinity is best presented in terms of an inverse surface-area coordinate $\ell = 1/r$, where $\ell = 0$ at \mathcal{I}^+ . In the resulting $x^\mu = (u, \ell, x^A)$ conformal Bondi coordinates, the physical spacetime metric $g_{\mu\nu}$ has the conformal compactification $\hat{g}_{\mu\nu} = \ell^2 g_{\mu\nu}$, where $\hat{g}_{\mu\nu}$ is smooth at \mathcal{I}^+ and, referring to the metric (2.1), takes the form[11]

$$\begin{aligned} \hat{g}_{\mu\nu} dx^\mu dx^\nu = & - (e^{2\beta}(\ell^2 + \ell W) - h_{AB} U^A U^B) du^2 + 2e^{2\beta} dud\ell \\ & - 2h_{AB} U^B dudx^A + h_{AB} dx^A dx^B . \end{aligned} \quad (3.1)$$

As described in [19, 20], both the Bondi news function $N(u, x^A)$ and the Newman-

Penrose Weyl tensor component [21]

$$\Psi_4^0(u, x^A) = \lim_{r \rightarrow \infty} r \psi_4, \quad (3.2)$$

which describe the waveform, are determined by the asymptotic limit at \mathcal{I}^+ of the tensor field

$$\hat{\Sigma}_{\mu\nu} = \frac{1}{\ell} (\hat{\nabla}_\mu \hat{\nabla}_\nu - \frac{1}{4} \hat{g}_{\mu\nu} \hat{\nabla}^\alpha \hat{\nabla}_\alpha) \ell. \quad (3.3)$$

This limit is constructed from the leading coefficients in an expansion of the metric about \mathcal{I}^+ in powers of ℓ . We thus write

$$h_{AB} = H_{AB} + \ell c_{AB} + O(\ell^2). \quad (3.4)$$

Conditions on the asymptotic expansion of the remaining components of the metric follow from the Einstein equations:

$$\beta = H + O(\ell^2), \quad (3.5)$$

$$U^A = L^A + 2\ell e^{2H} H^{AB} D_B H + O(\ell^2), \quad (3.6)$$

and

$$W = D_A L^A + \ell (e^{2H} \mathcal{R}/2 + D_A D^A e^{2H} - 1) + O(\ell^2), \quad (3.7)$$

where H and L are the asymptotic limits of β and U and where \mathcal{R} and D_A are the 2-dimensional curvature scalar and covariant derivative associated with H_{AB} .

The expansion coefficients H , H_{AB} , c_{AB} , and L^A (all functions of u and x^A) completely determine the radiation field. One can further specialize the Bondi coordinates to be inertial at \mathcal{I}^+ , i.e., have Minkowski form, in which case $H = L^A = 0$, $H_{AB} = q_{AB}$ (the unit sphere metric) so that the radiation field is completely determined by c_{AB} . However, the characteristic extraction of the waveform is carried out in computational coordinates (determined by the Cauchy data on the extraction worldtube) so this inertial simplification cannot be assumed.

In order to first compute the Bondi news function in the $\hat{g}_{\mu\nu}$ computational frame, it is necessary to determine the conformal factor ω relating H_{AB} to a unit sphere metric Q_{AB} , i.e., to an inertial conformal Bondi frame[11] satisfying

$$Q_{AB} = \omega^2 H_{AB} . \quad (3.8)$$

(See [22] for a discussion of how the news in an arbitrary conformal frame is related to its expression in this inertial Bondi frame.) We can determine ω by solving the elliptic equation governing the conformal transformation of the curvature scalar (2.8) to a unit sphere geometry:

$$\mathcal{R} = 2(\omega^2 + H^{AB} D_A D_B \log \omega) . \quad (3.9)$$

The elliptic equation (3.9) need only be solved at the initial time where, with initial data $J|_{\mathcal{S}^+} = 0$, $H^{AB} D_A D_B$ simplifies to the 2-Laplacian on the unit sphere. Then, as described in the next section, application of the Einstein equations on \mathcal{S}^+ determines the time dependence of ω according to

$$2\hat{n}^\alpha \partial_\alpha \log \omega = -e^{-2H} D_A L^A , \quad (3.10)$$

where $\hat{n}^\alpha = \hat{g}^{\alpha\beta} \nabla_\beta \ell$ is the null vector tangent to the generators of \mathcal{S}^+ . We use (3.10) to evolve ω along the generators of \mathcal{S}^+ given a solution of (3.9) as initial condition.

First recall some basic elements of Penrose compactification. In a general conformal frame with metric $\hat{g}_{\mu\nu} = \Omega^2 g_{\mu\nu}$, where $\Omega = 0$ on \mathcal{S}^+ , the vacuum Einstein equations $G_{\mu\nu} = 0$ take the form

$$\Omega^2 \hat{G}_{\mu\nu} + 2\Omega \hat{\nabla}_\mu \hat{\nabla}_\nu \Omega - \hat{g}_{\mu\nu} \left(2\Omega \hat{\nabla}^\rho \hat{\nabla}_\rho \Omega - 3(\hat{\nabla}^\rho \Omega \hat{\nabla}_\rho \Omega) \right) = 0 . \quad (3.11)$$

It immediately follows that

$$(\hat{\nabla}^\rho \Omega) \hat{\nabla}_\rho \Omega|_{\mathcal{S}^+} = 0 , \quad (3.12)$$

so that \mathcal{S}^+ is a null hypersurface and that

$$[\hat{\nabla}_\mu \hat{\nabla}_\nu \Omega - \frac{1}{4} \hat{g}_{\mu\nu} \hat{\nabla}^\rho \hat{\nabla}_\rho \Omega]|_{\mathcal{S}^+} = 0. \quad (3.13)$$

With respect to this frame, the construction of an inertial conformal frame proceeds as follows. We introduce a new conformal factor $\tilde{\Omega} = \omega \Omega$, with $\tilde{g}_{\mu\nu} = \omega^2 \hat{g}_{\mu\nu}$ by requiring, in accord with (3.10),

$$[2\hat{n}^\sigma \partial_\sigma \omega + \omega \hat{\nabla}_\sigma \hat{n}^\sigma]|_{\mathcal{S}^+} = 0, \quad \hat{n}^\sigma = \hat{g}^{\rho\sigma} \nabla_\rho \Omega. \quad (3.14)$$

As a result, it follows from a straightforward calculation that

$$\tilde{\nabla}^\rho \tilde{\nabla}_\rho \tilde{\Omega}|_{\mathcal{S}^+} = 0, \quad (3.15)$$

i.e., in the $\tilde{g}_{\mu\nu}$ conformal frame \mathcal{S}^+ is null, shear- and divergence-free.

It also follows that

$$\tilde{n}^\sigma \tilde{\nabla}_\sigma \tilde{n}^\nu|_{\mathcal{S}^+} = 0, \quad (3.16)$$

where $\tilde{n}^\sigma = \tilde{g}^{\rho\sigma} \tilde{\nabla}_\rho \tilde{\Omega}$, i.e., in the $\tilde{g}_{\mu\nu}$ frame, \tilde{n}^σ is an affinely parametrized null generator of \mathcal{S}^+ .

To construct inertial coordinates $(\tilde{u}, x^{\tilde{A}})$ on \mathcal{S}^+ , we first assign angular coordinates $x^{\tilde{A}}$ to each point of the initial spacelike spherical slice $u = u_0$ of \mathcal{S}^+ . We then propagate these coordinates along the generators of \mathcal{S}^+ according to

$$\tilde{n}^\rho \partial_\rho x^{\tilde{A}}|_{\mathcal{S}^+} = \omega^{-1} \hat{n}^\rho \partial_\rho x^{\tilde{A}}|_{\mathcal{S}^+} = 0. \quad (3.17)$$

In addition, we require

$$\tilde{n}^\rho \partial_\rho \tilde{u}|_{\mathcal{S}^+} = \omega^{-1} \hat{n}^\rho \partial_\rho \tilde{u}|_{\mathcal{S}^+} = 1, \quad (3.18)$$

so that \tilde{u} is an affine parameter along the generators in the $\tilde{g}_{\mu\nu}$ conformal frame.

4. News

The Bondi news function N is computed in the computational coordinates with the appropriate conformal transformation. It is then interpolated onto the inertial coordinates. The formalism follows that of [13], Appendix B (with a sign error in s_3 corrected):

$$N = \frac{1}{4\omega A} \left(s_1 + s_2 + \frac{1}{4} (\bar{\partial}\bar{U} + \bar{\partial}U) s_3 - 4\omega^{-2}s_4 + 2\omega^{-1}s_5 \right), \quad (4.1)$$

where $A = \omega e^{2\beta}$ and the s_i terms are

$$\begin{aligned}
s_1 &= (J^2 \bar{J}_{,\ell u} + J \bar{J} J_{,\ell u} - 2JKK_{,\ell u} - 2JK_{,\ell u} + 2J_{,\ell u}K + 2J_{,\ell u})/(K + 1) , \\
s_2 &= (\partial J_{,\ell} J \bar{J} \bar{U} + 2\partial J_{,\ell} K \bar{U} + 2\partial J_{,\ell} \bar{U} + \partial \bar{J}_{,\ell} J^2 \bar{U} \\
&\quad - 2\partial K_{,\ell} J K \bar{U} - 2\partial K_{,\ell} J \bar{U} + 2\partial U J \bar{J} K_{,\ell} - 2\partial U J \bar{J}_{,\ell} K \\
&\quad - 2\partial U J \bar{J}_{,\ell} + 4\partial U K K_{,\ell} + 4\partial U K_{,\ell} + 2\partial \bar{U} J \bar{J} J_{,\ell} - 2\partial \bar{U} J K K_{,\ell} \\
&\quad - 2\partial \bar{U} J K_{,\ell} + 4\partial \bar{U} J_{,\ell} K + 4\partial \bar{U} J_{,\ell} + \partial \bar{J}_{,\ell} J \bar{J} U + 2\partial \bar{J}_{,\ell} K U + 2\partial \bar{J}_{,\ell} U \\
&\quad + \partial \bar{J}_{,\ell} J^2 U - 2\partial K_{,\ell} J K U - 2\partial K_{,\ell} J U + 2\partial U J^2 \bar{J}_{,\ell} - 2\partial U J K K_{,\ell} \\
&\quad - 2\partial U J K_{,\ell} + 2\partial \bar{U} J^2 K_{,\ell} - 2\partial \bar{U} J J_{,\ell} K - 2\partial \bar{U} J J_{,\ell})/(2(K + 1)) , \\
s_3 &= -(J^2 \bar{J}_{,\ell} + J \bar{J} J_{,\ell} - 2JKK_{,\ell} - 2JK_{,\ell} + 2J_{,\ell}K + 2J_{,\ell})/(K + 1) , \\
s_4 &= (\partial A \bar{\partial} \omega J \bar{J} + 2\partial A \bar{\partial} \omega K + 2\partial A \bar{\partial} \omega - \partial A \bar{\partial} \omega J K \\
&\quad - \partial A \bar{\partial} \omega J - \partial \omega \bar{\partial} A J K - \partial \omega \bar{\partial} A J + \partial A \bar{\partial} \omega J^2)/(2(K + 1)) , \\
s_5 &= (2\bar{\partial}^2 A J \bar{J} + 4\bar{\partial}^2 A K + 4\bar{\partial}^2 A + 2\bar{\partial}^2 A J^2 - 4\bar{\partial} \bar{\partial} A J K \\
&\quad - 4\bar{\partial} \bar{\partial} A J + \partial A \bar{\partial} J J \bar{J}^2 + 2\partial A \bar{\partial} J \bar{J} K + 2\partial A \bar{\partial} J \bar{J} + \partial A \bar{\partial} \bar{J} J^2 \bar{J} \\
&\quad + 2\partial A \bar{\partial} \bar{J} J K + 2\partial A \bar{\partial} \bar{J} J - 2\partial A \bar{\partial} K J \bar{J} K - 4\partial A \bar{\partial} K J \bar{J} - 4\partial A \bar{\partial} K K \\
&\quad - 4\partial A \bar{\partial} K - \partial A \bar{\partial} J J \bar{J} K + 2\partial A \bar{\partial} J K + 2\partial A \bar{\partial} J - \partial A \bar{\partial} \bar{J} J^2 K \\
&\quad + 2\partial A \bar{\partial} K J^2 \bar{J} - \partial J \bar{\partial} A J \bar{J} K - 2\partial J \bar{\partial} A J \bar{J} - 2\partial J \bar{\partial} A K \\
&\quad - 2\partial J \bar{\partial} A - \partial \bar{J} \bar{\partial} A J^2 K - 2\partial \bar{J} \bar{\partial} A J^2 + 2\partial K \bar{\partial} A J^2 \bar{J} \\
&\quad + 4\partial K \bar{\partial} A J K + 4\partial K \bar{\partial} A J + \partial A \bar{\partial} J J^2 \bar{J} \\
&\quad + \partial A \bar{\partial} \bar{J} J^3 - 2\partial A \bar{\partial} K J^2 K)/(4(K + 1)) . \tag{4.2}
\end{aligned}$$

In our implementation, $_{,i}$ derivatives are derived from spectrally calculated $_{,\rho}$ derivatives using the appropriate Jacobian.

5. Results

In our comparison tests of CCE, the worldtube boundary data were extracted from a simulation of an equal mass non-spinning head-on black hole collision, with initial separation of $30M$. The control run (Isotropic) utilized the standard harmonic gauge damping identical to that in [23] throughout the head-on merger and ring-down. Harmonic gauge damping adds a dissipative forcing term to the wave equations satisfied by the harmonic Cartesian spatial coordinates (x, y, z) . In order to diminish the effects of a custom designed gauge, we also compare with results of another run (HytZero) which turns off gauge damping in the harmonic y -direction, transverse to the x -direction motion of the black holes. These two high-resolution runs were used as boundary data for all the subsequent CCE runs. These runs include 3 different resolutions, 2 different codes, 2 different gauges, and 3 different extraction radii, for a total of 36 runs.

As described in [15], the SpEC characteristic evolution algorithm exploits spectral methods and innovative integral methods that greatly improve upon the speed and accuracy of the Pitt null code. This is seen as essential for taking advantage of the efficiency of SpEC Cauchy evolution. The necessary improvement in efficiency has been preserved in the SpEC extraction module, as displayed in Table 1. The comparison runs were performed using the current version of the Pitt code [20], which forms part of the Einstein Toolkit.

The initial conditions and extraction parameters were deliberately chosen as a stressful test of the algorithms. In particular, at the beginning of the run the black hole excision boundary extends out to Cartesian radius $R = 16M$, which is very close to our smallest choice of extraction radius at $R = 30M$. At this radius, gauge effects are highly significant and would make perturbative extraction schemes meaningless,

in accordance with our intentions. One consequence of such an extreme choice is that differences between the Pitt and SpEC inertial frame and worldtube initialization procedures lead to noticeably different waveforms. Worldtube initialization involves supplying the “integration constants” from the Cauchy code, which allows radial integration of the characteristic hypersurface and evolution equations (2.3) – (2.7) from the worldtube to \mathcal{I}^+ . In both Pitt null code and SpEC, the initial condition on J is determined by the inner boundary value, supplied by the Cauchy evolution, with a smooth roll off to zero at \mathcal{I}^+ .

The extraction worldtube Γ is determined by a surface of constant Cartesian radius R . In the Pitt CCE code, the areal radius r_{wt} of Γ lies between two surfaces of constant Cartesian radii $R_1 \leq r_{wt} \leq R_2$ and this carries over to the compactified radial coordinate. As a result, interpolation is necessary to supply the integration constants, which introduces numerical error. In the SpEC CCE code, this interpolation error is avoided by introducing the compactified radial coordinate (2.9), with range $1/2 \leq \rho \leq 1$ between Γ and \mathcal{I}^+ .

Worldtube data from each run were extracted using both Pitt and SpEC CCE, at three different Cartesian radii: $R = 30M$, $R = 100M$ and $R = 250M$, as illustrated by the news function waveforms in Figs. 2, 4, and 6, respectively. In these figures, the HytZero and Isotropic waveforms are so close that they appear on top of one another. The major discrepancy between the Pitt and SpEC waveforms is due to the worldtube interpolation error in the Pitt code. This is especially evident at small extraction radii, where there is strong “junk” radiation near the worldtube, which is inherent in the initial Cauchy data and its mismatch with the initial characteristic data.

This interpolation error in the Pitt code converges away at larger radii, where the field gradients between R_1 and R_2 become smaller. This is seen in Figs. 3, 5, and

| Run | Pitt1 | Pitt2 | Pitt3 | SpEC1 | SpEC2 | SpEC3 |
|---------------|-------|-----------|-------|-------|----------|-------|
| N_r | 100 | 150 | 200 | 10 | 12 | 14 |
| N or L | 40 | 60 | 80 | 12 | 14 | 17 |
| $\Delta t/M$ | 0.1 | 0.0666... | 0.05 | 1.0 | 0.666... | 0.5 |
| T (CPU hours) | 173 | 274 | 374 | 0.7 | 1.9 | 3.1 |

Table 1: Resolution parameters used for code convergence comparisons, with time steps Δt . N_r represents the radial grid sizes. The Pitt null code uses two stereographic patches with $2N^2$ total number of angular grid points. The SpEC code has $2L^2$ total angular grid points. T is the CPU time taken for $R = 30M$, $t_{final} = 450M$ runs in the Isotropic gauge, and is representative for the other runs. All resolutions and codes were run from the same initial data.

7, where the relative difference between the Pitt and SpEC news function waveforms is compared with the relative numerical error implied by convergence tests.

Each run was computed at 3 different resolutions to monitor convergence, as indicated in Table 1. In the following subsections, we first show convergence and the removal of gauge effects, separately for the Pitt and SpEC codes. Next, we compare Ψ_4^0 waveforms and establish further agreement between the two codes. Finally, we examine the evolution of the inertial coordinates at \mathcal{I}^+ relative to the worldtube coordinates induced by the Cauchy evolution.

Comparison of the relative error E_{rel} between dataset A and dataset B is computed according to

$$E_{rel} = \log_{10} \left(\frac{|A - B|}{|B|} \right), \quad (5.1)$$

where in convergence tests B is the highest resolution dataset, and the real parts of the $(\ell, m) = (2, 2)$ spherical harmonic modes are compared.

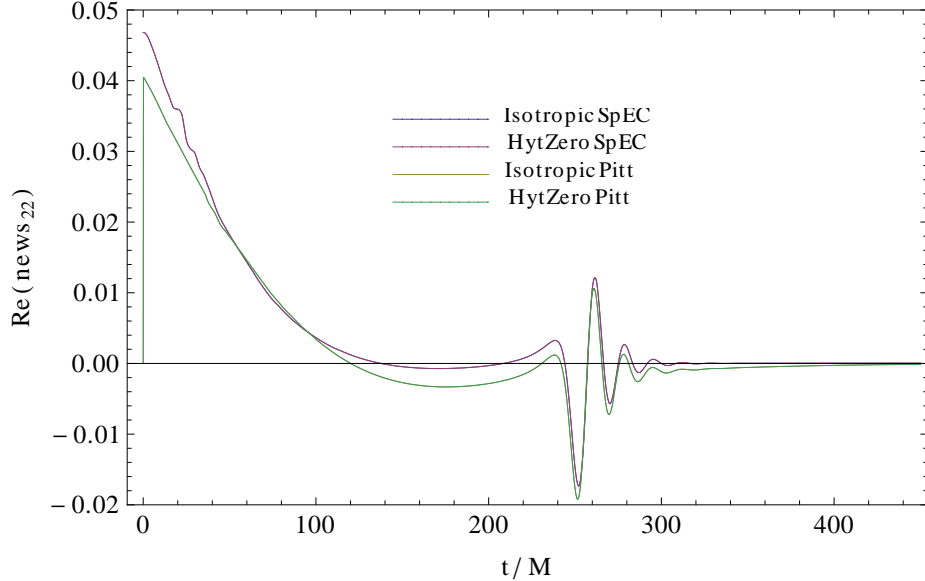


Figure 2: Waveforms of the real part of the $(2,2)$ spherical harmonic mode of the news function, as computed by the Pitt null code and SpEC with extraction worldtube at $R = 30M$. Different initialization procedures at the worldtube give rise to a difference between the Pitt and SpEC waveforms, which is most pronounced at this small extraction radius. The different gauge choices, Isotropic and HytZero, do not have noticeable effect on this scale, indicating successful gauge effect removal in both codes.

5.1. Pitt code convergence and removal of gauge effects

Here, in order to establish a baseline, we examine the self convergence of the Pitt code for each of the extraction radii, using the three resolutions (Pitt1,Pitt2,Pitt3) indicated in Table 1. In Figs. 8, 9, and 10, we see in both the Isotropic and HytZero gauges that the news function converges over the entire run. Indeed, Isotropic (solid lines) and HytZero (dashed lines) overlap completely. The figures also plot the relative error in the news computed in both gauges, which is consistently below the numerical error implied by convergence tests for extraction worldtubes at $R = 30M$ and $R = 100M$. This verifies that the Pitt code successfully removes gauge effects. Furthermore, the figures plot the relative error between the news computed in the

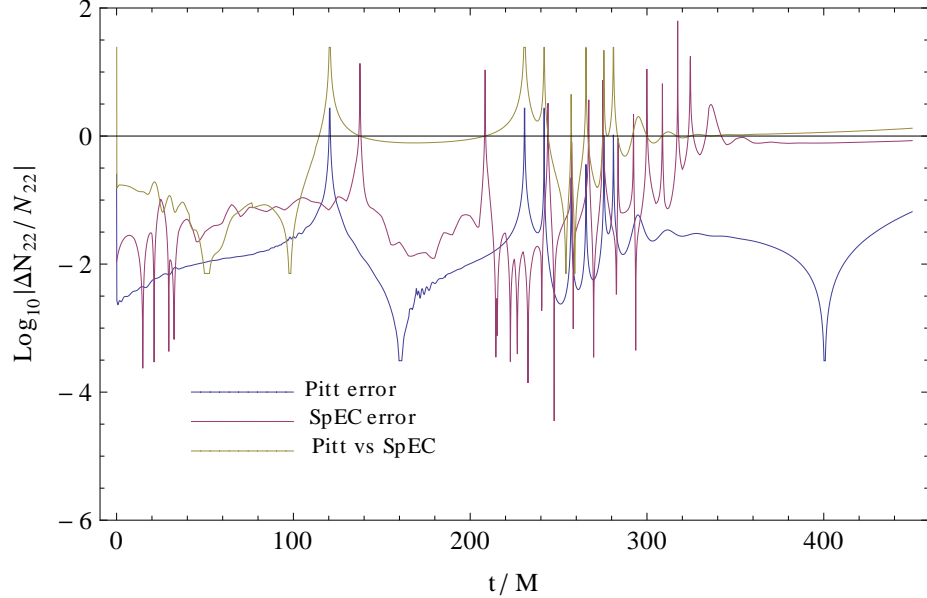


Figure 3: Graphs showing the relative difference between the real part of the $(2, 2)$ mode Pitt and SpEC news function waveforms for extraction radius $R = 30M$, in comparison to the relative numerical error implied by convergence tests, corresponding to the waveforms in Fig. 2. While both SpEC and Pitt have comparable and consistent levels of error, the codes do not agree within that level of error at this extraction radius.

worldtube coordinates and the inertial coordinates at \mathcal{I}^+ . In the $R = 30M$ case shown in Fig. 8, the initial discrepancy is high due to the strong gauge effects of junk radiation. It does not fall below the relative error between the Isotropic and HytZero gauges until well after the signal has passed. This confirms that the transformation to inertial coordinates is essential for correctly removing gauge effects from the waveform. For extraction at $R = 100M$ shown in Fig. 9, the relative error between worldtube and inertial coordinates has dropped below the Isotropic-HytZero gauge effect. At $R = 250M$ shown in Fig. 10, the predominant error is the Isotropic-HytZero gauge effect.

These results show that the selected runs do produce a substantial gauge error between the worldtube and inertial coordinates and that the Pitt code effectively

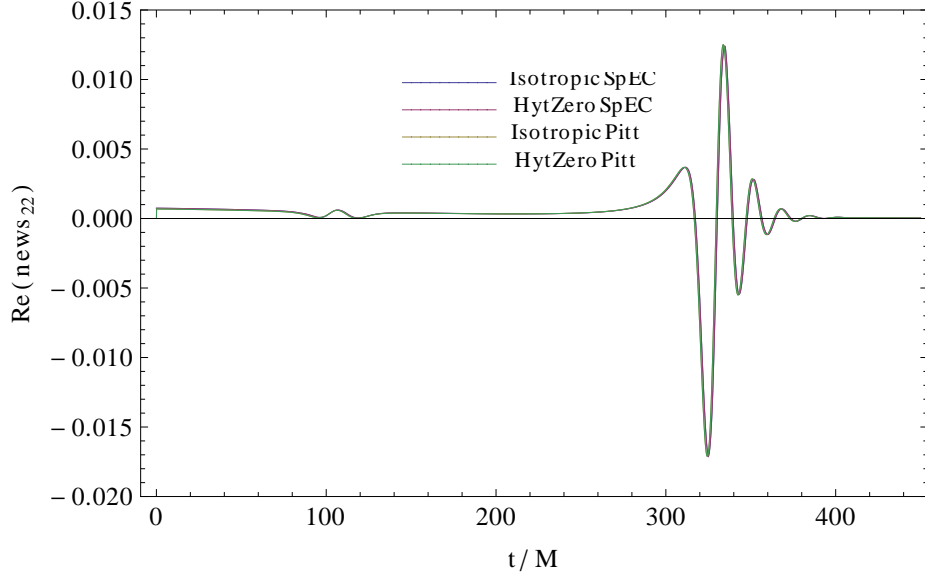


Figure 4: Waveforms of the real part of the $(2, 2)$ mode of the news function, as computed by the Pitt and SpEC codes with extraction worldtube at $R = 100M$. Compared to Fig. 2, at this larger extraction radius the worldtube initialization differences lead to a much smaller difference between waveforms, which appear nearly identical here. The main discrepancy arises from the treatment of the junk radiation at early times. Here, too, gauge differences between HytZero and Isotropic are not visible at this scale.

removes it, while remaining convergent for the duration of the run.

5.2. SpEC code convergence and removal of gauge effects

Here we examine the SpEC code's self convergence for each extraction radii, in the same way that the Pitt code was examined in Sec. 5.1. In Figs. 11, 12, and 13, we see that convergence, measured with the resolutions indicated in Table 1, is comparable to the Pitt code's convergence, while the potential gauge contamination is consistently removed at all worldtube radii. As in Figs. 8, 9, and 10, the solid lines (Isotropic) and dashed lines (HytZero) overlap due to consistency in gauge removal. The SpEC extraction code effectively removes gauge error at all radii while remaining convergent

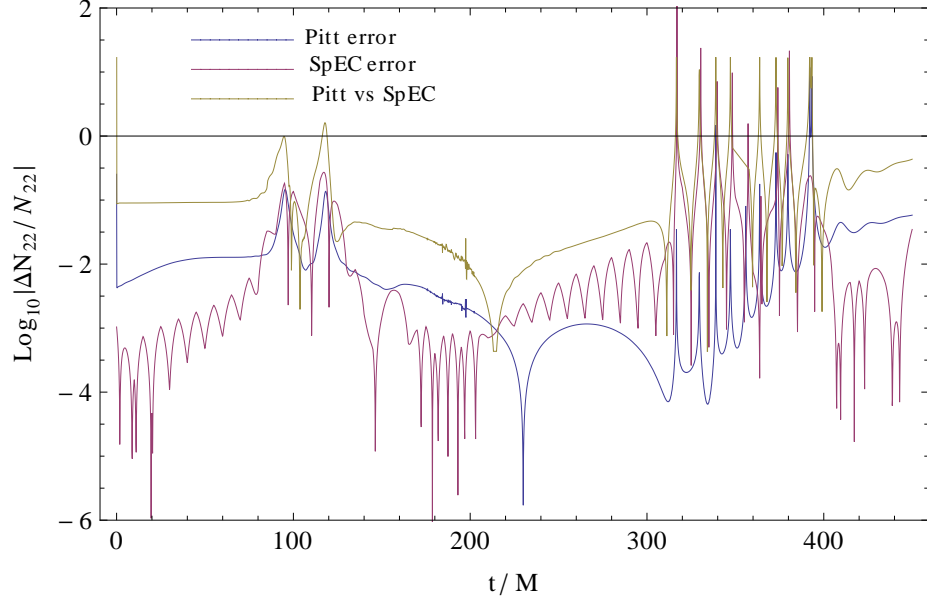


Figure 5: Graph showing the relative difference between the real part of the $(2,2)$ mode SpEC and Pitt news waveforms for extraction radius $R = 100M$, and the relative numerical error, corresponding to the waveforms in Fig. 4. In comparison with Fig. 3, by $R = 100M$ the difference between the Pitt and SpEC algorithms has dropped to the level of numerical error in each algorithm.

throughout the runs.

5.3. Comparison of Ψ_4^0 between the Pitt and SpEC codes

In Secs 5.1 and 5.2, we have shown that both codes are convergent and remove potential gauge effects. We have also demonstrated that the difference in the news computed by the two codes disappears as the extraction worldtube radius increases. Here we provide further evidence that even at a small worldtube radius the waveform computed by the SpEC code is valid.

After the gauge freedom is removed by extraction, there is still supertranslation and Lorentz freedom in the choice of inertial coordinates, which affect the phase and velocity of the inertial observers. This effect is highly sensitive to initial conditions

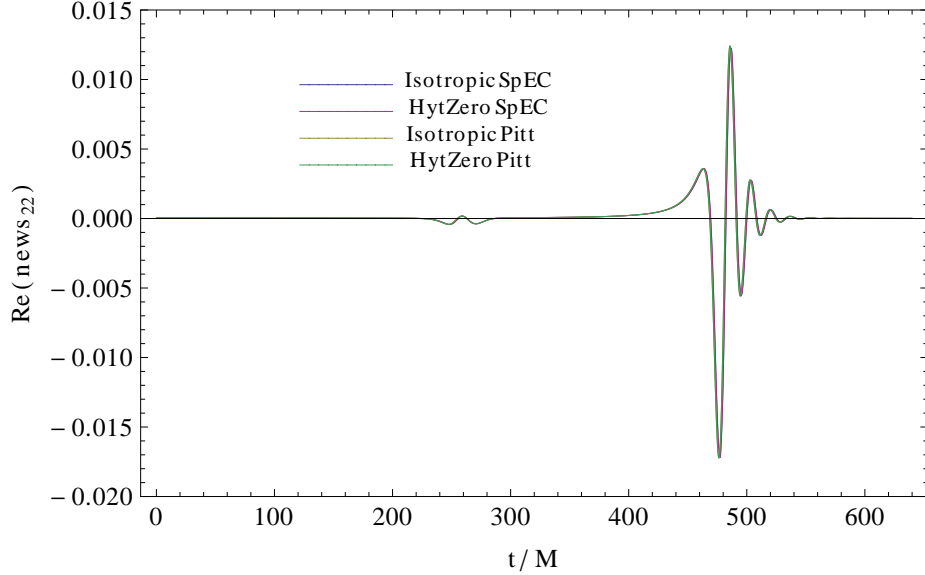


Figure 6: Waveforms of the real part of the $(2, 2)$ mode of the news function, as computed by the Pitt and **SpEC** codes with extraction worldtube at $R = 250M$. At this large extraction radius there is a barely noticeable difference between all the waveforms, limited to the junk radiation at early times.

and also to the evolution of the inertial conformal transformation factor ω , especially in the extreme gauge conditions of extraction at $R = 30M$. It feeds into the worldtube interpolation error in the Pitt code. In order to verify that the discrepancy illustrated in Fig. 2 between the news computed by the Pitt null code and **SpEC** is partially due to this inertial coordinate freedom, we compute the time derivative of the news, which is related to the Weyl curvature in inertial coordinates according to $\partial_t N = \Psi_4^0$. This suppresses phase differences between the two waveforms. In making the comparisons, Ψ_4^0 is computed semi-independently using the Weyl tensor waveform module in the current version of the Pitt code [20]. In these runs, Ψ_4^0 was found to be convergent with truncation error comparable to the consistency between Ψ_4^0 and $\partial_t N$ in the Pitt code.

In Fig. 14, we see that the time derivative of the news and Ψ_4^0 have much less

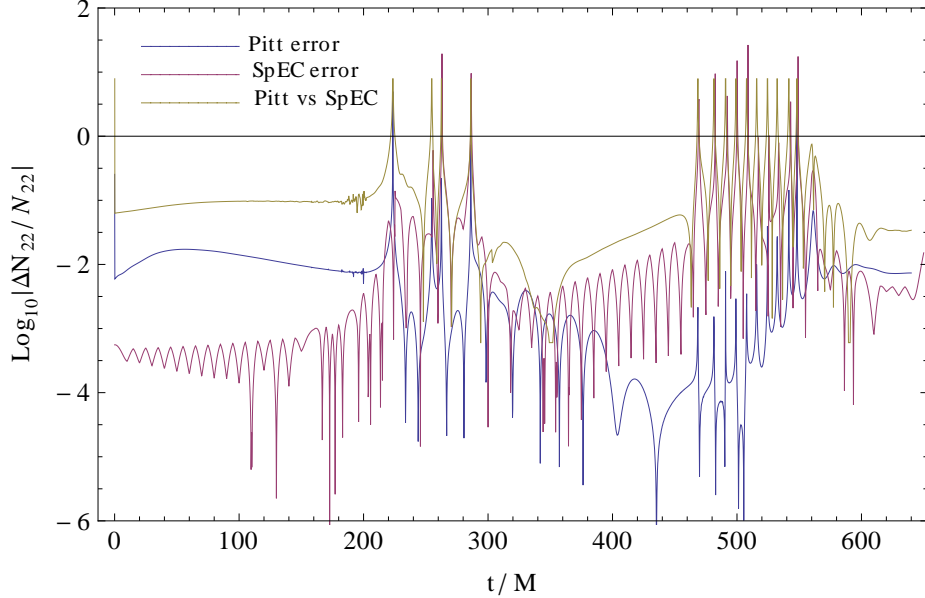


Figure 7: Graphs showing the relative difference between SpEC and Pitt news waveforms at $R = 250M$, in comparison to the relative numerical error, corresponding to the waveforms in Fig. 6. During the post-junk part of the waveform, the error due to worldtube initialization has dropped to the level of the numerical error, completing the trend seen in Fig. 5.

discrepancy than Fig. 2 would suggest. In Figs. 15, 17, and 19, we compare relative errors between Ψ_4^0 and $\partial_t N$ computed by the Pitt and SpEC codes. Not only is there agreement between the codes at $R = 30M$, this agreement persists for larger extraction radii, as shown in Figs. 16 and 18. Both codes show agreement with the Ψ_4^0 waveform throughout the runs at all three extraction radii. This indicates that a major part of the discrepancy in Fig. 2 is due to initialization errors in the Pitt code, confirming the physical validity of the extracted SpEC waveform.

5.4. Relative motion between inertial and worldtube coordinates

In Section 3, we discussed the construction of an inertial coordinate system and its evolution with respect to the worldtube coordinates constructed from the Cartesian coordinates of the Cauchy code. Here, we describe the motion of the inertial (θ, ϕ)

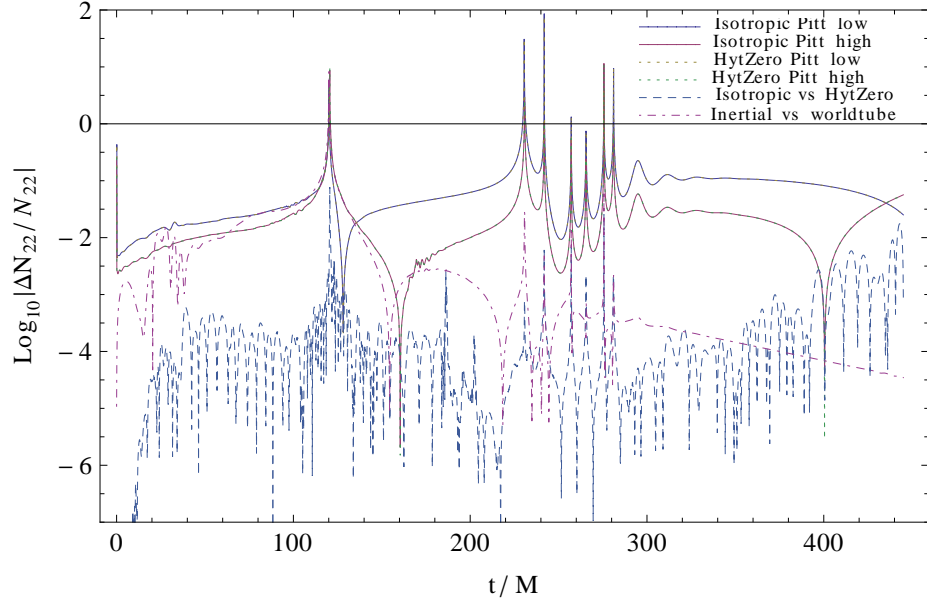


Figure 8: Graphs of the relative error $\log_{10} |\Delta N_{22}/N_{22}|$ in the (2,2) mode of the news function for the $R = 30M$ Pitt extraction run in both gauges. The relative errors for the Pitt1 (low) and Pitt2 (high) resolutions (compared to Pitt2 and Pitt3 respectively) are rescaled to demonstrate convergence. The dashed blue line indicates the relative error (Isotropic vs HytZero) between the news computed in both gauges. The dot-dashed purple line (Inertial vs worldtube) indicates the relative error between the news computed in the worldtube coordinates and the inertial coordinates. At this small extraction radius, this discrepancy is high due to the strong gauge effect of junk radiation.

angular coordinates relative to the worldtube angular coordinates, constructed in the standard way from the worldtube Cartesian coordinates. Figure 20 illustrates the global pattern of this relative motion for the Isotropic gauge SpEC run with the highest resolution extraction at $R = 30M$. Generally speaking, the coordinates wiggle back and forth in the direction corresponding to the motion of the black holes. The complete movement amounts to at most a few percent of their initial values, but even this is sufficient to introduce considerable gauge error in the waveform, as already seen in Fig. 8.

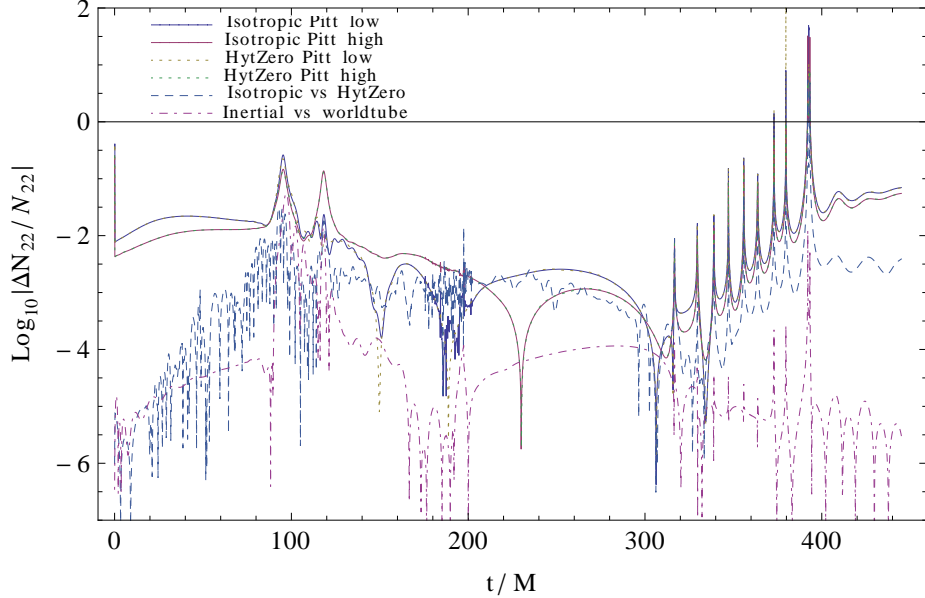


Figure 9: Graphs of the relative error $\log_{10} |\Delta N_{22}/N_{22}|$ in the news function for Pitt extraction at $R = 100M$. Again, the errors for the Pitt1 and Pitt2 resolutions demonstrate convergence. Compared to Fig. 8, the relative error (Inertial vs worldtube) between inertial and worldtube coordinates has now dropped below the Isotropic vs HytZero gauge effect.

In Fig. 21, the relative ϕ motion of the point circled in Fig. 20 is plotted as a function of inertial time. Initial junk radiation causes considerable wobble, followed by a smooth return almost to its starting point. The maximum excursion of the ϕ -coordinate shift from its initial value is about 3.5%.

5.5. Precessing, spinning binary black hole merger

In addition to the head-on collision tests which we have described, we have also investigated stability and convergence of the Pitt and SpEC CCE modules, together with the inertial-worldtube coordinate transformation, using the generic test run of precessing, spinning binary black holes in [15], as taken from Taylor *et al.*[24]. Its parameters are mass ratio $q = 3$, black hole spins $\chi_1 = (0.7, 0, 0.7)/\sqrt{2}$ and $\chi_2 = (-0.3, 0, 0.3)/\sqrt{2}$, number of orbits 26, total time $T = 7509M$, initial eccentricity

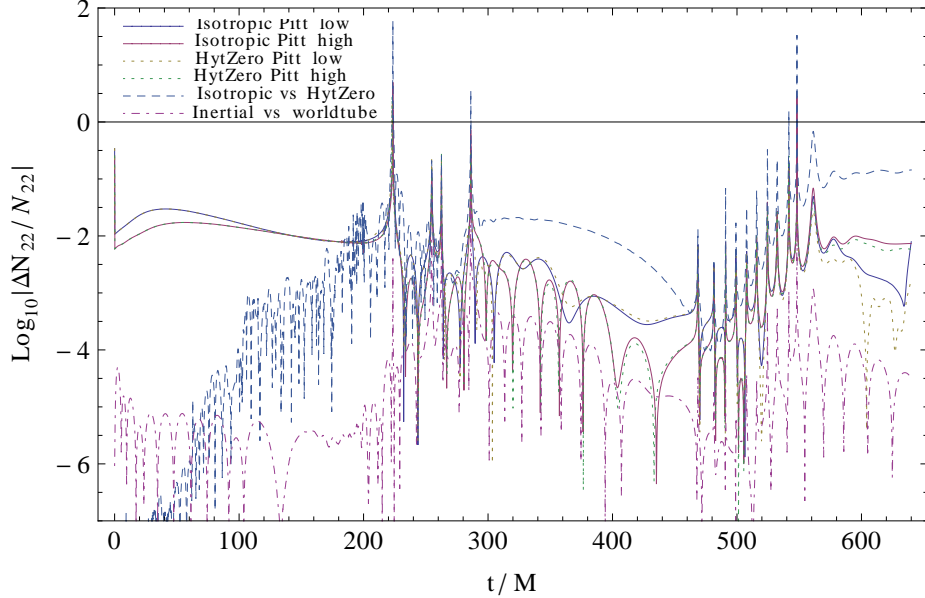


Figure 10: Graphs of the relative error $\log_{10} |\Delta N_{22}/N_{22}|$ in the news function for Pitt extraction at $R = 250M$. At this large extraction radius, the dominant error arises from the Isotropic-HytZero gauge effect.

10^{-3} , initial frequency $\omega_{ini} = 0.032/M$, and extraction radius $R = 100M$. The Pitt and SpEC waveforms displayed in Fig. 22 are fairly typical waveforms, spanning the initial junk radiation through inspiral, merger, and ringdown.

Figures 23 and 24 show a log scale comparison of the waveforms with absolute error. The codes agree strongly throughout the run.

The relative inertial-worldtube coordinate motion of a representative point in the extended generic run is illustrated in Fig. 25. At early times, the helix has two loops per cycle corresponding to each of the black holes. At later times, precession dominates the evolution of this particular coordinate. Throughout the run, the deviation is around 0.5%.

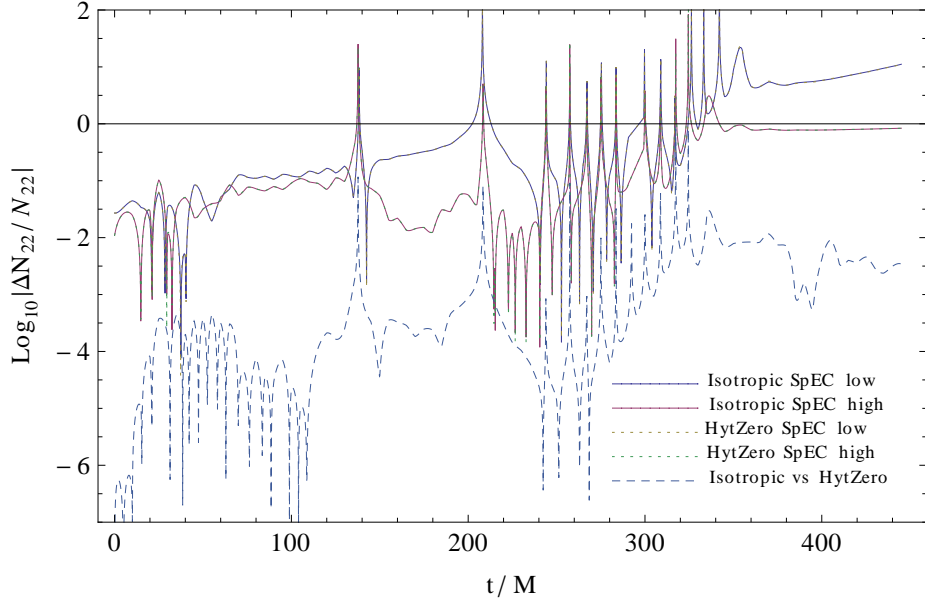


Figure 11: Graphs of the relative error $\log_{10} |\Delta N_{22}/N_{22}|$ in the news function for the $R = 30M$ SpEC extraction run in both gauges. The relative errors for the SpEC1 (low) and SpEC2 (high) resolutions (compared to SpEC2 and SpEC3 respectively) are rescaled to demonstrate convergence. The graph Isotropic vs HytZero indicates the relative error between the news computed in both gauges. Even at this small extraction radius, there is relatively little Isotropic vs HytZero gauge error.

6. Conclusion

The SpEC characteristic evolution algorithm has now been furnished with a convergent, efficient news extraction module. SpEC is now capable of rapidly producing accurate, gauge free waveforms as required.

Acknowledgments

We thank Nicholas Taylor for his generic spinning binary black hole run that we used to test and baseline code performance. We thank Yosef Zlochower for supplying details of the news module in the Pitt null code. We thank Mark Scheel, Yanbei

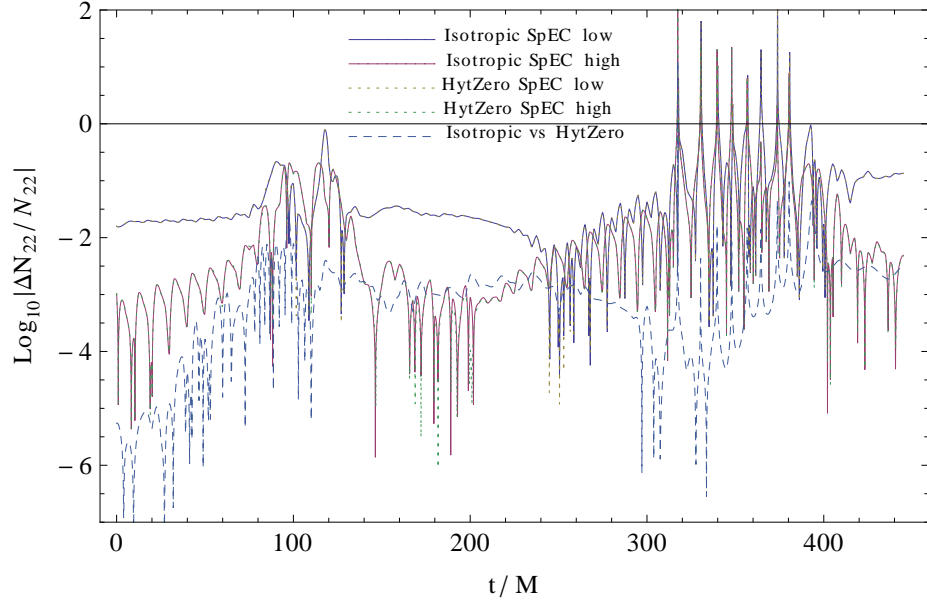


Figure 12: Graphs of the relative error $\log_{10} |\Delta N_{22}/N_{22}|$ in the news function for the $R = 100M$ SpEC extraction run in both gauges. The graphs show convergence in both gauges. The Isotropic vs HytZero gauge error is relatively small.

Chen, and Christian Reisswig for their advice, support, and technical expertise, and thank Michael Boyle for comments on the manuscript. This research used the Spectral Einstein Code (SpEC)[25]. The Caltech cluster `zwicky.cacr.caltech.edu` is an essential resource for SpEC related research, supported by the Sherman Fairchild Foundation and by NSF award PHY-0960291. This research also used the Extreme Science and Engineering Discovery Environment (XSEDE) under grant TG-PHY990002. The UCSD cluster `ccom-boom.ucsd.edu` was used during code development. This project was supported by the Sherman Fairchild Foundation, and by NSF Grants PHY-1068881, AST-1333520, and CAREER Grant PHY-0956189 at Caltech. JW’s research was supported by NSF grant PHY-1201276 to the University of Pittsburgh.

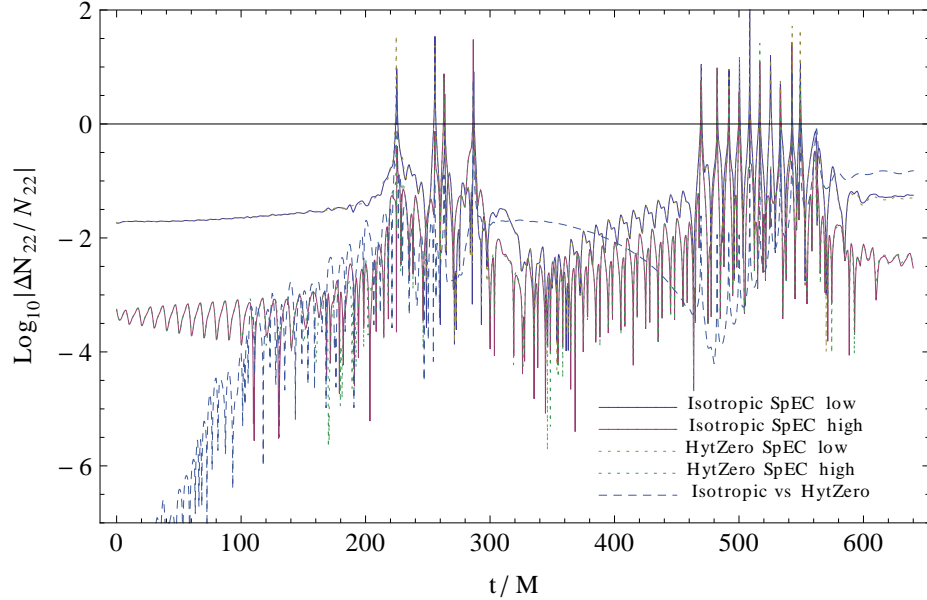


Figure 13: Graphs of the relative error $\log_{10} |\Delta N_{22}/N_{22}|$ in the news function for the $R = 250M$ SpEC extraction run in both gauges, showing convergence in both gauges as well as small gauge error throughout the run.

References

- [1] S. J. Waldman, “The advanced ligo gravitational wave detector,” Tech. Rep. LIGO-P0900115-v2, LIGO Project, 2011.
- [2] T. Accadia, F. Acernese, F. Antonucci, P. Astone, G. Ballardin, et al., “Plans for the upgrade of the gravitational wave detector VIRGO: Advanced VIRGO,” in Proceedings of the Twelfth Marcel Grossmann Meeting on General Relativity, T. Damour, R. T. Jantzen, and R. Ruffini, eds., pp. 1738–1742. 2009.
- [3] **LIGO Scientific Collaboration** Collaboration, H. Grote, “The GEO 600 status,” Class. Quantum Grav. **27** (2010) 084003.
- [4] K. Somiya and the KAGRA Collaboration, “Detector configuration of KAGRA—the japanese cryogenic gravitational-wave detector,” Class. Quantum Grav. **29** no. 12, (2012) 124007.
- [5] H. Bondi, M. G. J. van der Burg, and A. W. K. Metzner, “Gravitational waves in general relativity VII. Waves from axi-symmetric isolated systems,” Proc. R. Soc. Lond. A **269** (1962) 21–52.
- [6] R. K. Sachs, “Gravitational waves in general relativity. VIII. waves in asymptotically flat

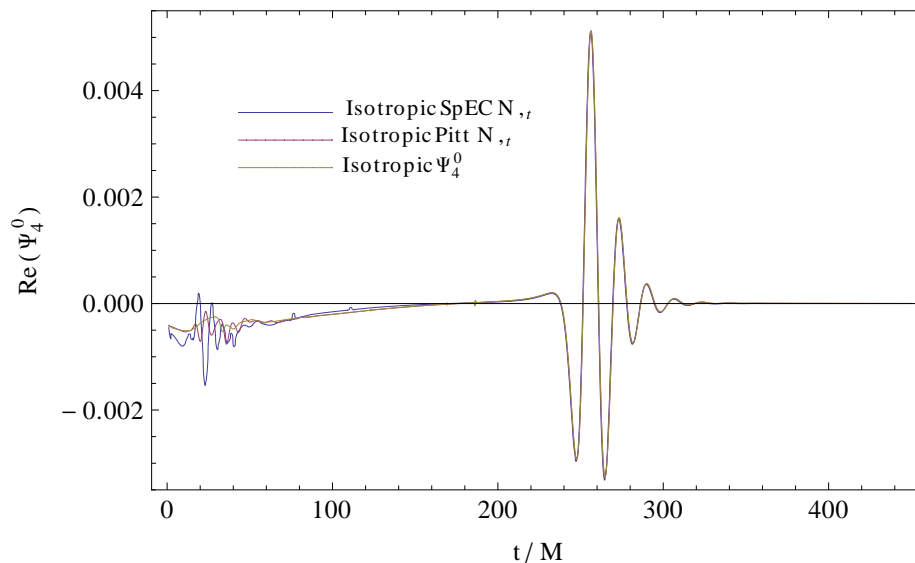


Figure 14: The real part of the $(2, 2)$ modes of the waveforms of Ψ_4^0 (computed during the Pitt run) and the time derivative of the news $\partial_t N$, as computed for the SpEC and Pitt runs using the Isotropic gauge with extraction radius $R = 30M$. The waveforms are in much better agreement than the comparison of the news waveforms for this extraction radius in Fig. 2.

space-time,” Proc. R. Soc. Lond. A **270** no. 1340, (October, 1962) 103–126.

<http://www.jstor.org/stable/2416200>.

- [7] R. Penrose, “Asymptotic properties of fields and space-times,” Phys. Rev. Lett. **10** no. 2, (1963) 66–68.
- [8] J. M. Bardeen, O. Sarbach, and L. T. Buchman, “Tetrad formalism for numerical relativity on conformally compactified constant mean curvature hypersurfaces,” Phys. Rev. D **83** (2011) 104045.
- [9] A. Zenginoğlu, “Hyperboloidal evolution with the Einstein equations,” Class. Quantum Grav. **25** (2008) 195025, [arXiv:gr-qc/0808.0810](https://arxiv.org/abs/gr-qc/0808.0810).
- [10] V. Moncrief and O. Rinne, “Regularity of the Einstein equations at future null infinity,” Class. Quantum Grav. **26** (2009) 125010, <http://www.arxiv.org/abs/gr-qc/0811.4109>.
- [11] L. A. Tamburino and J. H. Winicour, “Gravitational fields in finite and conformal Bondi frames,” Phys. Rev. **150** (1966) 1039–1053.
<http://link.aps.org/doi/10.1103/PhysRev.150.1039>.

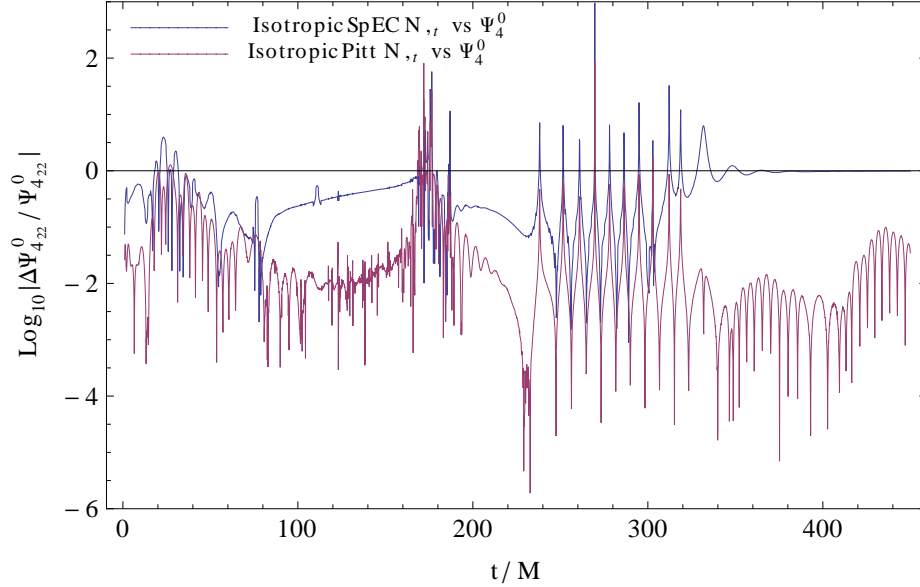


Figure 15: The relative error $\log_{10} |\Delta\Psi_{422}^0 / \Psi_{422}^0|$ between Ψ_4^0 and $\partial_t N$ as computed for the SpEC and Pitt runs using the Isotropic gauge with extraction radius $R = 30M$, corresponding to the waveforms in Fig. 14. Ψ_4^0 and its numerical truncation error were computed using the Pitt code. Truncation error in Ψ_4^0 was consistent with the $\partial_t N$ error shown here. The good agreement between the SpEC and Pitt results eventually lapses, but not until well after ring-down.

- [12] R. A. Isaacson, J. S. Welling, and J. Winicour, “Null cone computation of gravitational radiation,” *J. Math. Phys.* **24** no. 1824, (1983) .
<http://iopscience.iop.org/0264-9381/30/7/075017>.
- [13] N. T. Bishop, R. Gomez, L. Lehner, M. Maharaj, and J. Winicour, “High-powered gravitational news,” *Phys. Rev.* **D56** (1997) 6298–6309, [arXiv:gr-qc/9708065](https://arxiv.org/abs/gr-qc/9708065).
- [14] C. Reisswig, N. T. Bishop, and D. Pollney, “General relativistic null-cone evolutions with a high-order scheme,” *Gen. Rel. Grav.* **45** (5) (2013) 1069–1094, [arXiv:1208.3891](https://arxiv.org/abs/1208.3891) [gr-qc].
- [15] C. J. Handmer and B. Szilágyi, “Spectral characteristic evolution: A new algorithm for gravitational wave propagation,” *Classical and Quantum Gravity* **32** (2015) 025008, [arXiv:1406.7029](https://arxiv.org/abs/1406.7029).
- [16] R. Gómez, L. Lehner, P. Papadopoulos, and J. Winicour, “The eth formalism in numerical relativity,” *Class. Quantum Grav.* (01, 1997) , [arXiv:gr-qc/9702002](https://arxiv.org/abs/gr-qc/9702002).

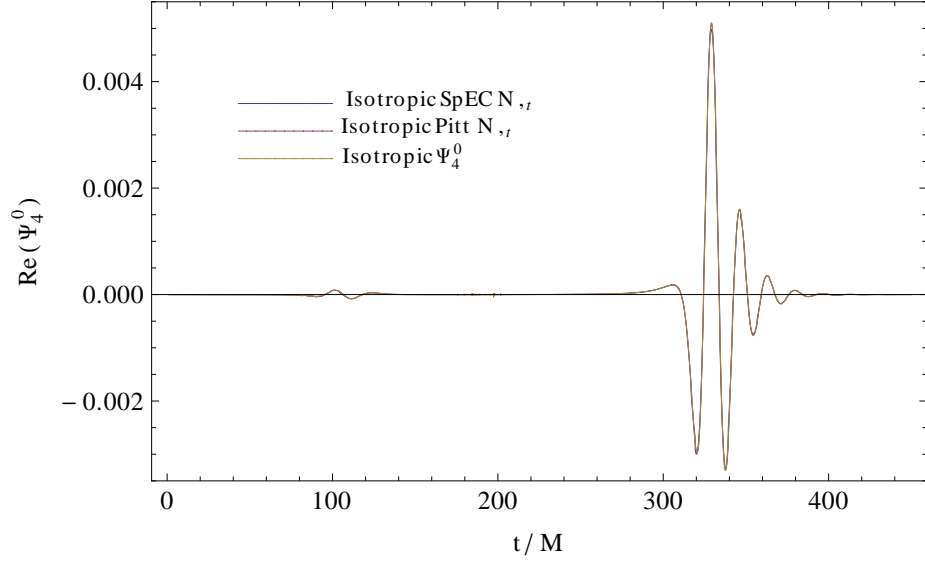


Figure 16: Waveforms of Ψ_4^0 and $\partial_t N$ as computed for the SpEC and Pitt runs using the Isotropic gauge with extraction radius $R = 100M$.

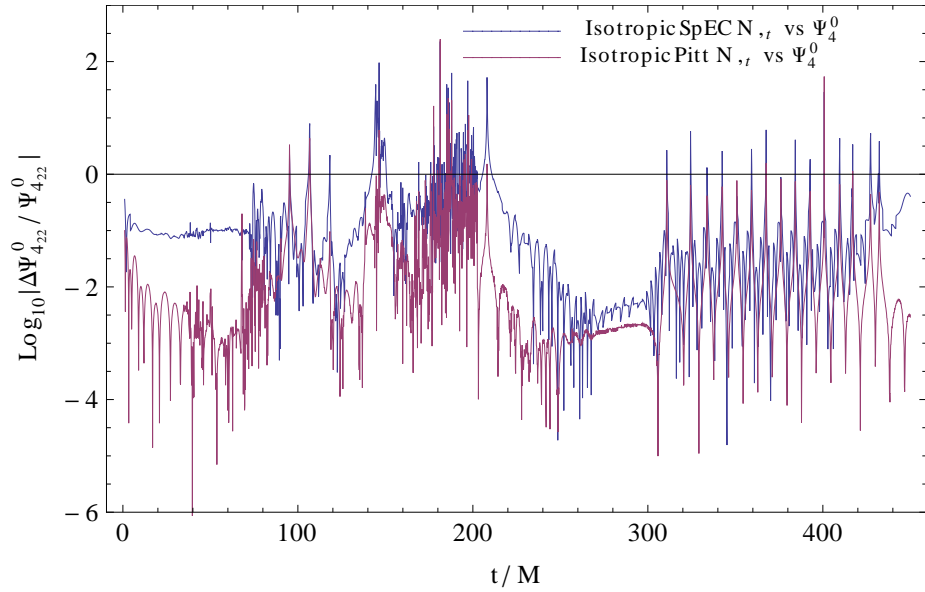


Figure 17: The relative error $\log_{10} |\Delta\Psi_{422}^0 / \Psi_{422}^0|$ between Ψ_4^0 and $\partial_t N$ as computed for the SpEC and Pitt runs using the Isotropic gauge with extraction radius $R = 100M$, corresponding to the waveforms in Fig. 16. Both codes show comparable agreement throughout the run.

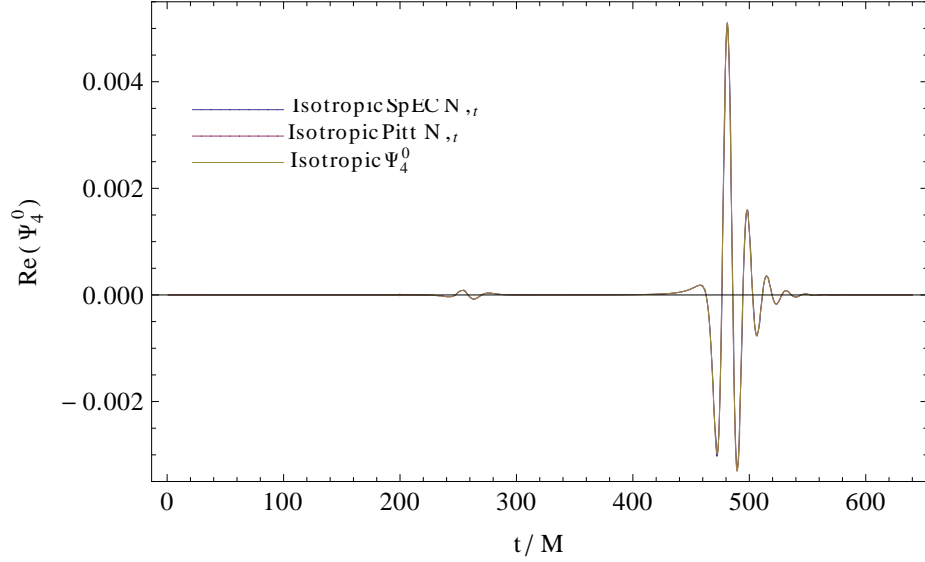


Figure 18: Waveforms of Ψ_4^0 and $\partial_t N$ as computed for the SpEC and Pitt codes using the Isotropic gauge with extraction radius $R = 250M$.

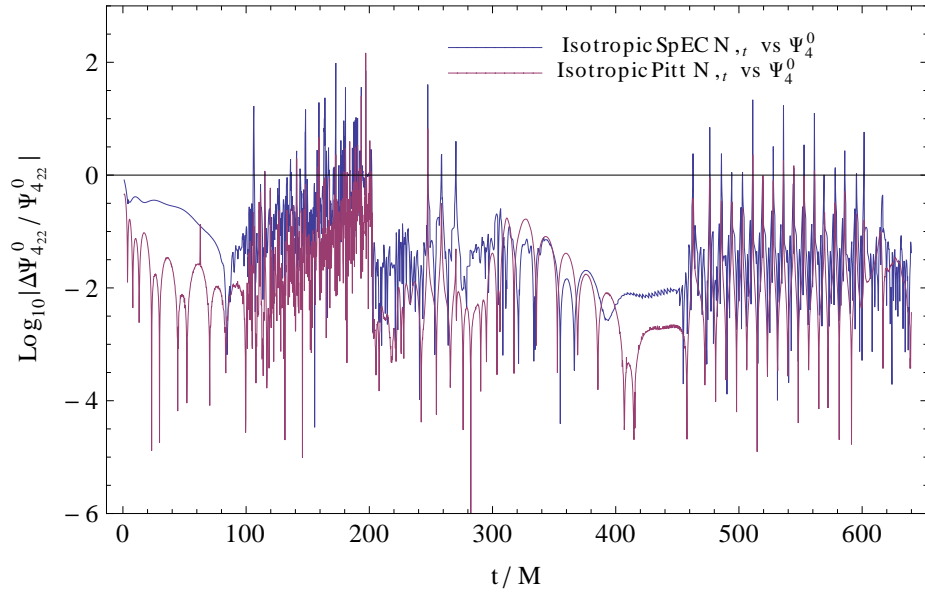


Figure 19: The relative error $\log_{10} |\Delta\Psi_{422}^0 / \Psi_{422}^0|$ between Ψ_4^0 and $\partial_t N$ computed for the SpEC and Pitt runs using the Isotropic gauge with extraction radius $R = 250M$, corresponding to the waveforms in Fig. 18. Both codes show good agreement throughout the run.

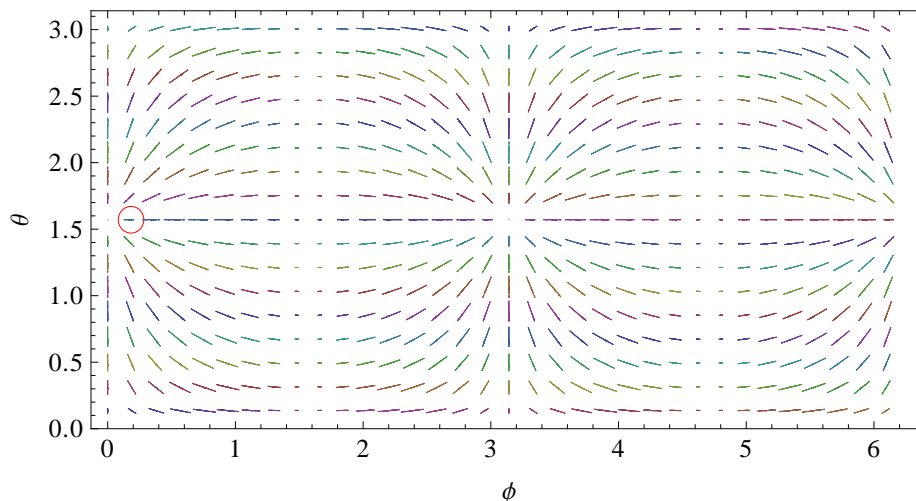


Figure 20: The arrows indicate the global pattern of the motion of the (θ, ϕ) inertial coordinates at each spherical collocation point (labeled in radians) relative to the worldtube angular coordinates. Global motion is primarily in the Cartesian x direction, and has been exaggerated by a factor of 10 for visibility.

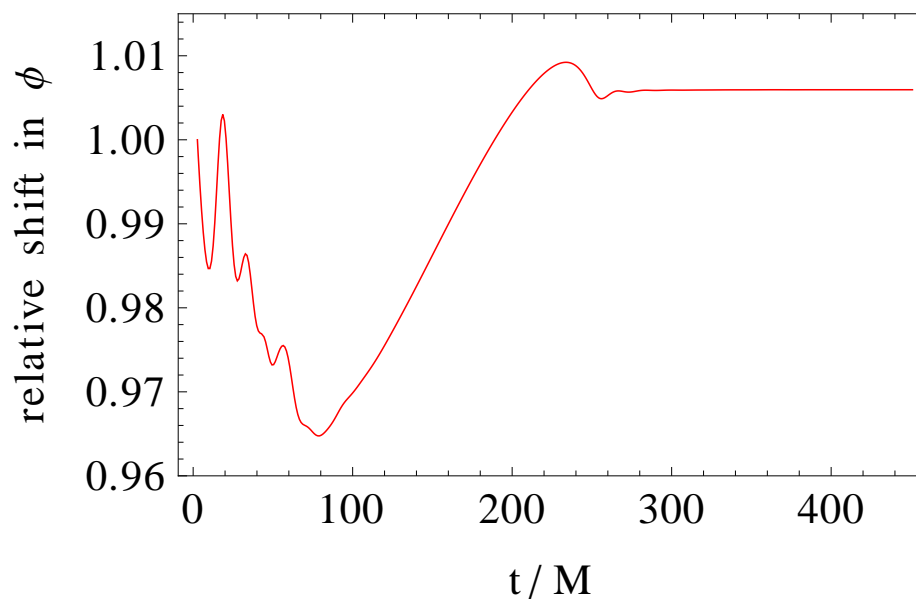


Figure 21: The relative inertial-worldtube ϕ -coordinate motion of the point circled in Fig. 20 shows approximately a 3.5 percent variation from its initial value.

[17] J. Winicour, “Newtonian gravity on the null cone,” *J. Math. Phys.* **1193** (1983) .

[18] N. T. Bishop, R. Gómez, R. A. Isaacson, L. Lehner, B. Szilágyi, and J. Winicour,

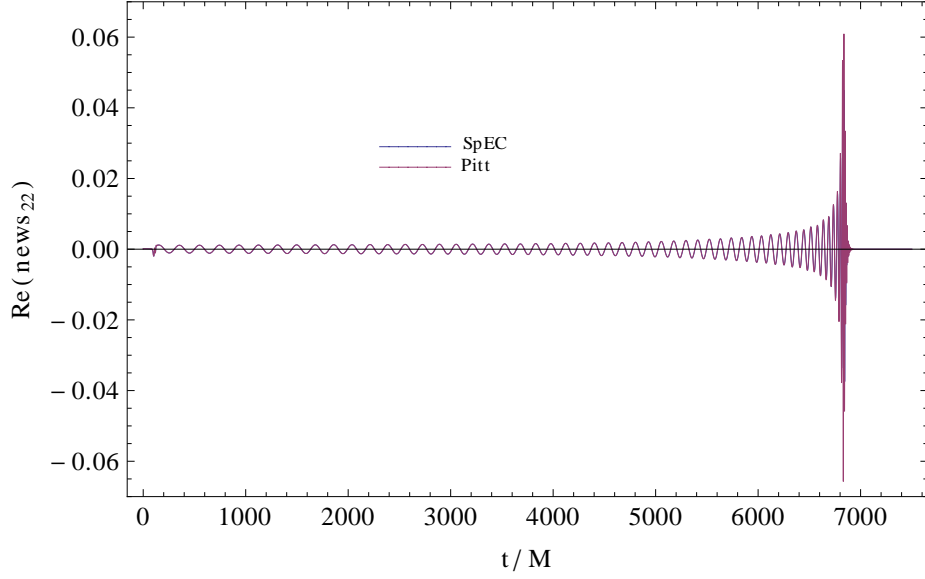


Figure 22: Waveform of the real part of the $(2, 2)$ mode of the news function for the generic precessing binary black hole run, showing 26 orbits, inspiral, merger, and ringdown.

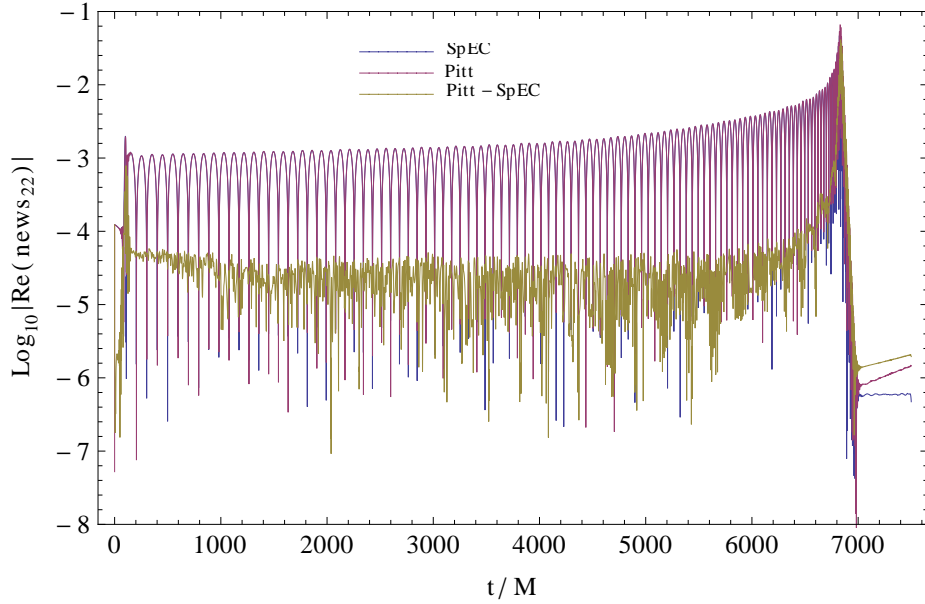


Figure 23: Graphs of $\log_{10} |Re(news_{22})|$ for Pitt and SpEC waveforms for the precessing binary black hole run, showing 16 orbits, inspiral, merger, and ringdown. The difference Pitt - SpEC gives the absolute error $\log_{10} |N_{22Pitt} - N_{22SpEC}|$ between the codes, showing consistent agreement throughout the run.

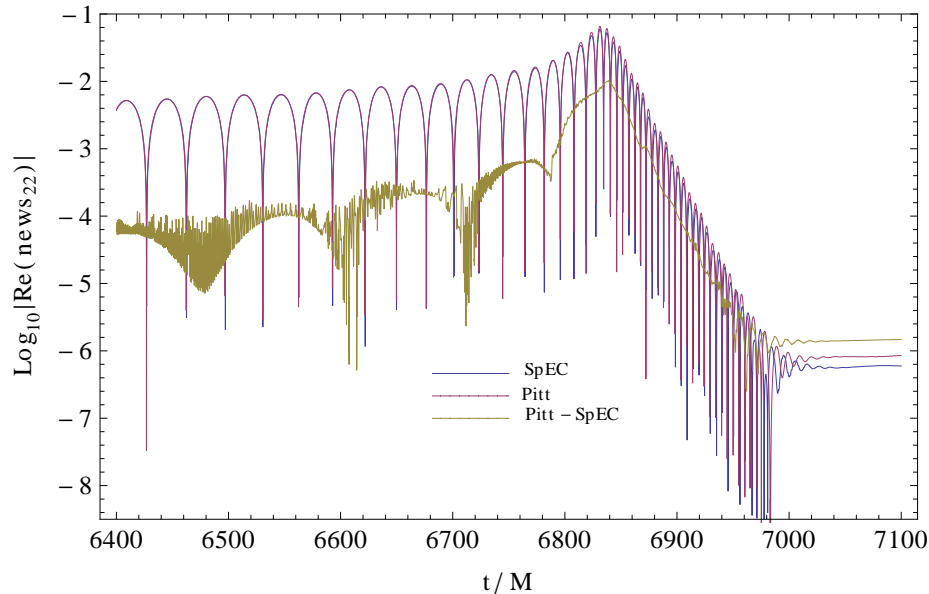


Figure 24: Same graphs as in Fig. 23 but focusing on the merger part of the waveform. Absolute error shows consistency between the Pitt and SpEC news waveforms through merger and ringdown.

“Cauchy-characteristic matching,” in Black Holes, Gravitational Radiation and the Universe, B. R. Iyer and B. Bhawal, eds., ch. 24. Kluwer, Dordrecht, 1998.
 arXiv:gr-qc/9801070.

- [19] M. C. Babiuc, N. T. Bishop, B. Szilágyi, and J. Winicour, “Strategies for the characteristic extraction of gravitational waveforms,” Phys. Rev. D **79** (2009) 084011, arXiv:0808.0861.
- [20] M. C. Babiuc, B. Szilágyi, J. Winicour, and Y. Zlochower, “A characteristic extraction tool for gravitational waveforms,” Phys. Rev. D **84** (Aug, 2011) 044057, arXiv:1011.4223 [gr-qc]. <http://link.aps.org/doi/10.1103/PhysRevD.84.044057>.
- [21] E. Newman and R. Penrose, “An approach to gravitational radiation by a method of spin coefficients,” J. Math. Phys. **3** no. 3, (1962) 566–578.
<http://link.aip.org/link/?JMP/3/566/1>.
- [22] J. Winicour Gen. Rel. and Grav. **19** (1987) 281.
- [23] B. Szilágyi, L. Lindblom, and M. A. Scheel, “Simulations of binary black hole mergers using spectral methods,” Phys. Rev. D **80** (2009) 124010, arXiv:0909.3557 [gr-qc].
- [24] N. W. Taylor, M. Boyle, C. Reisswig, M. A. Scheel, T. Chu, L. E. Kidder, and B. Szilágyi,

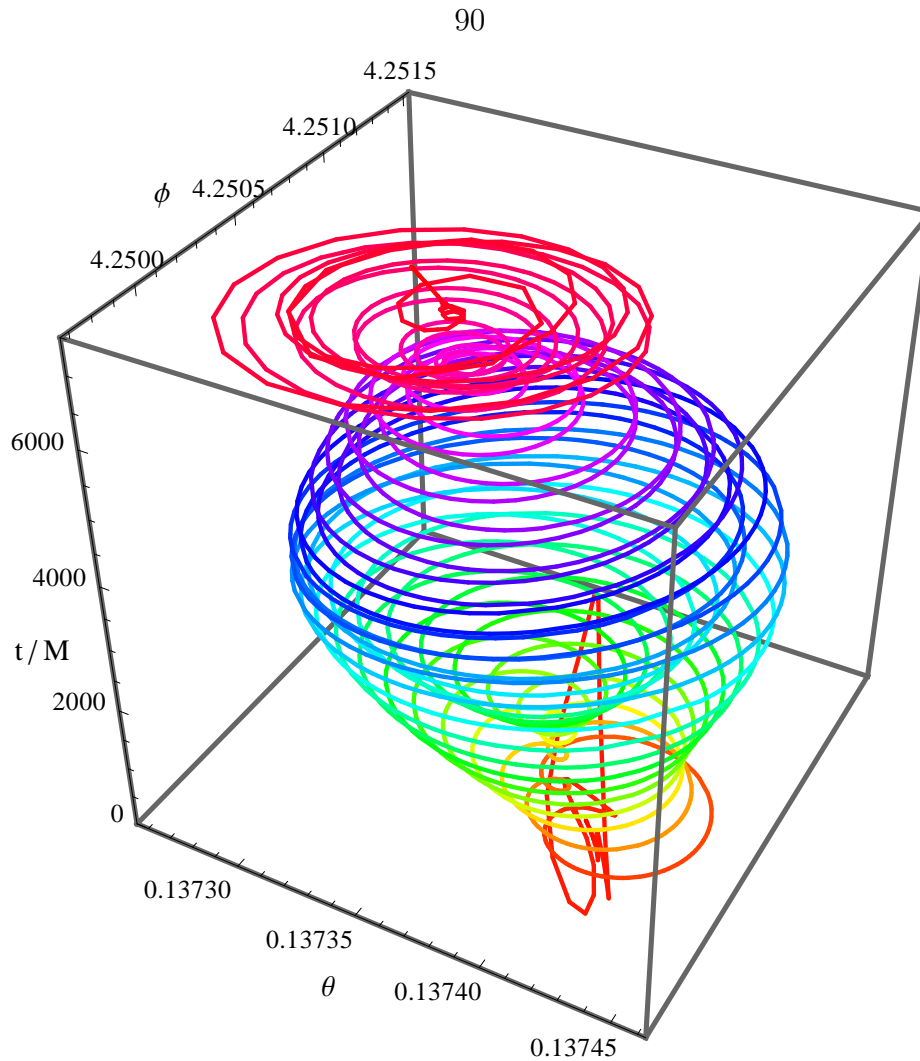


Figure 25: Relative motion of a representative angular coordinate taken from `SpEC3` with extraction radius $R = 100M$ showing a long term helical pattern concordant with the black hole inspiral and merger. Globally, initial oscillation due to junk radiation is aligned primarily along the Cartesian x direction, corresponding to the initial black hole orientation. Coordinate motion is an epicyclic helix whose amplitude is modulated by precession of the orbital plane.

“Comparing gravitational waveform extrapolation to Cauchy-characteristic extraction in binary black hole simulations,” *Phys. Rev. D* **88** (Dec, 2013) 124010, [arXiv:1309.3605](https://arxiv.org/abs/1309.3605) [gr-qc]. <http://link.aps.org/doi/10.1103/PhysRevD.88.124010>.

- [25] A. H. Mroue, M. A. Scheel, B. Szilagyi, H. P. Pfeiffer, M. Boyle, D. A. Hemberger, L. E. Kidder, G. Lovelace, S. Ossokine, N. W. Taylor, A. Zenginoglu, L. T. Buchman, T. Chu,

E. Foley, M. Giesler, R. Owen, and S. A. Teukolsky, “A catalog of 174 binary black hole simulations for gravitational wave astronomy,” Phys. Rev. Lett. **111** (2013) 241104, [arXiv:1304.6077 \[gr-qc\]](#).

Chapter 5 – Strain, news, and flux

Even though Spectral Cauchy characteristic extraction can compute the gauge-free news at \mathcal{I}^+ , the construction and exploitation of the *inertial* metric and its derived quantities remained to be realized.

The first step was the construction of an inertial coordinate system, demonstrated in the previous chapter. This coordinate system, unlocked from the gauge-affected worldtube coordinates, provided a platform for further calculation. With these coordinates, the conformal metric at \mathcal{I}^+ may be transformed to the inertial metric using standard procedures.

One recent key advance was the realization that slices of constant inertial time \tilde{u} are in fact not null but asymptotically time-like, adding an additional term to the formula for the Bondi news. This stems from the requirement that the transformation from worldtube coordinates to inertial coordinates is linear in the inverse areal radial coordinate $\ell = 1/r$, simplifying the calculation of the relevant Jacobian. The inertial frame-derived news was compared with the news computed in the previous chapter and found to converge.

Complete metric information in the domain volume also permits the calculation of the Weyl tensor, which is the traceless, conformally invariant version of the more standard Riemann curvature tensor. While identically zero at \mathcal{I}^+ , the spherical components of the Weyl tensor’s radial derivative enables computation of Ψ_4 , the part relevant to gravitational waves.

Finally, gravitational waves transport energy and momentum. Although “energy” is not necessarily well defined in General Relativity, any space-time symmetry which may be expressed as a field of Killing vectors has a conjugate momentum that is conserved. In this case, time *is* an asymptotic symmetry, expressed with the Killing vector $\xi^{\tilde{\alpha}} = (1, 0, 0, 0)|_{\mathcal{I}^*}$, its conserved conjugate momentum is energy, and the corresponding flux is equivalent to the square of the news $|N|^2$.

In general, any Killing vector representing an asymptotic symmetry generates a corresponding momentum flux that may be calculated analogously to the news.

This paper presents the formalism and method for doing so, as well as the Killing vectors in explicit form. In addition to the ten symmetries and fluxes described in the introduction, there is also a countably infinite set of fluxes arising from the supertranslations. There is a freedom in the choice of initial inertial coordinates — the freefalling coordinates are individually assigned an initial position and velocity. This freedom is an additional symmetry and has its own corresponding flux. Evaluation of the supertranslation flux can help determine the extent to which the initial worldtube coordinates behave as expected.

While energy and linear momentum fluxes have been estimated using other methods, Spectral CCE is the first package that will provide complete flux information. This is particularly interesting for investigating the momentum transfers that occur during “super kick” mergers, precession during long runs, and convergence of the Cauchy evolution under high mass ratios, high spins, and other challenging conditions.

Although initially numerical convergence issues delayed an authoritative computation of the flux, completion and subsequent publication has since been achieved. Serendipitously, the data was found to be convergent in the most power-dense modes.

The inertial flux module required the design of new algorithms to solve equations provided by Jeffrey Winicour, and was operational by early March 2015. Non-null inertial time \tilde{u} was discovered during testing, and the formalism, algorithms, and code continued to evolve. Development continued through my PhD defence on May 12 and was ultimately completed by or before September 14.

A paper was subsequently completed, submitted to CQG in May 2016, and accepted with a minor syntactical revision in September 2016. <http://arxiv.org/abs/1605.04332>

Spectral Cauchy Characteristic Extraction of strain, news and gravitational radiation flux

Casey J. Handmer¹, Béla Szilágyi^{1,2}, Jeffrey Winicour³

¹TAPIR, Walter Burke Institute for Theoretical Physics, MC 350-17, California Institute of Technology, 1200 E California Blvd, Pasadena CA 91125, USA

²Jet Propulsion Laboratory, California Institute of Technology, 4800 Oak Grove Dr. Pasadena CA, 91109, USA

³Department of Physics and Astronomy University of Pittsburgh, Pittsburgh, PA 15260, USA

E-mail: chandmer@caltech.edu

Abstract.

We present a new approach for the Cauchy-characteristic extraction of gravitational radiation strain, news function, and the flux of the energy-momentum, supermomentum and angular momentum associated with the Bondi-Metzner-Sachs asymptotic symmetries. In Cauchy-characteristic extraction, a characteristic evolution code takes numerical data on an inner worldtube supplied by a Cauchy evolution code, and propagates it outwards to obtain the space-time metric in a neighborhood of null infinity. The metric is first determined in a scrambled form in terms of coordinates determined by the Cauchy formalism. In prior treatments, the waveform is first extracted from this metric and then transformed into an asymptotic inertial coordinate system. This procedure provides the physically proper description of the waveform and the radiated energy but it does not generalize to determine the flux of angular momentum or supermomentum. Here we formulate and implement a new approach which transforms the full metric into an asymptotic inertial frame and provides a uniform treatment of all the radiation

fluxes associated with the asymptotic symmetries. Computations are performed and calibrated using the Spectral Einstein Code (SpEC).

PACS numbers: 04.20Ex, 04.25Dm, 04.25Nx, 04.70Bw

1. Introduction

The strong gravitational radiation produced in the inspiral and merger of binary black holes has been a dominant motivation for the construction of gravitational wave observatories. This effort has recently been brought to fruition by the observation of a binary inspiral and merger by the LIGO gravitational wave detectors [1]. The details of the gravitational waveform supplied by numerical simulation is a key theoretical tool to fully complement the sensitivity of the LIGO and Virgo observatories [2, 3, 4, 5], by enhancing the detection and the scientific interpretation of the gravitational signal. Besides the gravitational waveform, the flux of energy-momentum carried off by the waves has important astrophysical effects on the binary system. In particular, the recoil “kick” on the binary due the radiative loss of momentum can possibly eject the final black hole from a galactic center. The strength of such kicks has been computed by various means [6, 7, 8, 9, 10, 11]. The most unambiguous and accurate approach is in terms of the Bondi news function [12], which supplies the gravitational energy and momentum flux at future null infinity \mathcal{I}^+ .

This can be carried out via Cauchy-characteristic extraction (CCE), in which the Cauchy evolution is used to supply the boundary data on a timelike inner worldtube, which then allows a characteristic evolution extending to \mathcal{I}^+ where the radiation is computed using the geometric methods developed by Bondi *et al.* [12], Sachs [13] and Penrose [14]. For a review, see [15]. A version of this initial-boundary value problem based upon a timelike worldtube [16] has been implemented as a characteristic evolution code, the PITT null code [17, 18, 19, 20], and more recently as the **SpEC** characteristic code [21, 22], both of which incorporate a Penrose compactification of the exterior space-time extending to \mathcal{I}^+ . In this way, characteristic evolution

coupled to Cauchy evolution has been implemented to give an accurate numerical computation of the Bondi news function, which determines both the waveform and the radiated energy-momentum.

One technical complication introduced by CCE is that the coordinates induced on \mathcal{I}^+ are related to the Cauchy coordinates on the inner worldtube. Consequently, these computational coordinates do not correspond to inertial observers at \mathcal{I}^+ , i.e. to the coordinates intrinsic to a distant freely falling and non-rotating observatory. Thus, the gravitational waveform first obtained in the “computational coordinates” of CCE is in a scrambled form. Because the news function is an invariant irrespective of coordinate system, the procedure up to now has been to compute it first in the computational coordinates.‡ It is then unscrambled by constructing the transformation between code coordinates and inertial coordinates on \mathcal{I}^+ , as portrayed in Fig. 1. Likewise, a physically relevant calculation of the radiation waveform must also be referred to such inertial coordinates on \mathcal{I}^+ .

In addition to energy-momentum loss, the gravitational radiation of angular momentum has important consequences for the evolution of a relativistic binary system. For a historic account of attempts at a universally accepted definition of angular momentum for radiating systems in general relativity see [24]. At spatial infinity, reasonable asymptotic conditions establish the Poincaré group as the asymptotic symmetry group. This allows a Poincaré covariant definition of angular momentum in which the translation freedom mixes angular momentum with linear momentum in the standard manner [25]. However, the Bondi-Metzner-Sachs (BMS) asymptotic symmetry group [26] at \mathcal{I}^+ has an infinite supertranslation subgroup.

‡ More accurately, the news tensor N_{ab} is a gauge invariant field on \mathcal{I}^+ [23]. The news function $N = \frac{1}{4}N_{ab}q^a q^b$ depends upon a choice of complex polarization dyad q^a , which has gauge freedom. But this freedom can be trivially unwrapped by the construction $N_{ab} = N\bar{q}_a\bar{q}_b + \bar{N}q_aq_b$.

Fortunately, the translations form an invariant subgroup of the BMS group, which leads to an unambiguous definition of energy-momentum. However, although the Lorentz group is a subgroup of the BMS group, the supertranslations lead to a mixing of the associated supermomentum with angular momentum, the physical consequences of which have not been fully explored. For a stationary epoch in the neighborhood of \mathcal{I}^+ , this supertranslation freedom can be removed and the BMS group reduced to the Poincaré group, in which case angular momentum can be well-defined. However, for a system which makes a stationary to stationary transition, the two Poincaré groups obtained at early and late times can be shifted by a supertranslation. Such supertranslation shifts could lead to a distinctly general relativistic mechanism for a system to lose angular momentum. See [27, 28, 29] for discussions. This in fact occurs if the intervening gravitational radiation produces a non-zero gravitational memory effect. A non-zero gravitational radiation memory is equivalent to such a supertranslation shift [30]. In this paper, we develop a unified algorithm for the computation of the gravitational fluxes of energy-momentum, angular momentum and supermomentum to infinity.

There are two distinct approaches for obtaining flux-conserved quantities which form a representation of the BMS asymptotic symmetry group. One approach consists of the BMS linkage integrals $L_\xi(\Sigma)$ [16, 31, 29], which for each spherical cross-section Σ of \mathcal{I}^+ generalize the Komar integrals [32] for exact symmetries to the case of asymptotic Killing vectors ξ^a . Associated with the linkage integrals are locally defined fluxes ${}^L F_\xi$ whose integral determines the change $L_\xi(\Sigma_2) - L_\xi(\Sigma_1)$ between two cross-sections. The second approach, originated by Ashotkar and Streubel, is based upon the Hamiltonian phase space of gravitational radiation modes at \mathcal{I}^+ [33]. The Hamiltonian densities generating a BMS transformation also

geometrically define local fluxes ${}^H F_\xi$. In the case of the supertranslations α^a , Ashetkar and Streubel showed that these Hamiltonian fluxes could be integrated to obtain flux conserved charges $Q_\alpha(\Sigma)$. In the case of the BMS time and space translations, $\xi^a = \tau^a$, the corresponding linkage and Hamiltonian energy-momentum integrals and their fluxes are identical, i.e. $L_\tau(\Sigma) = Q_\tau(\Sigma)$ and ${}^L F_\tau = {}^H F_\tau$. However, their supermomentum fluxes differ locally. Subsequently, Wald and Zoupas [34] generalized the Hamiltonian approach and obtained flux conserved quantities for all the Ashetkar-Streubel Hamiltonian fluxes, including angular momentum. They showed that these flux conserved quantities, including angular momentum, were identical to previous expressions proposed by Dray and Streubel [35].

The relation between the linkage and Hamiltonian BMS fluxes has been examined in [36]. Although their construction and their local values are completely different, it has been shown that the integrals of all the linkage and Hamiltonian fluxes between cross-sections of \mathcal{I}^+ agree, including the angular momentum and supermomentum fluxes, in the most physically relevant case when Σ_2 and Σ_1 are shear-free cross-sections in the limits of infinite future and past retarded time, respectively. Although, for the rotations and boosts a factor-of-two anomaly in the linkages must be taken into account, i.e. $\int_\Sigma {}^L F_\xi dS = 2 \int_\Sigma {}^H F_\xi dS$.

There have been other approaches to defining energy-momentum and angular momentum at \mathcal{I}^+ which do not appeal to the BMS symmetries. Some [35, 37] have been based upon an asymptotic version of Penrose's construction of quasi-local energy-momentum and angular momentum using twistor theory [38]. Another has been based upon the modification of the BMS group to a quasigroup of asymptotic symmetries [39]. Other important work on the computation of the physical properties of radiation at \mathcal{I}^+ has been presented in [40, 41, 42, 43].

Here, we concentrate on the linkage approach because it is readily adapted to previous computational infrastructure treating \mathcal{I}^+ . However, the computational methods presented here should also be useful in computing the Hamiltonian charges and fluxes, as formulated by Wald and Zoupas, which have all the desired physical properties. Although the linkage approach is geometrically well defined, its main physical shortcoming is that the associated supermomentum fluxes do not locally vanish in Minkowski space, although their integrals between cross-sections of \mathcal{I}^+ determined by two Minkowski space light cones do vanish. As a result, the local physical significance of these supermomentum fluxes is unclear, although the local time rate of change of all the linkage fluxes ${}^L\dot{F}_\xi$ do vanish in Minkowski space.

Furthermore, as shown in Sec. 5, in a general radiating spacetime ${}^L\dot{F}_\xi = 0$ for all BMS generators in any region where the Newman-Penrose radiative component of the Weyl tensor ψ_4^0 vanishes. In particular, ${}^L\dot{F}_\xi \rightarrow 0$ for all BMS symmetries in the infinite retarded time past on \mathcal{I}^+ . It is precisely in this limit that the supertranslation freedom can also be eliminated and a preferred Poincaré subgroup can be identified [27]. As a result, the energy-momentum and angular momentum fluxes ${}^L F_\xi$ can be uniquely defined by a retarded time integration of ${}^L\dot{F}_\xi$, using the initial value ${}^L F_\xi = 0$ at $u = -\infty$. Similarly, the energy momentum and angular momentum can also be uniquely defined for such systems by a retarded time integration of ${}^L F_\xi$, using their initial values at $u = -\infty$, or at spatial infinity. However, there remains the possibility of carrying out a similar construction at \mathcal{I}^+ in the infinite retarded time future $u = +\infty$. This leads to the same unresolved issue discussed above for a stationary to stationary transition, i.e. to a net supertranslation shift between the future and past Poincaré groups. The identical supertranslation ambiguity exists in the Hamiltonian description of angular momentum.

As already discussed, in previous applications of CCE to compute energy-momentum loss, the Bondi news function was first computed from the radiation field in the computational coordinates by a gauge invariant method. The news and radiation waveform were then transformed to inertial coordinates on \mathcal{I}^+ . In that approach, it was only necessary to find the 3-dimensional transformation to inertial coordinates intrinsic to \mathcal{I}^+ itself. This procedure is possible because the news function can be defined geometrically, without reference to the BMS symmetries. However, this procedure is not feasible in computing the angular momentum and supermomentum fluxes. Here, we present a unified approach to computing all the BMS fluxes of energy-momentum, angular momentum and supermomentum to infinity by carrying out the transformation to inertial coordinates in a full 4-dimensional neighborhood of \mathcal{I}^+ . We are able to accomplish this by constructing a surprisingly simple transformation between the computational and inertial coordinates. The metric is then transformed to the inertial coordinates, in which the BMS symmetries are readily identified and the corresponding fluxes computed. We formulate a simple computational algorithm for carrying out this transformation.

In this procedure, there remains the freedom of the BMS group in the choice of inertial observers. In special relativistic theories, the corresponding freedom reduces to the translations and Lorentz transformations of the Poincaré group. The BMS supertranslations introduce a gauge freedom in the radiation strain.

2. Waveforms at \mathcal{I}^+

The characteristic formalism is based upon a family of outgoing null hypersurfaces emanating from an inner worldtube and extending to infinity, where they foliate \mathcal{I}^+

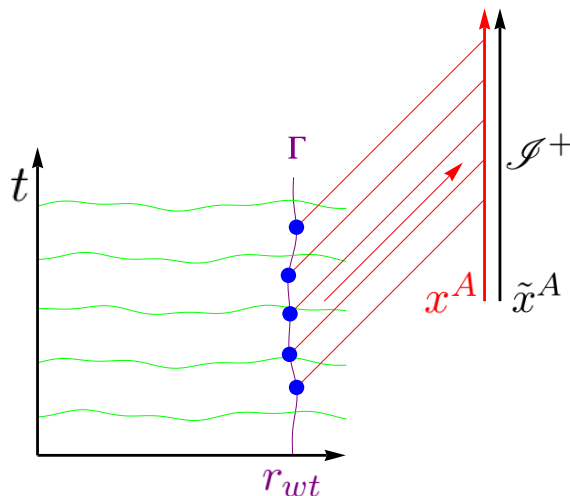


Figure 1: Cauchy characteristic extraction. A Cauchy evolution of the Einstein field equation proceeds on a space-like foliation (green). A finite topologically spherical worldtube Γ at areal radius r_{wt} forms the inner boundary to a characteristic evolution on a null foliation (red). Based on a spherical coordinate system x^A constructed from Cauchy coordinates on the worldtube, gravitational information is propagated to compactified future null infinity \mathcal{I}^+ . At \mathcal{I}^+ , an inertial coordinate system \tilde{x}^A is co-evolved, in which the desired physical waveform can be expressed.

into spherical slices. Let u label these null hypersurfaces, x^A ($A = 2, 3$) be angular coordinates which label the null rays and r be a surface area coordinate. Using the notion of [16], in the resulting (u, r, x^A) coordinates, the metric takes the Bondi-Sachs form

$$ds^2 = - \left(e^{2\beta} \frac{V}{r} - r^2 h_{AB} U^A U^B \right) du^2 - 2e^{2\beta} du dr - 2r^2 h_{AB} U^B du dx^A + r^2 h_{AB} dx^A dx^B, \quad (2.1)$$

where $h^{AB} h_{BC} = \delta_C^A$ and $\det(h_{AB}) = \det(q_{AB})$, with q_{AB} a unit sphere metric.

As described in more detail in [16, 44], in this formalism Einstein's equations decompose into a system which propagate boundary data for the metric variables (β, V, U^A, h_{AB}) on an inner worldtube to a solution at \mathcal{I}^+ . In the Pitt null code and in

the SpEC characteristic code, this solution is computed in a Penrose compactification of \mathcal{I}^+ , e.g. in terms of the coordinates $x^\mu = (u, \ell, x^A)$, where $\ell = 1/r$, $\ell = 0$ at \mathcal{I}^+ .

Then the conformal metric $\hat{g}_{\mu\nu} = \ell^2 g_{\mu\nu}$ is smooth at \mathcal{I}^+ and takes the form

$$\hat{g}_{\mu\nu} dx^\mu dx^\nu = -(\ell^3 e^{2\beta} V - h_{AB} U^A U^B) du^2 + 2e^{2\beta} dud\ell - 2h_{AB} U^B dudx^A + h_{AB} dx^A dx^B. \quad (2.2)$$

General conditions on the asymptotic behavior of the metric variables follow from the vacuum Einstein equations [16],

$$\beta = H + O(\ell^2), \quad (2.3)$$

$$U^A = L^A + 2\ell e^{2H} H^{AB} D_B H + O(\ell^2), \quad (2.4)$$

$$\ell^2 V = D_A L^A + \ell(e^{2H} \mathcal{R}/2 + D_A D^A e^{2H}) + O(\ell^2), \quad (2.5)$$

and

$$h_{AB} = H_{AB} + \ell c_{AB} + O(\ell^2), \quad (2.6)$$

where \mathcal{R} and D_A are the 2-dimensional curvature scalar and covariant derivative associated with H_{AB} and the determinant condition implies

$$H^{AB} c_{AB} = 0. \quad (2.7)$$

The expansion coefficients H , H_{AB} , c_{AB} and L^A (all functions of u and x^A) completely determine the radiation field.

One can further specialize the Bondi coordinates to be *inertial* at \mathcal{I}^+ , i.e. have asymptotic Minkowski form, in which case $H = L^A = 0$, $H_{AB}|_{\mathcal{I}^+} = q_{AB}$ (the unit sphere metric) so that the radiation field is completely determined by c_{AB} , which describes the asymptotic shear of the outgoing null cones or, equivalently, the radiation strain. In these inertial coordinates, the retarded time derivative $\partial_u c_{AB}$

determines the Bondi news function $N(u, x^A)$. However, the characteristic extraction of the waveform is carried out in computational coordinates derived from the Cauchy coordinates on the inner worldtube, so this inertial simplification cannot be assumed.

In previous work the Bondi news function N was first computed in the computational $\hat{g}_{\mu\nu}$ frame. It was then transformed to inertial coordinates (\tilde{u}, \tilde{x}^A) on \mathcal{I}^+ to determine the physical dependence of the waveform on retarded time and angle. Here we construct the transformation to a compactified version of inertial coordinates $(\tilde{u}, \tilde{\ell}, \tilde{x}^A)$ in a full neighborhood of \mathcal{I}^+ .

3. Construction of inertial coordinates

First, we recall some basic elements of Penrose compactification. In a spacetime with metric $g_{\mu\nu}$, the vacuum Einstein equations $G_{\mu\nu} = 0$ expressed in terms of a conformally related metric $\hat{g}_{\mu\nu} = \Omega^2 g_{\mu\nu}$, where $\Omega = 0$ on \mathcal{I}^+ , take the form

$$\Omega^2 \hat{G}_{\mu\nu} + 2\Omega \hat{\nabla}_\mu \hat{\nabla}_\nu \Omega - \hat{g}_{\mu\nu} \left(2\Omega \hat{\nabla}^\rho \hat{\nabla}_\rho \Omega - 3(\hat{\nabla}^\rho \Omega \hat{\nabla}_\rho \Omega) \right) = 0. \quad (3.1)$$

It immediately follows that

$$(\hat{\nabla}^\rho \Omega) \hat{\nabla}_\rho \Omega|_{\mathcal{I}^+} = 0, \quad (3.2)$$

so that \mathcal{I}^+ is a null hypersurface and that

$$[\hat{\nabla}_\mu \hat{\nabla}_\nu \Omega - \frac{1}{4} \hat{g}_{\mu\nu} \hat{\nabla}^\rho \hat{\nabla}_\rho \Omega]|_{\mathcal{I}^+} = 0. \quad (3.3)$$

With respect to this general frame, we now choose $\Omega = \ell$ and computational coordinates (u, ℓ, x^A) , as in Sec. 2, and proceed to construct an inertial conformal frame as follows. We introduce a new conformal factor $\tilde{\Omega} = \omega \Omega = \omega \ell$, with $\tilde{g}_{\mu\nu} = \omega^2 \hat{g}_{\mu\nu}$ such that

$$\tilde{\nabla}^\rho \tilde{\nabla}_\rho \tilde{\Omega}|_{\mathcal{I}^+} = 0, \quad (3.4)$$

by requiring

$$[2\hat{n}^\sigma \partial_\sigma \omega + \omega \hat{\nabla}_\sigma \hat{n}^\sigma]|_{\mathcal{S}^+} = 0, \quad \hat{n}^\sigma = \hat{g}^{\rho\sigma} \nabla_\rho \ell. \quad (3.5)$$

It then follows that

$$\tilde{\nabla}_\mu \tilde{\nabla}_\nu \tilde{\Omega}|_{\mathcal{S}^+} = 0, \quad \tilde{\nabla}^\rho \tilde{\nabla}_\rho \tilde{\Omega}|_{\mathcal{S}^+} = 0, \quad (3.6)$$

i.e. in the $\tilde{g}_{\mu\nu}$ conformal frame \mathcal{S}^+ is null, shear-free and divergence-free. It also follows that

$$\tilde{n}^\sigma \tilde{\nabla}_\sigma \tilde{n}^\nu|_{\mathcal{S}^+} = 0, \quad \tilde{n}^\sigma = \tilde{g}^{\rho\sigma} \tilde{\nabla}_\rho \tilde{\Omega}, \quad (3.7)$$

i.e. in the $\tilde{g}_{\mu\nu}$ frame \tilde{n}^σ is an affinely parametrized null generator of \mathcal{S}^+ .

We now construct inertial conformal coordinates (\tilde{u}, \tilde{x}^A) on \mathcal{S}^+ , by first assigning angular coordinates \tilde{x}^A to each point of some initial spacelike spherical slice $\tilde{u} = u_0$ of \mathcal{S}^+ . We then propagate these coordinates along the null geodesics generating \mathcal{S}^+ according to

$$\tilde{n}^\rho \partial_\rho \tilde{x}^A|_{\mathcal{S}^+} = \omega^{-1} \hat{n}^\rho \partial_\rho \tilde{x}^A|_{\mathcal{S}^+} = 0. \quad (3.8)$$

In addition, we require

$$\tilde{n}^\rho \partial_\rho \tilde{u}|_{\mathcal{S}^+} = \omega^{-1} \hat{n}^\rho \partial_\rho \tilde{u}|_{\mathcal{S}^+} = 1, \quad (3.9)$$

so that \tilde{u} is an affine parameter along the generators in the $\tilde{g}_{\mu\nu}$ conformal frame.

This determines the transformation from the computational coordinates $x^\mu = (u, \ell, x^A)$ to inertial coordinates $(\tilde{u}(u, x^B), \tilde{x}^A(u, x^B))$ on \mathcal{S}^+ , which allows the news function and the extracted waveform to be re-expressed in the physically relevant coordinates of a detector. However, this is not sufficient to identify the BMS symmetries and their associated fluxes. The remaining complication is that after transforming to inertial coordinates the metric on the spherical cross-sections of \mathcal{S}^+ ,

$$H_{\tilde{A}\tilde{B}} = \hat{g}_{\tilde{A}\tilde{B}}|_{\mathcal{S}^+} = \frac{\partial x^\mu}{\partial \tilde{x}^A} \frac{\partial x^\nu}{\partial \tilde{x}^B} \hat{g}_{\mu\nu}|_{\mathcal{S}^+}, \quad (3.10)$$

does not reduce to a unit sphere metric. As a result, the identification of the translations as a subgroup of the supertranslation group is complicated; essentially one must solve an elliptic equation to identify the curved 2-space version of the $\ell = 0$ and $\ell = 1$ spherical harmonics on the spherical cross-sections.

For this purpose, it is simplest to proceed by determining the conformal factor ω relating $H_{\tilde{A}\tilde{B}}$ to a unit-sphere metric $Q_{\tilde{A}\tilde{B}}$,

$$Q_{\tilde{A}\tilde{B}} = \omega^2 H_{\tilde{A}\tilde{B}} . \quad (3.11)$$

We determine ω by solving the elliptic equation governing the conformal transformation of the curvature scalar to the unit sphere curvature,

$$\mathcal{R} = 2(\omega^2 + D_A D^A \log \omega) , \quad (3.12)$$

where \mathcal{R} and D_A are the curvature scalar and covariant derivative associated with the 2-metric H_{AB} . Since this is a scalar equation it can be solved in the computational coordinates.

The elliptic equation (3.12) need only be solved at the initial time. Then, the shear-free property of the null geodesics generating \mathcal{S}^+ implies that ω may be propagated along the generators by means of (3.6), which takes the explicit form

$$2\hat{n}^\alpha \partial_\alpha \log \omega = -e^{-2H} D_A L^A . \quad (3.13)$$

After initialization of ω so that the initial slice of \mathcal{S}^+ has unit sphere geometry, it then follows that all cross-sections of \mathcal{S}^+ have unit sphere geometry. In terms of standard spherical coordinates $\tilde{x}^A = (\tilde{\theta}, \tilde{\phi})$, the induced metric on the cross-sections of \mathcal{S}^+ has components

$$\tilde{g}_{\tilde{A}\tilde{B}}(\tilde{u}, \tilde{x}^A)|_{\mathcal{S}^+} = Q_{\tilde{A}\tilde{B}} , \quad \tilde{g}^{\tilde{A}\tilde{B}}(\tilde{u}, \tilde{x}^A)|_{\mathcal{S}^+} = Q^{\tilde{A}\tilde{B}} , \quad (3.14)$$

where, in these coordinates,

$$Q_{\tilde{A}\tilde{B}}d\tilde{x}^A d\tilde{x}^B = d\tilde{\theta}^2 + \sin^2 \tilde{\theta} d\tilde{\phi}^2 . \quad (3.15)$$

Given such inertial coordinates on \mathcal{S}^+ , we then extend them to coordinates $\tilde{x}^\mu = (\tilde{u}, \tilde{\ell}, \tilde{x}^A)$ in a neighborhood of \mathcal{S}^+ , where

$$\tilde{\ell} = \omega(u, x^A)\ell = \tilde{\Omega} . \quad (3.16)$$

The Jacobian of the transformation from computational to inertial coordinates has the simple property

$$\partial_{\tilde{\ell}}\tilde{u} = \partial_{\tilde{\ell}}\tilde{x}^A = 0 , \quad \partial_{\tilde{\ell}}\tilde{\ell} = \omega . \quad (3.17)$$

As a result it immediately follows that at \mathcal{S}^+ the metric reduces to the simple form

$$\tilde{g}_{\tilde{A}\tilde{B}}(\tilde{u}, \tilde{x}^A)|_{\mathcal{S}^+} = Q_{\tilde{A}\tilde{B}} , \quad \tilde{g}^{\tilde{A}\tilde{B}}(\tilde{u}, \tilde{x}^A)|_{\mathcal{S}^+} = Q^{\tilde{A}\tilde{B}} , \quad (3.18)$$

$$\tilde{g}_{\tilde{u}\tilde{u}}(\tilde{u}, \tilde{x}^A)|_{\mathcal{S}^+} = \tilde{g}_{\tilde{u}\tilde{A}}(\tilde{u}, \tilde{x}^A)|_{\mathcal{S}^+} = \tilde{g}^{\tilde{\ell}\tilde{\ell}}(\tilde{u}, \tilde{x}^A)|_{\mathcal{S}^+} = \tilde{g}^{\tilde{\ell}\tilde{A}}(\tilde{u}, \tilde{x}^A)|_{\mathcal{S}^+} = 0 . \quad (3.19)$$

This transformation to inertial coordinates also determines the metric in a neighborhood of \mathcal{S}^+ , which simplifies the identification of the BMS group and the computation of the radiation strain and BMS fluxes.

4. The BMS group

In the inertial coordinates and conformal frame constructed in Sec. 3, the asymptotic Killing vectors composing the BMS group can be described by by [13, 16]

$$\xi^{\tilde{\rho}}\partial_{\tilde{\rho}}|_{\mathcal{S}^+} = \left(\alpha(\tilde{x}^A) + \frac{1}{2}\tilde{u}f_{:\tilde{A}}^{\tilde{A}} \right) \partial_{\tilde{u}} + f^{\tilde{A}}\partial_{\tilde{A}} , \quad (4.1)$$

where a ‘‘colon’’ denotes the covariant derivative with respect to the unit sphere metric $Q_{\tilde{A}\tilde{B}}$, $\alpha(\tilde{x}^A)$ represents the supertranslation freedom and $f^{\tilde{A}}(\tilde{x}^B)$ is a conformal Killing vector on the unit sphere,

$$f^{(\tilde{A}:\tilde{B})} = \frac{1}{2}Q^{\tilde{A}\tilde{B}}f_{:\tilde{C}}^{\tilde{C}} . \quad (4.2)$$

This conformal group is isomorphic to the Lorentz group.

The additional property that ξ^μ is tangent to \mathcal{I}^+ ,

$$\xi^{\tilde{\ell}}|_{\mathcal{I}^+} = \xi^\rho \partial_\rho \tilde{\Omega}|_{\mathcal{I}^+} = 0, \quad (4.3)$$

implies that ξ^μ satisfies the asymptotic Killing equation in the physical space geometry,

$$\tilde{\Omega}^{-2} \nabla^{(\mu} \xi^{\nu)}|_{\mathcal{I}^+} = [\tilde{\nabla}^{(\tilde{\mu}} \xi^{\tilde{\nu})} - \tilde{\Omega}^{-1} \tilde{g}^{\tilde{\mu}\tilde{\nu}} \xi^{\tilde{\rho}} \tilde{\nabla}_{\tilde{\rho}} \tilde{\Omega}]|_{\mathcal{I}^+} = 0. \quad (4.4)$$

The supertranslations form an invariant subgroup of the BMS group for which $f^{\tilde{A}} = 0$. The translations are an invariant 4-parameter subgroup of the supertranslations for which $\alpha(\tilde{x}^A)$ is composed of $\ell = 0$ and $\ell = 1$ spherical harmonics. The rotation subgroup intrinsic to a cross-section Σ^+ of \mathcal{I}^+ consists of the BMS transformations which map Σ^+ onto itself. Without introducing any artificially preferred structure on \mathcal{I}^+ , there is no invariant way to extract a rotation group, Lorentz group or Poincaré group from the BMS group.

Given a cross-section Σ^+ of \mathcal{I}^+ and a generator ξ^μ of the BMS group, the linkage integral $L_\xi(\Sigma^+)$ which generalizes the Komar integral for an exact symmetry is given in terms of the physical space geometry by

$$L_\xi(\Sigma^+) = \lim_{\Sigma \rightarrow \Sigma^+} \oint_\Sigma (\nabla^{[\mu} \xi^{\mu]} - K^{[\mu} N^{\nu]} \nabla_\rho \xi^\rho) dS_{\mu\nu}, \quad (4.5)$$

where K^μ and N^μ are, respectively, ingoing and outgoing null vectors normal to Σ , normalized by $K^\mu N_\mu = -1$. The limit is taken along the outgoing null hypersurface \mathcal{N} emanating from Σ to Σ^+ , as shown in Fig. 2. The value of this limit depends upon how the BMS generator is extended off \mathcal{I}^+ . The asymptotic symmetry condition (4.4) allows the freedom in this extension of the form

$$\xi^\mu \rightarrow \xi^\mu + \tilde{\Omega}^2 v^\mu. \quad (4.6)$$

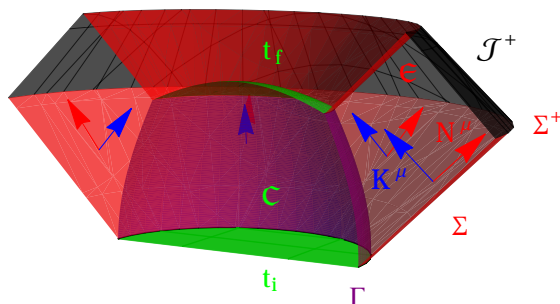


Figure 2: Diagram of the computational domain under Penrose compactification, with angle $\tilde{\theta}$ suppressed. The Cauchy evolution \mathcal{C} runs from time t_i to t_f within the worldtube Γ . The characteristic evolution \mathcal{E} is performed on null hypersurfaces extending from Γ to future null infinity \mathcal{I}^+ . Cross-sections Σ of a null hypersurface (topologically a 2-sphere) approach the limit Σ^+ at \mathcal{I}^+ , where the linkage integral is defined. Ingoing (K^μ) and outgoing (N^μ) null vectors are normal to Σ . Gauge independent news, strain, ψ_4^0 and flux are computed in inertial coordinates at \mathcal{I}^+ .

In the original formulation of the linkages [16], v^μ was determined by a null hypersurface propagation law on \mathcal{N} ,

$$(\nabla^{(\mu} \xi^{\nu)} - \frac{1}{2} g^{\mu\nu} \nabla_\rho \xi^\rho) K_\mu = 0. \quad (4.7)$$

In [29], other choices of propagation law were considered. In the next section, we adopt a simple extension in which the generators ξ^μ only depend linearly on the inertial conformal factor $\tilde{\ell}$.

5. The BMS fluxes

Our focus is on the radiation flux F_ξ across \mathcal{I}^+ which governs the change of linkage between two cross-sections,

$$L_\xi(\Sigma_2) - L_\xi(\Sigma_1) = \int_{\Sigma_1^+}^{\Sigma_2^+} F_\xi dV. \quad (5.1)$$

In a conformal frame in which \mathcal{S}^+ is divergence-free, it was shown in [29] that there is a local geometric expression for F_ξ which is independent of the freedom (4.6) governing the extension of ξ^μ off \mathcal{S}^+ . The resulting flux is uniquely determined by (i) the choice of ξ^μ on \mathcal{S}^+ and (ii) the local conformal geometry near \mathcal{S}^+ ; and (iii) it is independent of any choice of cross-section or other extraneous constructs.

In the $\tilde{g}_{\tilde{\mu}\tilde{\nu}}$ conformal inertial frame described in Sec. 3, this flux is constructed as follows. The transformation from the computational coordinates $x^\mu(u, \ell, x^A)$ to inertial coordinates $(\tilde{u}(u, x^B), \tilde{x}^A(u, x^B))$ on \mathcal{S}^+ is first extended to coordinates $\tilde{x}^\mu = (\tilde{u}, \tilde{\ell}, \tilde{x}^A)$ in a neighborhood of \mathcal{S}^+ where, as before,

$$\tilde{\ell} = \omega(u, x^A)\ell = \tilde{\Omega} . \quad (5.2)$$

This transformation determines the metric in the extension of the inertial frame to a neighborhood of \mathcal{S}^+ ,

$$\tilde{g}^{\tilde{\mu}\tilde{\nu}}(\tilde{u}, \tilde{\ell}, \tilde{x}^A) = \omega^{-2} \frac{\partial \tilde{x}^\mu}{\partial x^\alpha} \frac{\partial \tilde{x}^\nu}{\partial x^\beta} \hat{g}^{\alpha\beta}(u, \ell, x^A) . \quad (5.3)$$

In addition to (3.18) and (3.19), this implies

$$\begin{aligned} \tilde{g}^{\tilde{u}\tilde{\ell}}(\tilde{u}, 0, \tilde{x}^A) &= 1 , \\ \tilde{g}^{\tilde{u}\tilde{u}}(\tilde{u}, 0, \tilde{x}^A) &= \omega^{-2} \frac{\partial \tilde{u}}{\partial x^A} \frac{\partial \tilde{u}}{\partial x^B} \hat{g}^{AB} , \\ \tilde{g}^{\tilde{u}\tilde{A}}(\tilde{u}, 0, \tilde{x}^A) &= \omega^{-2} \frac{\partial \tilde{u}}{\partial x^B} \frac{\partial \tilde{x}^A}{\partial x^C} \hat{g}^{BC} . \end{aligned} \quad (5.4)$$

The corresponding covariant components are

$$\begin{aligned} \tilde{g}_{\tilde{u}\tilde{\ell}}(\tilde{u}, 0, \tilde{x}^A) &= 1 , \\ \tilde{g}_{\tilde{\ell}\tilde{\ell}}(\tilde{u}, 0, \tilde{x}^A) &= -\tilde{g}^{\tilde{u}\tilde{u}} + Q_{\tilde{A}\tilde{B}} \tilde{g}^{\tilde{u}\tilde{A}} \tilde{g}^{\tilde{u}\tilde{B}} , \\ \tilde{g}_{\tilde{\ell}\tilde{A}}(\tilde{u}, 0, \tilde{x}^A) &= -Q_{\tilde{A}\tilde{B}} \tilde{g}^{\tilde{u}\tilde{B}} . \end{aligned} \quad (5.5)$$

Note that the \tilde{x}^μ coordinates are not null coordinates. While the $\tilde{u} = \text{const}$ cross-sections of \mathcal{S}^+ are space-like, (5.4) implies in general that $\tilde{g}^{\tilde{u}\tilde{u}} > 0$ so that the

$\tilde{u} = \text{const}$ hypersurfaces in the neighborhood of \mathcal{S}^+ are asymptotically time-like. This somewhat surprising feature stems from the requirement that the transformation from computational coordinates to inertial coordinates is linear in ℓ . The transformation to the \tilde{x}^μ inertial coordinates determines the essential geometric quantities associated with the inertial frame metric $\tilde{g}_{\tilde{\mu}\tilde{\nu}}$, e.g. the associated covariant derivative $\tilde{\nabla}_{\tilde{\mu}}$ and curvature scalar \tilde{R} .

Restrictions on the $\tilde{\ell}$ -derivatives of the inertial metric at \mathcal{S}^+ arise from (3.6),

$$\begin{aligned}\partial_{\tilde{\ell}}\tilde{g}_{\tilde{u}\tilde{u}}|_{\mathcal{S}^+} &= 0, \\ \partial_{\tilde{\ell}}\tilde{g}_{\tilde{u}\tilde{\ell}}|_{\mathcal{S}^+} &= \frac{1}{2}\partial_{\tilde{u}}\tilde{g}_{\tilde{\ell}\tilde{\ell}}|_{\mathcal{S}^+}, \\ \partial_{\tilde{\ell}}\tilde{g}_{\tilde{u}\tilde{A}}|_{\mathcal{S}^+} &= \partial_{\tilde{u}}\tilde{g}_{\tilde{A}\tilde{\ell}}|_{\mathcal{S}^+}.\end{aligned}\tag{5.6}$$

In addition,

$$\tilde{g}_{\tilde{u}\tilde{\ell}} = \frac{\partial u}{\partial \tilde{u}}\omega e^{2\beta},\tag{5.7}$$

so since (2.3) implies $\partial_{\tilde{\ell}}\beta|_{\mathcal{S}^+} = 0$, we have

$$\partial_{\tilde{\ell}}\tilde{g}_{\tilde{u}\tilde{\ell}}|_{\mathcal{S}^+} = \partial_{\tilde{u}}\tilde{g}_{\tilde{\ell}\tilde{\ell}}|_{\mathcal{S}^+} = 0.\tag{5.8}$$

The determinant condition (2.7), i.e. $h^{AB}\partial_{\ell}h_{AB}|_{\mathcal{S}^+} = 0$ implies

$$\left\{Q^{\tilde{A}\tilde{B}}\partial_{\tilde{\ell}}\tilde{g}_{\tilde{A}\tilde{B}} + 2\tilde{g}^{\tilde{u}\tilde{A}}\partial_{\tilde{\ell}}\tilde{g}_{\tilde{u}\tilde{A}}\right\}|_{\mathcal{S}^+} = 0,\tag{5.9}$$

so that

$$\left\{Q^{\tilde{A}\tilde{B}}\partial_{\tilde{\ell}}\tilde{g}_{\tilde{A}\tilde{B}} + 2\tilde{g}^{\tilde{u}\tilde{A}}\partial_{\tilde{u}}\tilde{g}_{\tilde{\ell}\tilde{A}}\right\}|_{\mathcal{S}^+} = \left\{Q^{\tilde{A}\tilde{B}}\partial_{\tilde{\ell}}\tilde{g}_{\tilde{A}\tilde{B}} - 2Q_{\tilde{A}\tilde{B}}\tilde{g}^{\tilde{u}\tilde{A}}\partial_{\tilde{u}}\tilde{g}^{\tilde{u}\tilde{B}}\right\}|_{\mathcal{S}^+} = 0.\tag{5.10}$$

The corresponding contravariant components satisfy

$$\begin{aligned}\partial_{\tilde{\ell}}\tilde{g}^{\tilde{\ell}\tilde{\ell}}|_{\mathcal{S}^+} &= 0, \\ \partial_{\tilde{\ell}}\tilde{g}^{\tilde{\ell}\tilde{A}}|_{\mathcal{S}^+} &= \partial_{\tilde{u}}\tilde{g}^{\tilde{u}\tilde{A}}|_{\mathcal{S}^+}, \\ \partial_{\tilde{\ell}}\tilde{g}^{\tilde{u}\tilde{\ell}}|_{\mathcal{S}^+} &= \frac{1}{2}\partial_{\tilde{u}}\tilde{g}^{\tilde{u}\tilde{u}}|_{\mathcal{S}^+} = Q_{\tilde{A}\tilde{B}}\tilde{g}^{\tilde{u}\tilde{A}}\partial_{\tilde{u}}\tilde{g}^{\tilde{u}\tilde{B}}|_{\mathcal{S}^+}, \\ Q_{\tilde{A}\tilde{B}}\partial_{\tilde{\ell}}\tilde{g}^{\tilde{A}\tilde{B}}|_{\mathcal{S}^+} &= 0.\end{aligned}\tag{5.11}$$

In general, since $\xi^{\tilde{\mu}}$ is tangent to \mathcal{S}^+ , we can define a smooth scalar field $K = \tilde{\Omega}^{-1}\xi^{\tilde{\mu}}\partial_{\tilde{\mu}}\tilde{\Omega}$ and the asymptotic Killing equation (4.4) implies we can define a smooth field $X^{\tilde{\mu}\tilde{\nu}}$ according to

$$\tilde{\nabla}^{(\tilde{\mu}}\xi^{\tilde{\nu})} = K\tilde{g}^{\tilde{\mu}\tilde{\nu}} + \tilde{\Omega}X^{\tilde{\mu}\tilde{\nu}}. \quad (5.12)$$

We write $X = X_{\tilde{\mu}}^{\tilde{\mu}}$. In the $\tilde{g}_{\tilde{\mu}\tilde{\nu}}$ inertial frame,

$$K = \tilde{\ell}^{-1}\xi^{\tilde{\ell}}, \quad (5.13)$$

so that

$$K|_{\mathcal{S}^+} = \frac{\partial\xi^{\tilde{\ell}}}{\partial\tilde{\ell}}|_{\mathcal{S}^+}. \quad (5.14)$$

Evaluation of (5.12) at \mathcal{S}^+ gives, in addition to (4.1),

$$\begin{aligned} \frac{\partial\xi^{\tilde{\ell}}}{\partial\tilde{\ell}}|_{\mathcal{S}^+} &= \frac{\partial\xi^{\tilde{u}}}{\partial\tilde{u}}|_{\mathcal{S}^+} = \frac{1}{2}\xi^{\tilde{A}}|_{\mathcal{S}^+}, \\ \frac{\partial\xi^{\tilde{u}}}{\partial\tilde{\ell}}|_{\mathcal{S}^+} &= \left\{-\tilde{g}^{\tilde{u}\tilde{A}}\frac{\partial\xi^{\tilde{u}}}{\partial x^{\tilde{A}}} + \frac{1}{2}\xi^{\tilde{u}}\frac{\partial\tilde{g}^{\tilde{u}\tilde{u}}}{\partial\tilde{u}} + \frac{1}{2}\xi^{\tilde{A}}\frac{\partial\tilde{g}^{\tilde{u}\tilde{u}}}{\partial x^{\tilde{A}}}\right\}|_{\mathcal{S}^+}, \\ \frac{\partial\xi^{\tilde{A}}}{\partial\tilde{\ell}}|_{\mathcal{S}^+} &= \left\{\tilde{g}^{\tilde{A}\tilde{u}}\frac{\partial\xi^{\tilde{u}}}{\partial\tilde{u}} - \tilde{g}^{\tilde{u}\tilde{B}}\xi^{\tilde{A}}{}_{;\tilde{B}} + \xi^{\tilde{B}}g^{\tilde{u}\tilde{A}}{}_{;\tilde{B}} + \xi^{\tilde{u}}\frac{\partial\tilde{g}^{\tilde{u}\tilde{A}}}{\partial\tilde{u}} - Q^{\tilde{A}\tilde{B}}\frac{\partial\xi^{\tilde{u}}}{\partial x^{\tilde{B}}}\right\}|_{\mathcal{S}^+}. \end{aligned} \quad (5.15)$$

As shown in [29], it also follows that

$$X^{\tilde{\mu}\tilde{\nu}}\partial_{\tilde{\nu}}\tilde{\Omega}|_{\mathcal{S}^+} = 0, \quad (5.16)$$

which results from a straightforward calculation using (3.19), (5.13) and (5.15). Thus we can further define a smooth field $X^{\tilde{\mu}}$ according to

$$X^{\tilde{\mu}} = \tilde{\Omega}^{-1}X^{\tilde{\mu}\tilde{\nu}}\partial_{\tilde{\nu}}\tilde{\Omega}. \quad (5.17)$$

Let $Q^{\tilde{A}}(\tilde{x}^{\tilde{B}})$ be a complex polarization dyad satisfying

$$Q^{(\tilde{A}}\bar{Q}^{\tilde{B})} = Q^{\tilde{A}\tilde{B}}. \quad (5.18)$$

We have

$$Q^{\tilde{A}}Q^{\tilde{B}}\partial_{\tilde{\ell}}\tilde{g}_{\tilde{A}\tilde{B}}|_{\mathcal{S}^+} = -Q_{\tilde{A}}\bar{Q}_{\tilde{B}}\left\{\partial_{\tilde{\ell}}\tilde{g}^{\tilde{A}\tilde{B}} - 2\tilde{g}^{\tilde{u}\tilde{A}}\partial_{\tilde{u}}\tilde{g}^{\tilde{u}\tilde{B}}\right\}|_{\mathcal{S}^+}. \quad (5.19)$$

The outgoing null vector normal to the ($\tilde{u} = \text{const}, \tilde{\ell} = \text{const}$) 2-surfaces is

$$N_{\tilde{\alpha}} = \partial_{\tilde{\alpha}} \tilde{u} - \frac{1}{2} \tilde{g}^{\tilde{u}\tilde{u}} \partial_{\tilde{\alpha}} \tilde{\ell} . \quad (5.20)$$

The shear or asymptotic strain h on a constant inertial time cross-section of \mathcal{I}^+ is then given by

$$h = \frac{1}{2} Q^{\tilde{A}} Q^{\tilde{B}} \tilde{\nabla}_{\tilde{A}} N_{\tilde{B}}|_{\mathcal{I}^+} , \quad (5.21)$$

so that

$$h = \frac{1}{4} Q^{\tilde{A}} Q^{\tilde{B}} \left\{ \partial_{\tilde{\ell}} \tilde{g}_{\tilde{A}\tilde{B}} - 2\tilde{g}_{\tilde{\ell}\tilde{A}:\tilde{B}} \right\} |_{\mathcal{I}^+} , \quad (5.22)$$

$$= \frac{1}{4} Q_{\tilde{A}} Q_{\tilde{B}} \left\{ 2\tilde{g}^{\tilde{A}\tilde{u}} \partial_{\tilde{u}} \tilde{g}^{\tilde{B}\tilde{u}} + 2\tilde{g}^{\tilde{u}\tilde{A}:\tilde{B}} - \partial_{\tilde{\ell}} \tilde{g}^{\tilde{A}\tilde{B}} \right\} |_{\mathcal{I}^+} . \quad (5.23)$$

Here,

$$\partial_{\tilde{\ell}} \tilde{g}^{\tilde{A}\tilde{B}} = \omega^{-2} x^{\tilde{A}}{}_{,C} x^{\tilde{B}}{}_{,D} \ell_{,\tilde{\ell}} \partial_{\tilde{\ell}} \hat{g}^{CD} = \omega^{-3} x^{\tilde{A}}{}_{,C} x^{\tilde{B}}{}_{,D} \partial_{\tilde{\ell}} \hat{g}^{CD} . \quad (5.24)$$

The strain h has gauge freedom corresponding to the supertranslation freedom in the choice of slicing of \mathcal{I}^+ . A gauge independent description of the radiation waveform is given by the news function

$$N = \frac{1}{2} Q_{\tilde{A}} Q_{\tilde{B}} X^{\tilde{A}\tilde{B}}|_{\mathcal{I}^+} = \partial_{\tilde{u}} h , \quad (5.25)$$

where $X^{\tilde{A}\tilde{B}}$ corresponds to the translation

$$\xi^{\tilde{\alpha}}|_{\mathcal{I}^+} = \tilde{\nabla}^{\tilde{\alpha}} \tilde{\ell}|_{\mathcal{I}^+} = (1, 0, 0, 0) , \quad (5.26)$$

with

$$\partial_{\tilde{\ell}} \xi^{\tilde{\alpha}}|_{\mathcal{I}^+} = \partial_{\tilde{u}} \left(\frac{1}{2} \tilde{g}^{\tilde{u}\tilde{u}}, 0, \tilde{g}^{\tilde{u}\tilde{A}} \right) |_{\mathcal{I}^+} . \quad (5.27)$$

A short calculation gives

$$N = \frac{1}{4} Q_{\tilde{A}} Q_{\tilde{B}} \partial_{\tilde{u}} (2\tilde{g}^{\tilde{u}\tilde{A}:\tilde{B}} + 2\tilde{g}^{\tilde{u}\tilde{A}} \partial_{\tilde{u}} \tilde{g}^{\tilde{u}\tilde{B}} - \partial_{\tilde{\ell}} \tilde{g}^{\tilde{A}\tilde{B}}) , \quad (5.28)$$

in accordance with (5.23) and (5.25).

The absolute square of the news function determines the flux of energy and momentum. The flux corresponding to a general asymptotic symmetry is given by [29]

$$F_\xi = -\tilde{\nabla}_{\tilde{\mu}}\tilde{\nabla}_{\tilde{\nu}}X^{\tilde{\mu}\tilde{\nu}} + 3\tilde{\nabla}_{\tilde{\mu}}X^{\tilde{\mu}} + \frac{3}{4}\tilde{\nabla}_{\tilde{\mu}}\tilde{\nabla}^{\tilde{\mu}}X + \frac{1}{24}\tilde{R}X. \quad (5.29)$$

Note that F_ξ is a scalar so that it could be evaluated in any coordinate system.

However, its physical properties are only manifest in the inertial \tilde{x}^μ coordinates.

Since F_ξ is independent of the freedom (4.6), it suffices to extend the BMS generators to a neighborhood of \mathcal{I}^+ with the linear $\tilde{\ell}$ -dependence

$$\xi^{\tilde{\mu}}(\tilde{u}, \tilde{\ell}, \tilde{x}^A) = \xi^{\tilde{\mu}}(\tilde{u}, 0, \tilde{x}^A) + \tilde{\ell} \frac{\partial \xi^{\tilde{\mu}}}{\partial \tilde{\ell}}(\tilde{u}, 0, \tilde{x}^A), \quad (5.30)$$

where the coefficients are determined by (4.1) and (5.15). This determines the asymptotic Killing vectors in the neighborhood of \mathcal{I}^+ for the purpose of computing the flux in terms of (5.29).

It is also possible to compute the time derivative of the flux in terms of its relation to the Weyl tensor [29],

$$\dot{F}_\xi := \tilde{n}^\mu \partial_\mu F_\xi = -\Omega^{-1} \tilde{C}_{\alpha\beta\gamma\delta} \tilde{n}^\beta \tilde{n}^\delta X^{\alpha\gamma}|_{\mathcal{I}^+}, \quad (5.31)$$

where asymptotic flatness implies $C_{\alpha\beta\gamma\delta} = O(\Omega)$. In inertial coordinates, in which $X^{\tilde{a}\tilde{\ell}}|_{\mathcal{I}^+} = 0$, this reduces to

$$\dot{F}_\xi = \partial_{\tilde{u}} F_\xi = -\partial_{\tilde{\ell}} \tilde{C}_{\tilde{A}\tilde{u}\tilde{B}\tilde{u}} X^{\tilde{A}\tilde{B}}|_{\mathcal{I}^+}. \quad (5.32)$$

By virtue of the trace-free property of the Weyl tensor this may be rewritten

$$\partial_{\tilde{u}} F_\xi = -\frac{1}{4} \{ \partial_{\tilde{\ell}} \tilde{C}_{\tilde{A}\tilde{u}\tilde{B}\tilde{u}} Q^{\tilde{A}} Q^{\tilde{B}} X^{\tilde{C}\tilde{D}} \bar{Q}_{\tilde{C}} \bar{Q}_{\tilde{D}} + \partial_{\tilde{\ell}} \tilde{C}_{\tilde{A}\tilde{u}\tilde{B}\tilde{u}} \bar{Q}^{\tilde{A}} \bar{Q}^{\tilde{B}} X^{\tilde{C}\tilde{D}} Q_{\tilde{C}} Q_{\tilde{D}} \} |_{\mathcal{I}^+}, \quad (5.33)$$

or

$$\partial_{\tilde{u}} F_\xi = \Psi \bar{\mathcal{X}} + \bar{\Psi} \mathcal{X}, \quad (5.34)$$

where $\mathcal{X} = \frac{1}{2}X^{\tilde{A}\tilde{B}}Q_{\tilde{A}}Q_{\tilde{B}}|_{\mathcal{I}^+}$ and $\Psi = -\frac{1}{2}\partial_{\tilde{\ell}}\tilde{C}^{\tilde{A}\tilde{B}\tilde{u}}Q^{\tilde{A}}Q^{\tilde{B}}|_{\mathcal{I}^+}$. In Newman-Penrose notation $\bar{\Psi}$ is the asymptotic ψ_4^0 component of the Weyl tensor.

A straightforward computation based upon (5.12) gives

$$\begin{aligned}\mathcal{X} &= \frac{1}{2}X^{\tilde{A}\tilde{B}}Q_{\tilde{A}}Q_{\tilde{B}}|_{\mathcal{I}^+}, \\ &= \frac{1}{4}Q_{\tilde{A}}Q_{\tilde{B}}\{2(\partial_{\tilde{\ell}}\tilde{g}^{\tilde{A}\tilde{C}})\xi^{\tilde{B}}{}_{:\tilde{C}} - (\partial_{\tilde{\ell}}\tilde{g}^{\tilde{A}\tilde{B}})_{:\tilde{C}}\xi^{\tilde{C}} - \frac{3}{2}(\partial_{\tilde{\ell}}\tilde{g}^{\tilde{A}\tilde{B}})\xi^{\tilde{C}}{}_{:\tilde{C}} + 2(\partial_{\tilde{\ell}}\xi^{\tilde{B}})_{:\tilde{A}} \\ &\quad + 2(\partial_{\tilde{\ell}}\tilde{g}^{\tilde{A}\tilde{\ell}})\partial_{\tilde{\ell}}\xi^{\tilde{B}} + 2\tilde{g}^{\tilde{A}\tilde{u}}\partial_{\tilde{u}}\partial_{\tilde{\ell}}\xi^{\tilde{B}} - (\partial_{\tilde{u}}\partial_{\tilde{\ell}}\tilde{g}^{\tilde{A}\tilde{B}})\xi^{\tilde{u}}\}|_{\mathcal{I}^+}.\end{aligned}\tag{5.35}$$

Here the $\partial_{\tilde{\ell}}\xi^{\tilde{A}}$ derivative of the Killing field is supplied from (5.15). Using the properties of $\xi^\alpha|_{\mathcal{I}^+}$ and $\partial_{\tilde{\ell}}\tilde{g}^{\tilde{A}\tilde{\ell}}|_{\mathcal{I}^+}$, this reduces to

$$\begin{aligned}\mathcal{X} &= \frac{1}{4}Q_{\tilde{A}}Q_{\tilde{B}}\{(\partial_{\tilde{\ell}}\tilde{g}^{\tilde{A}\tilde{B}})\xi^{\tilde{C}:\tilde{D}}Q_{[\tilde{C}}Q_{\tilde{D}]} - (\partial_{\tilde{\ell}}\tilde{g}^{\tilde{A}\tilde{B}})_{:\tilde{C}}\xi^{\tilde{C}} \\ &\quad + 2(\partial_{\tilde{\ell}}\xi^{\tilde{B}})_{:\tilde{A}} + \partial_{\tilde{u}}(2\tilde{g}^{\tilde{A}\tilde{u}}\partial_{\tilde{\ell}}\xi^{\tilde{B}} - \xi^{\tilde{u}}\partial_{\tilde{\ell}}\tilde{g}^{\tilde{A}\tilde{B}})\}|_{\mathcal{I}^+}.\end{aligned}\tag{5.36}$$

These expressions simplify for specific BMS symmetries.

For a supertranslation $\xi^{\tilde{u}} = \alpha(\tilde{x}^A)$, $f^{\tilde{A}} = 0$ and we have

$$\frac{\partial\xi^{\tilde{A}}}{\partial\tilde{\ell}}|_{\mathcal{I}^+} = [\alpha\frac{\partial\tilde{g}^{\tilde{u}\tilde{A}}}{\partial\tilde{u}} - \alpha^{:\tilde{A}}]|_{\mathcal{I}^+},\tag{5.37}$$

with the result that

$$\mathcal{X} = \alpha\partial_{\tilde{u}}h - \frac{1}{2}Q_{\tilde{A}}Q_{\tilde{B}}\alpha^{:\tilde{A}\tilde{B}}.\tag{5.38}$$

For the translations, for which $\alpha(\tilde{x}^A)$ is an $\ell = 0$ or $\ell = 1$ spherical harmonic, $Q^{\tilde{A}}Q^{\tilde{B}}\alpha_{:\tilde{A}\tilde{B}} = 0$. Since $\partial_{\tilde{u}}h = N$, we have

$$\mathcal{X} = \alpha N.\tag{5.39}$$

For the rotations, $\alpha = 0$ and $f^{\tilde{A}} = \epsilon^{\tilde{A}\tilde{B}}\Phi_{:\tilde{B}}$, where Φ is an $\ell = 1$ harmonic satisfying $\Phi^{:\tilde{A}}{}_{:\tilde{A}} = -2\Phi$ with $\epsilon^{\tilde{A}\tilde{B}} = iQ^{[\tilde{A}}Q^{\tilde{B}]}$, $\epsilon^{\tilde{A}\tilde{C}}\epsilon_{\tilde{B}\tilde{C}} = \delta_{\tilde{B}}^{\tilde{A}}$. As a result, $f^{\tilde{A}:\tilde{B}} =$

$-\Phi\epsilon^{\tilde{A}\tilde{B}}$, and

$$\partial_{\tilde{t}}\xi^{\tilde{A}}|_{\mathcal{S}^+} = \{-g^{\tilde{u}\tilde{B}}f^{\tilde{A}}{}_{:\tilde{B}} + f^{\tilde{B}}g^{\tilde{u}\tilde{A}}{}_{:\tilde{B}}\}|_{\mathcal{S}^+}. \quad (5.40)$$

We define a strain tensor according to

$$h^{\tilde{A}\tilde{B}} = \frac{1}{4} \left\{ -\partial_{\tilde{t}}\tilde{g}^{\tilde{A}\tilde{B}} + 2\tilde{g}^{\tilde{A}\tilde{u}}\partial_{\tilde{u}}\tilde{g}^{\tilde{u}\tilde{B}} + 2\tilde{g}^{\tilde{u}(\tilde{A}:\tilde{B})} \right\}|_{\mathcal{S}^+}, \quad (5.41)$$

so that $Q_{\tilde{A}}Q_{\tilde{B}}h^{AB} = h$. Then a straightforward calculation gives

$$\begin{aligned} \mathcal{X} = & -2i\Phi h + Q_{\tilde{A}}Q_{\tilde{B}}h^{\tilde{A}\tilde{B}}{}_{:\tilde{C}}f^{\tilde{C}} \\ & + Q_{\tilde{A}}Q_{\tilde{B}}\{f^{\tilde{C}}g^{\tilde{B}\tilde{u}}{}_{:\tilde{C}}{}^{\tilde{A}} - f^{\tilde{C}}g^{\tilde{B}\tilde{u}:\tilde{A}}{}_{:\tilde{C}} + g^{\tilde{A}\tilde{u}}f^{\tilde{B}}\}|_{\mathcal{S}^+}. \end{aligned} \quad (5.42)$$

But the second line vanishes due to the identity

$$V_{B:CA} - V_{B:AC} = Q_{AB}V_C - Q_{BC}V_A, \quad (5.43)$$

for the commutator of covariant derivatives with respect to the unit sphere metric Q_{AB} . Thus, for a rotation,

$$\mathcal{X} = -2i\Phi h + Q_{\tilde{A}}Q_{\tilde{B}}h^{\tilde{A}\tilde{B}}{}_{:\tilde{C}}f^{\tilde{C}}. \quad (5.44)$$

For the boosts, $\alpha = 0$, $f^{\tilde{A}} = \Gamma^{\tilde{A}}$, where $\Gamma^{\tilde{A}\tilde{B}} = -\Gamma Q^{\tilde{A}\tilde{B}}$, $\Gamma^{\tilde{A}}{}_{:\tilde{A}} = -2\Gamma$, $\xi^{\tilde{u}} = -u\Gamma$ and

$$\partial_{\tilde{t}}\xi^{\tilde{A}}|_{\mathcal{S}^+} = \{-\tilde{u}\Gamma\partial_{\tilde{u}}g^{\tilde{u}\tilde{A}} + \Gamma^{\tilde{B}}g^{\tilde{u}\tilde{A}}{}_{:\tilde{B}} + \tilde{u}\Gamma^{\tilde{A}}\}|_{\mathcal{S}^+}. \quad (5.45)$$

Then by the analogous calculation leading to (5.44)

$$\mathcal{X} = -\Gamma\partial_{\tilde{u}}(\tilde{u}h) + Q_{\tilde{A}}Q_{\tilde{B}}h^{\tilde{A}\tilde{B}}{}_{:\tilde{C}}\Gamma^{\tilde{C}}. \quad (5.46)$$

6. Results

Our results are based upon the same generic precessing binary black hole run taken from Taylor *et al.* [45], which was also used in [21] to calibrate the SpEC characteristic

code and in [22] to compare waveform extraction using the `SpEC` and Pitt null codes using the gauge invariant version of the of the news function computed in computational coordinates. The physical parameters are mass ratio $q = 3$, black hole dimensionless spins $\chi_1 = (0.7, 0, 0.7)/\sqrt{2}$ and $\chi_2 = (-0.3, 0, 0.3)/\sqrt{2}$, number of orbits 26, total time $T = 7509M$, initial eccentricity 10^{-3} , initial frequency $\omega_{ini} = 0.032/M$ and extraction radius $R = 100M$, where M is the total mass of the black holes.

Extraction was carried out at the three different resolutions elaborated in Table 1 to assess convergence.

| Run | Low | Med | High |
|--------------|-----|----------|------|
| N_r | 10 | 12 | 14 |
| L | 12 | 14 | 17 |
| $\Delta t/M$ | 1.0 | 0.666... | 0.5 |

Table 1: Resolution parameters used for code convergence comparisons, with time steps Δt . N_r represents the radial grid sizes. The `SpEC` code has $2L^2$ total angular grid points.

6.1. Verification of strain, news, and radiative Weyl component Ψ

Here we show that the news function computed using the inertial coordinate algorithm (inertial news) agrees with the gauge independent news (gauge-free news) computed in [22] using the computational coordinates. We also show that strain and Ψ (corresponding to the Newman-Penrose component $\bar{\psi}_4^0$) are consistent with the computation of the news function.

Comparison of the relative error E_{rel} between dataset A and dataset B is computed according to

$$E_{rel} = \log_{10} \left(\frac{|A - B|}{|B|} \right), \quad (6.1)$$

where in the convergence tests B is the highest resolution dataset. For the strain, news function and radiative Weyl component Ψ , the real parts of the $(\ell, m) = (2, 2)$ spherical harmonic modes are compared.

Spatial convergence is at an exponential rate expected of a spectral code, while time convergence is 4^{th} order. The convergence test shows which error source dominates the simulation. Given an increase in resolution by some constant factor, spectral convergence results in reducing the error by a constant factor on a log scale. In contrast, high-order polynomial convergence such as $E \propto \Delta t^4$ will yield logarithmic convergence on a log scale under the same increase in resolution. For these simulations, 4^{th} order time convergent error dominates over the spatial spectral error.

In Fig. 3, we computed the news function in two different ways at the three different resolutions outlined in Table 1, for a total of six datasets. The inertial news (computed directly in the inertial coordinate system) is compared with the high resolution results for the gauge-free news (computed first in the computational coordinates, as in [22]). Both versions of the news agree and display 4^{th} order convergence.

Similarly, we computed the error in the strain by comparing adjacent resolutions. The strain remains convergent over the entire run, as shown in Fig. 4. With only a 20% increase in resolution, the error in the medium resolution run decreases by 85%, consistent with the underlying spatial spectral method and the 4^{th} order time integrator.

The higher time derivatives in Ψ make it more sensitive to the numerical noise produced by the junk radiation in the initial phase of the run. After this initial period, the error in Ψ displays the same rate of convergence as the news and strain,

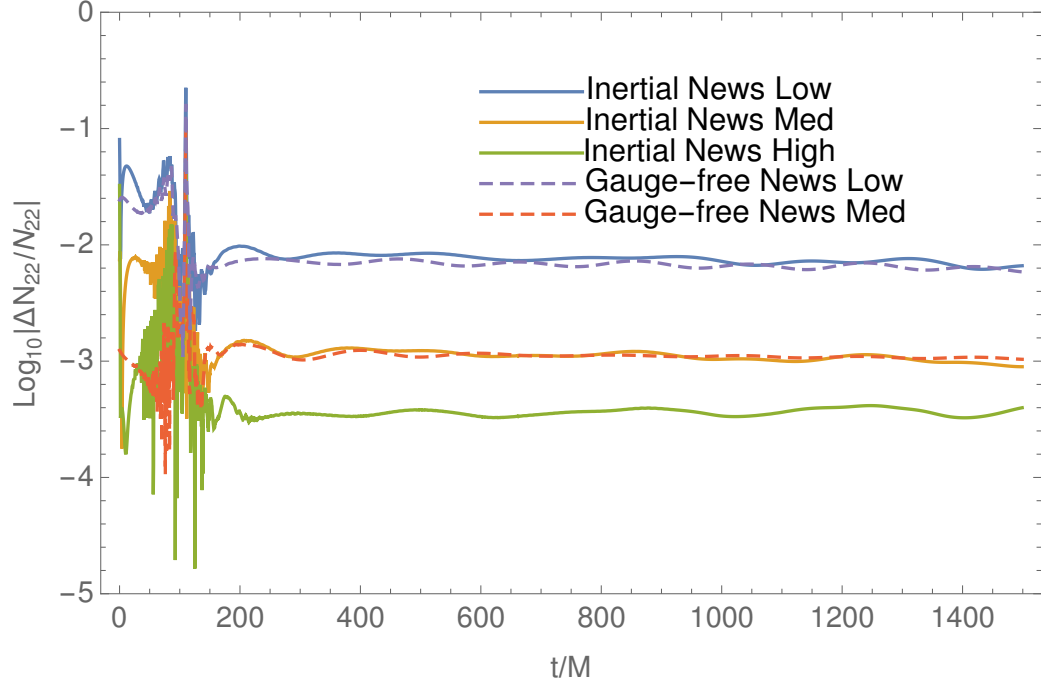


Figure 3: 4^{th} order convergence of the news function computed two different ways. Solid lines are the error in the new, inertial coordinates computation. Dashed lines are error in the gauge-free news computed in computational coordinates. Here, error is computed with reference to the highest resolution grid, showing both self convergence *and* agreement between the two methods.

as shown in Fig. 5.

Finally, we verify the inertial frame relationships $\Psi = N_{,\tilde{u}} = h_{,\tilde{u}\tilde{u}}$. Computed in the highest resolution inertial domain, these quantities agree, as shown in Fig. 6.

6.2. Flux

In the inertial frame at \mathcal{I}^+ , the asymptotic Killing vectors which generate the BMS group have the form (4.1), i.e.

$$\xi^{\tilde{\rho}}\partial_{\tilde{\rho}}|_{\mathcal{I}^+} = \left(\alpha(\tilde{x}^A) + \frac{1}{2}\tilde{u}f_{,\tilde{A}}^{\tilde{A}} \right) \partial_{\tilde{u}} + f^{\tilde{A}}\partial_{\tilde{A}}, \quad (6.2)$$

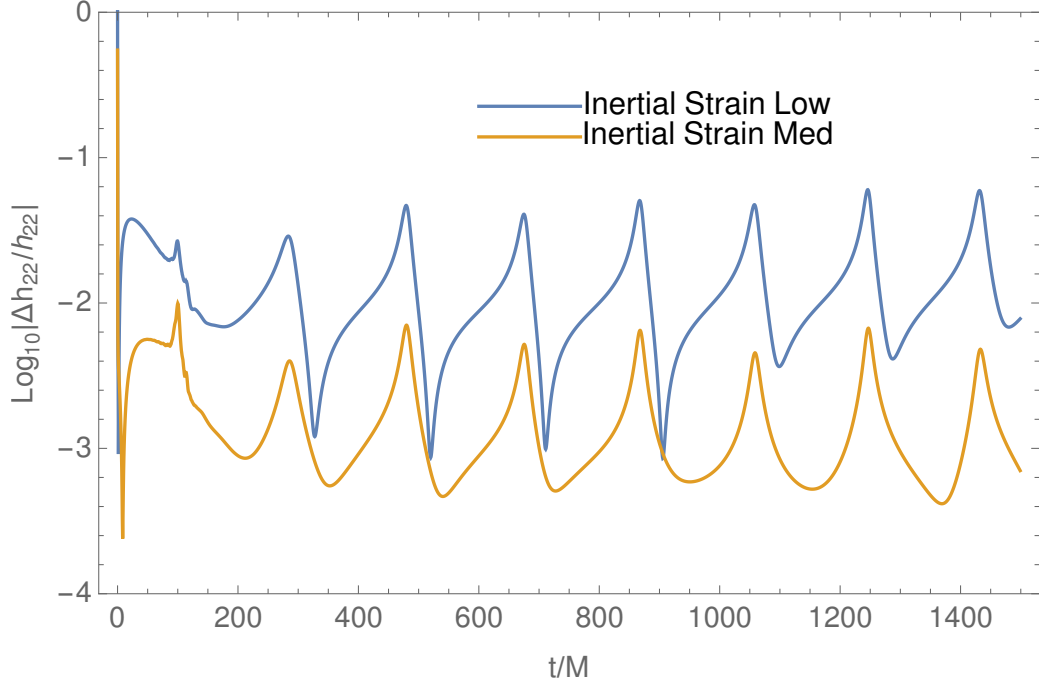


Figure 4: Here, we compare error in the low and medium resolution calculations of the strain computed in the inertial coordinates (inertial strain) by comparing them to the medium and high resolution runs, respectively. Comparison between the errors in the medium and low resolution runs is consistent with the 4th order convergence arising from the time integrator.

where $f^{\tilde{A}}(\tilde{x}^B)$ is a conformal killing vector for the unit sphere metric. Here we consider the fluxes corresponding to the BMS generators for the time translation T_u , the three spatial translations (T_x, T_y, T_z) , the three rotations (R_x, R_y, R_z) , and the three boosts (B_x, B_y, B_z) , with respect to the corresponding axes of the asymptotic inertial frame, as well as a sample supertranslation (ST), totaling 11 asymptotic symmetries.

We compute the energy flux by calculating the absolute square $|N|^2$ of the news function. For the remaining flux calculations, we first use (5.34) to compute the flux rate of change and then carry out a retarded inertial time integral. As a result, the numerical noise in Ψ during the initial phase of junk radiation (see Fig. 5) introduces some non-convergent error. Consequently, although the plots of the time dependence

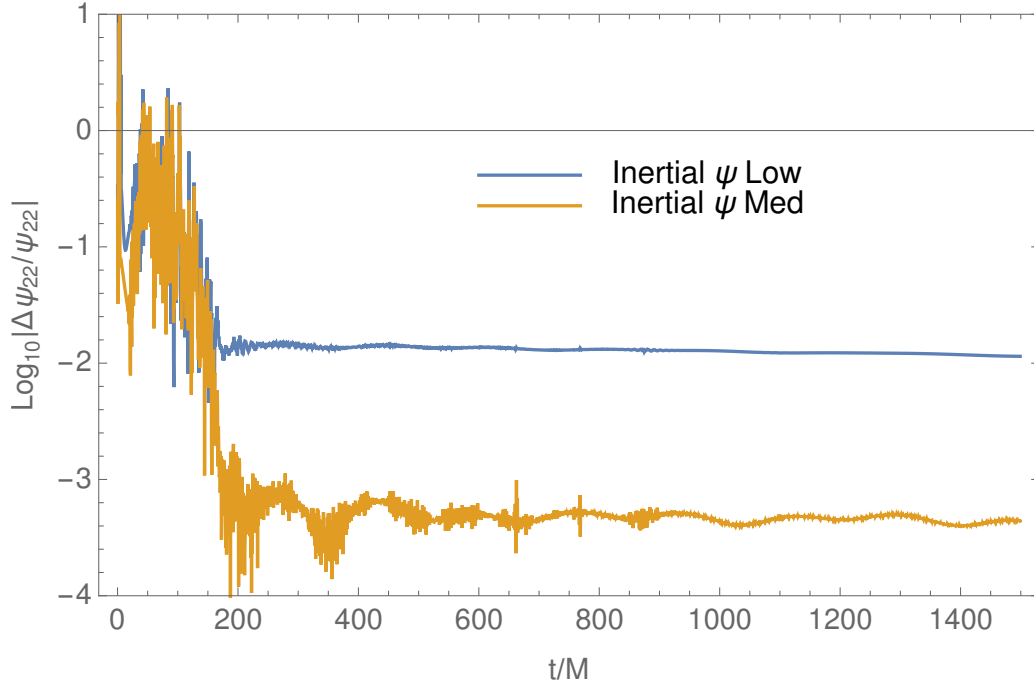


Figure 5: The errors in the inertial coordinate computation of Ψ for low and medium resolution runs are compared with the medium and high resolution runs, respectively. The results confirm 4^{th} order convergence following the initial phase of junk radiation.

of the fluxes show good agreement for the three resolutions, convergence of the error is not as clean as for the energy flux computed directly from the news function. Therefore, for the purpose of convergence studies, we concentrate on the error in the retarded time derivative of the flux, although both rates of convergence are shown for completeness.

In all cases, we plot the waveform and convergence of the strongest mode. Part (a) of each plot is a spherical representation of the functional form of the corresponding BMS generator. Spatial components are shown with vector arrows, while the time component is demarcated with a color gradient.

6.2.1. Energy and momentum flux The time translation is described by the BMS generator $\xi_{[Tu]}^\alpha$ with components $\alpha_{Tu} = 1$, $f^A = 0$, corresponding to an $\ell = 0$ spherical

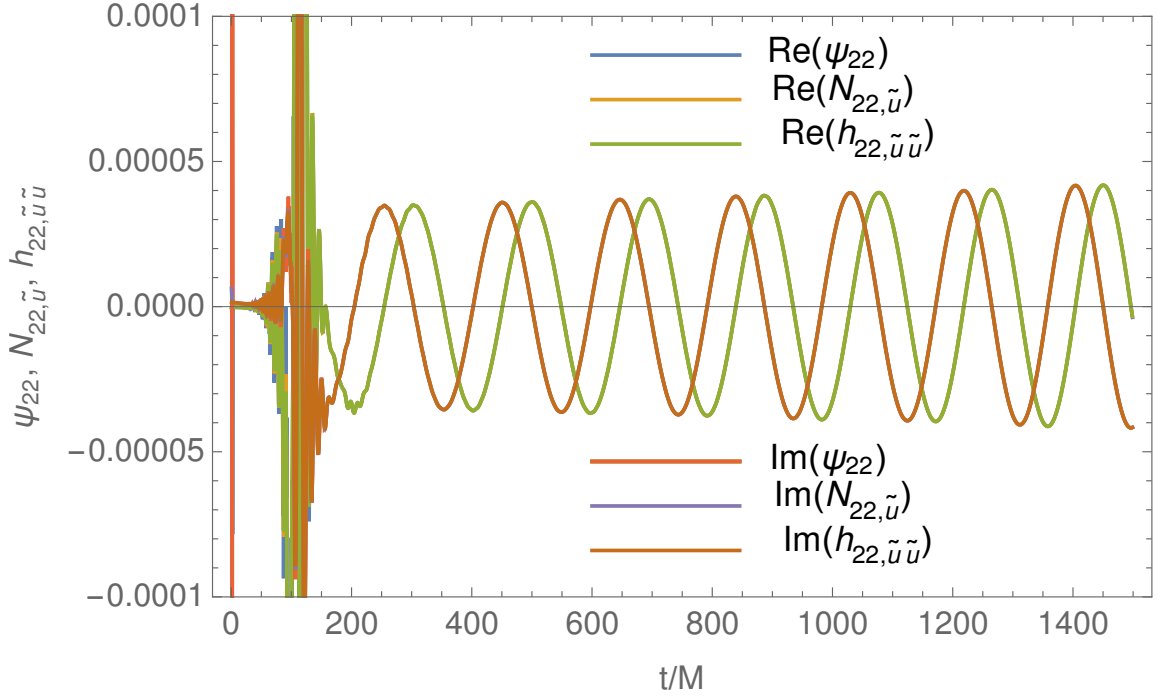


Figure 6: Comparison of $\Psi = N_{,\tilde{u}} = h_{,\tilde{u}\tilde{u}}$ (real and imaginary parts). Following the initial phase of junk radiation, the data overlap completely, hiding Ψ and $N_{,\tilde{u}}$ behind $h_{,\tilde{u}\tilde{u}}$.

harmonic. Figure 7 shows the form of the generator (7a), its associated flux (7b), the flux convergence (7c) and the stronger convergence of the inertial time derivative of the flux (7d).

The three momentum fluxes are derived from the three spatial translations, described by the BMS generators $\xi_{[Tx]}^\alpha$, $\xi_{[Ty]}^\alpha$ and $\xi_{[Tz]}^\alpha$, with $f^A = 0$ and α constructed from $l = 1$ spherical harmonics,

$$\alpha_{[Tx]} = \sin \tilde{\theta} \cos \tilde{\phi}, \quad \alpha_{[Ty]} = \sin \tilde{\theta} \sin \tilde{\phi}, \quad \alpha_{[Tz]} = \cos \tilde{\theta}, \quad (6.3)$$

corresponding to the axes of the asymptotic inertial frame. The corresponding momentum fluxes F_{Tx} , F_{Ty} and F_{Tz} can also be obtained directly from the energy flux by weighting it with the corresponding $l = 1$ harmonics,

$$F_{Tx} = \sin \tilde{\theta} \cos \tilde{\phi} |N|^2, \quad F_{Ty} = \sin \tilde{\theta} \sin \tilde{\phi} |N|^2, \quad F_{Tz} = \cos \tilde{\theta} |N|^2, \quad (6.4)$$

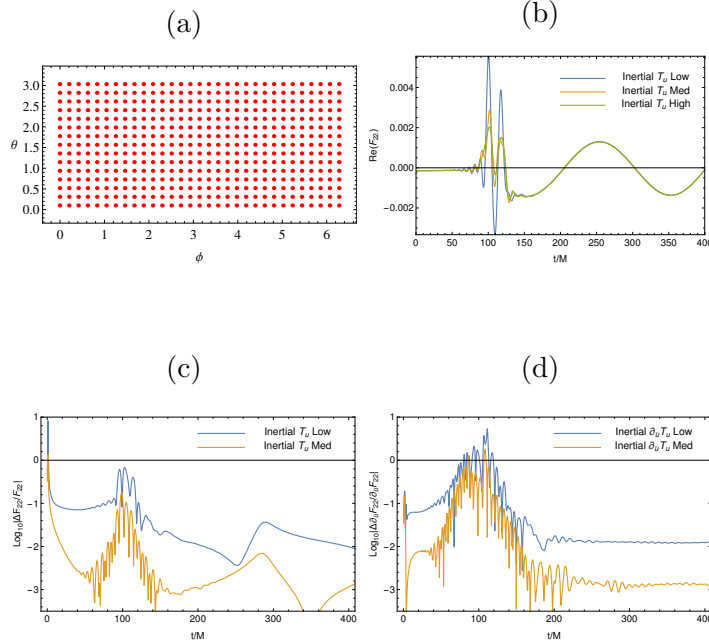


Figure 7: (7a) The \tilde{u} component of $\xi_{Tu} = 1$ is uniform everywhere on the sphere and has no angular component. (7b) The $(\ell = 2, m = 2)$ spherical harmonic component of the flux, $F_{Tu} = |N|^2$. (7c) Convergence of the flux is partially compromised by junk radiation, while the inertial time derivative of the flux (7d) shows the appropriate 4^{th} order convergence following the junk phase.

in which case the clean 4^{th} order convergence obtained for the energy flux $|N|^2$ would also result following the initial period of junk radiation.

Alternatively, these momentum ξ fluxes can be obtained by a retarded time integral, e.g. $F_{Tz} = \int \dot{F}_{Tz} du$. However, although the strain and energy flux both have dominant components in the $(\ell = 2, m = 2)$ mode, the nonlinear effect of multiplication by an $\ell = 1$ harmonic shifts the momentum fluxes into other modes. For this reason, we plot the $(\ell = 3, m = 2)$ mode.

The z -component of momentum flux F_{Tz} obtained this way is shown in Fig. 8b. Convergence of the flux is shown in Fig. 8c and its inertial time derivative in Fig. 8d.

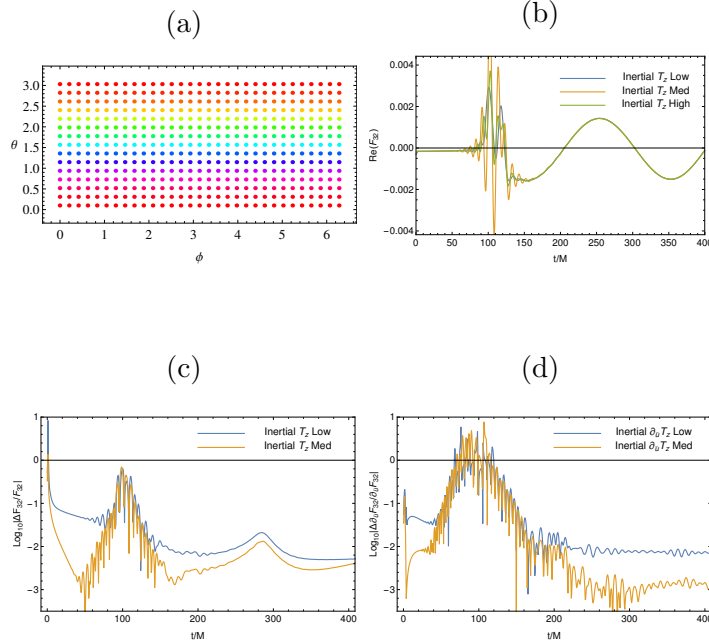


Figure 8: (8a) The \tilde{u} component of ξ_{Tz} shifts from pole to pole, illustrating a translation in the z -direction. (8b) The $(\ell = 3, m = 2)$ spherical harmonic component of the flux. (8c) Convergence of the flux is partially compromised by junk radiation, while the inertial time derivative of the flux (8d) shows the appropriate 4^{th} order convergence following the junk phase.

The $(\ell = 3, m = 3)$ mode of the x -component of the momentum flux F_{Tx} is shown in Fig. 9b. Convergence of the flux is shown in Fig. 9c and its inertial time derivative in Fig. 9d.

Similarly, the $(\ell = 3, m = 3)$ mode of the y -component of the momentum flux F_{Ty} is shown in Fig. 10b. Convergence of the flux is shown in Fig. 10c and its inertial time derivative in Fig. 10d.

6.2.2. Rotations The three spatial rotations with respect to the inertial axes are described by the BMS generators $\xi_{[Rx]}^\alpha$, $\xi_{[Ry]}^\alpha$ and $\xi_{[Rz]}^\alpha$ with $\alpha = 0$ and $f^{\tilde{A}} = \epsilon^{\tilde{A}\tilde{B}}\Phi_{;\tilde{B}}$,

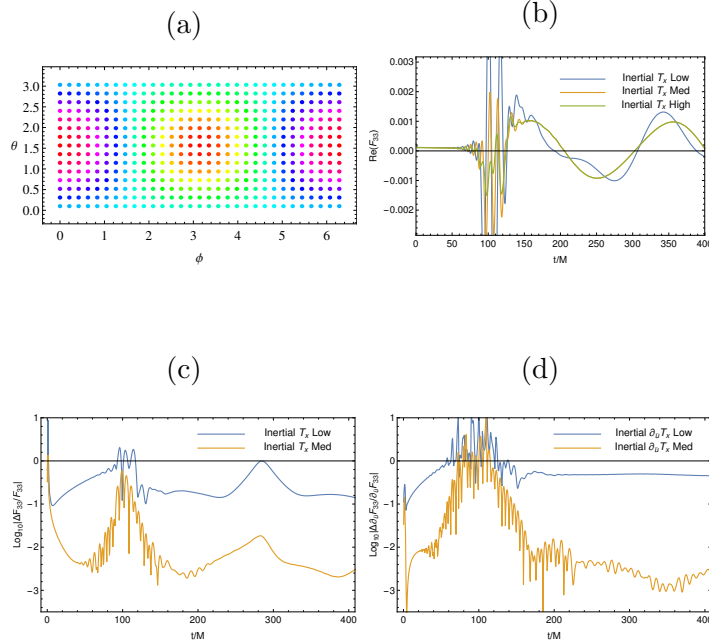


Figure 9: (9a) The \tilde{u} component of ξ_{Tx} shifts with ϕ , showing a translation in the x ($\phi = 0$) direction. (9b) The $(\ell = 3, m = 3)$ spherical harmonic component of the flux. (9c) Convergence of the flux is partially compromised by junk radiation, while the inertial time derivative of the flux (9d) shows the appropriate 4^{th} order convergence following the junk phase.

where Φ is constructed from $\ell = 1$ spherical harmonics. A rotation R_z about the z -axis corresponds to the spherical harmonic $\Phi = \cos \tilde{\theta}$, so that $f^{\tilde{A}} = (0, 1)$. Most of the motion of the orbiting black holes is about this axis, so we expect to see a greater flux of the corresponding z -component of angular momentum F_{Rz} . The $(\ell = 2, m = 2)$ mode of the z component of the angular momentum flux F_{Rz} is shown in Fig. 11b. Convergence of the flux is shown in Fig. 11c and its inertial time derivative in Fig. 11d.

A rotation R_x about the x -axis corresponds to the spherical harmonic $\Phi = \sin \tilde{\theta} \cos \tilde{\phi}$ so that $f^{\tilde{A}} = (-\sin \tilde{\phi}, -\cot \tilde{\theta} \cos \tilde{\phi})$. Similarly, a rotation R_y about the y -axis corresponds to the spherical harmonic $\Phi = \sin \tilde{\theta} \sin \tilde{\phi}$ so that $f^{\tilde{A}} =$

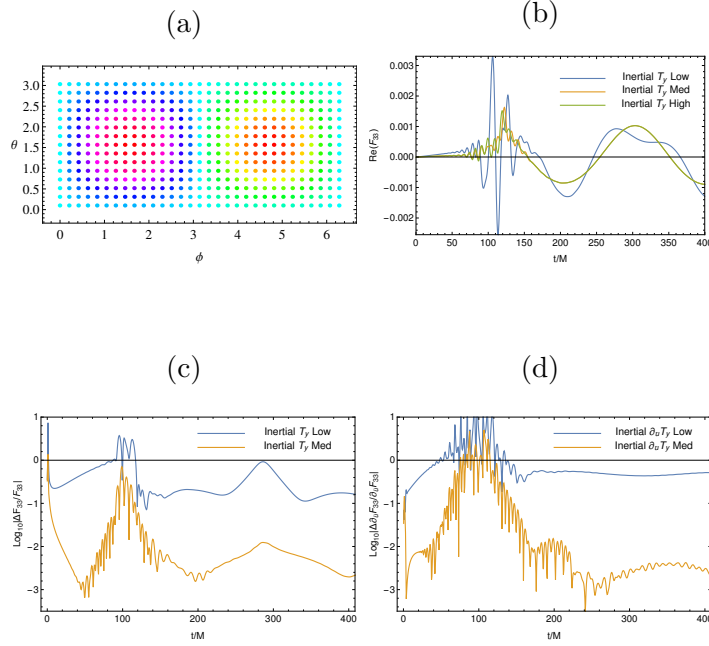


Figure 10: (10a) The \tilde{u} component of ξ_{Ty} shifts with ϕ , showing a translation in the y ($\phi = \pi/2$) direction. (10b) The $(\ell = 3, m = 3)$ spherical harmonic component of the flux. (10c) Convergence of the flux is partially compromised by junk radiation, while the inertial time derivative of the flux (10d) shows the appropriate 4^{th} order convergence following the junk phase.

$$(\cos \tilde{\phi}, -\cot \tilde{\theta} \sin \tilde{\phi}).$$

The $(\ell = 2, m = 1)$ modes of the x and y -components of the angular momentum flux, F_{Rx} and F_{Ry} , are shown in Fig. 12b and Fig. 13b, respectively. Convergence of these fluxes is shown in Fig. 12c and Fig. 13c; and convergence of their inertial time derivative in Fig. 12d and Fig. 13d.

6.2.3. Boosts In addition to the rotations, the other transformations of the Lorentz group are the three boosts with BMS generators $\xi_{[Bx]}^\alpha$, $\xi_{[By]}^\alpha$ and $\xi_{[Bz]}^\alpha$ for which $f_{:\tilde{A}}^{\tilde{A}} \neq 0$. For these boost generators, $\alpha = 0$, $f^{\tilde{A}} = \Gamma^{:\tilde{A}}$, where Γ consists of $\ell = 1$ spherical

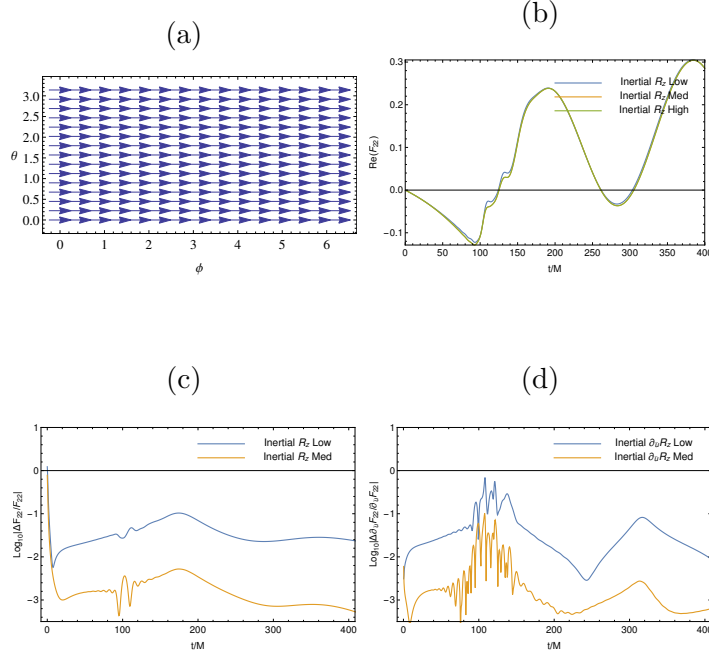


Figure 11: (11a) Vectors illustrate the nature of ξ_{Rz} , a rotation about z . (11b) The $(\ell = 2, m = 2)$ spherical harmonic component of the flux. (11c) Convergence of the flux is partially compromised by junk radiation, while the inertial time derivative of the flux (11d) shows the appropriate 4^{th} order convergence following the junk phase.

harmonics, so that $\Gamma^{\cdot\tilde{A}}{}_{\cdot\tilde{A}} = -2\Gamma$ and $\xi^{\tilde{u}} = -u\Gamma$. As a result, the boosts acquire a $\xi^{\tilde{u}}$ component with linear dependence on \tilde{u} , as well as $\ell = 1$ angular dependence. The corresponding physical quantities describe the dipole moment of the system corresponding to the center-of-mass integrals in Lorentz covariant theories.

For a boost B_z in the inertial z -direction, $\Gamma = \cos \tilde{\theta}$ so that $f^{\tilde{A}} = (-\sin \tilde{\theta}, 0)$ and $\xi^{\tilde{u}}_{[Bz]} = -\tilde{u} \cos \tilde{\theta}$. The $(\ell = 3, m = 0)$ mode of the z -component of the boost flux F_{Bz} is shown in Fig. 14b. Convergence of the flux is shown in Fig. 14c and its inertial time derivative in Fig. 14d.

For a boost B_x in the inertial x -direction, $\Gamma = \sin \tilde{\theta} \cos \tilde{\phi}$ so that $f^{\tilde{A}} = (\cos \tilde{\theta} \cos \tilde{\phi}, -\csc \tilde{\theta} \sin \tilde{\phi})$. Similarly, for a boost B_y in the inertial y -direction, $\Gamma =$

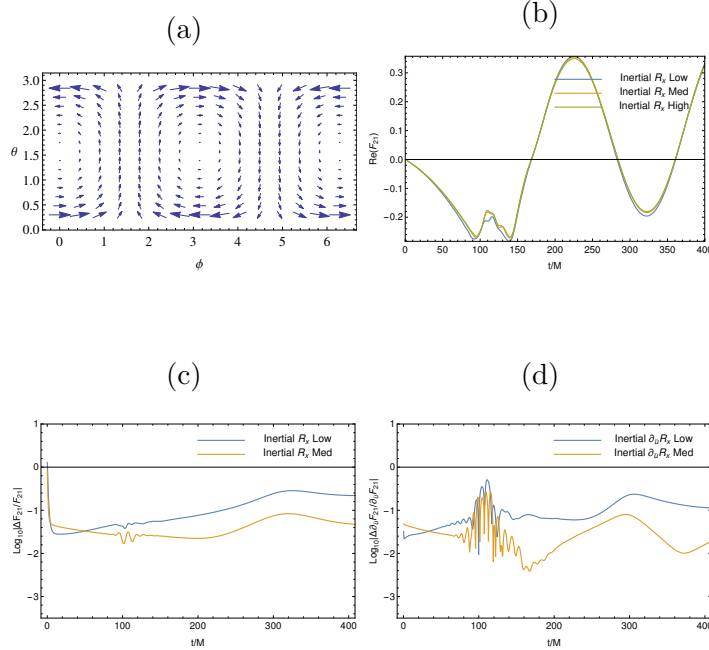


Figure 12: (12a) Vectors illustrate the nature of ξ_{Rx} , a rotation about the x -axis ($\phi = 0$). (12b) The $(\ell = 2, m = 1)$ spherical harmonic component of the flux. (12c) Convergence of the flux is partially compromised by junk radiation, while the inertial time derivative of the flux (12d) shows the appropriate 4th order convergence following the junk phase.

$\sin \tilde{\theta} \sin \tilde{\phi}$ so that $f^{\tilde{A}} = (\cos \tilde{\theta} \sin \tilde{\phi}, \csc \tilde{\theta} \cos \tilde{\phi})$. The $(\ell = 3, m = 3)$ mode of the x and y -components of the boost flux, F_{Bx} and F_{By} , is shown in Fig. 15b and Fig. 16b, respectively. Convergence of these fluxes is shown in Fig. 15c and Fig. 16c; and convergence of their inertial time derivative in Fig. 15d and Fig. 16d.

6.2.4. Supertranslations The BMS supertranslation generators $\xi_{[ST]}^{\tilde{\alpha}}$ are described by $f^{\tilde{A}} = 0$, with $\alpha(\tilde{x}^B)$ constructed from spherical harmonics with $l > 1$. This leads to an infinite set of transformations, which extend well beyond the limit of code resolution. Here we concentrate on the supertranslation corresponding to a $|Y_{22}|$ spherical harmonic, $\alpha_{ST} = \sin^2 \tilde{\theta} \cos 2\tilde{\phi}$.

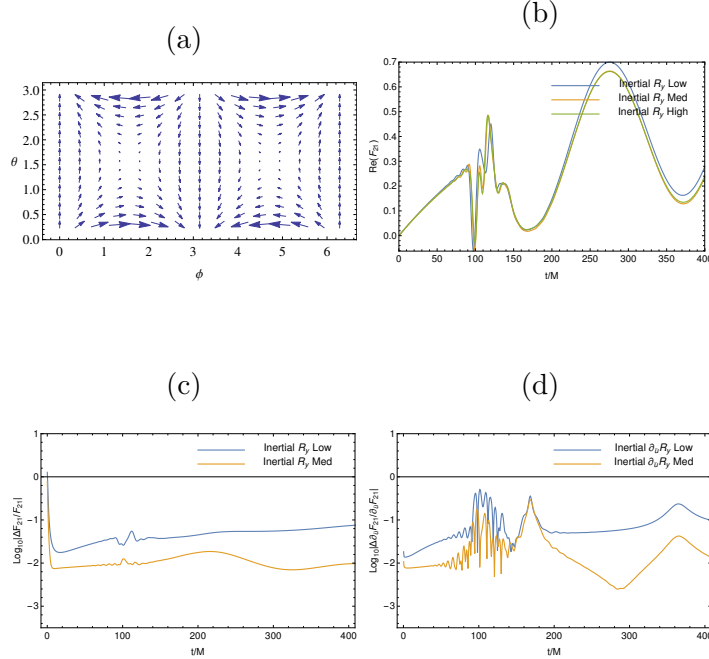


Figure 13: (13a) Vectors illustrate the nature of ξ_{Ry} , a rotation about y ($\phi = \pi/2$). (13b) The $(\ell = 2, m = 1)$ spherical harmonic component of the flux. (13c) Convergence of the flux is partially compromised by junk radiation, while the inertial time derivative of the flux (13d) shows the appropriate 4^{th} order convergence following the junk phase.

The $(\ell = 2, m = 2)$ mode of the $|Y_{22}|$ -derived supertranslation flux F_{ST} is shown in Fig. 17b. Convergence of the flux is shown in Fig. 17c and its inertial time derivative in Fig. 17d.

7. Conclusion

In the context of Cauchy-characteristic evolution, we have developed the mathematical formalism for computing the gravitational radiation fluxes to \mathcal{I}^+ of energy-momentum, angular-momentum-dipole-moment and supermomentum, associated with the asymptotic symmetries of the BMS group. We have implemented

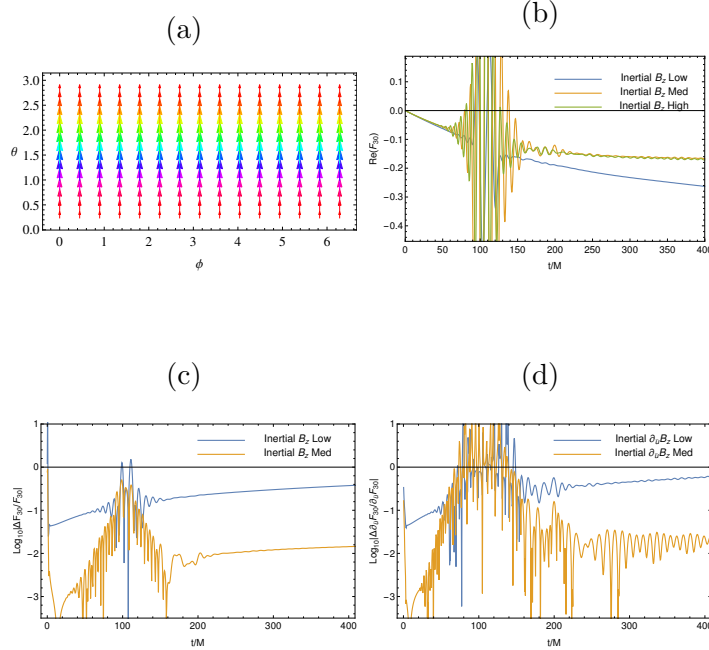


Figure 14: (14a) Vectors illustrate the nature of $\xi_{Bz}^{\tilde{A}}$, while colors illustrate the gradient of $\xi_{Bz}^{\tilde{u}}$, illustrating a Lorentz boost Bz in the z -direction. (14b) The $(\ell = 3, m = 0)$ spherical harmonic component of the flux. (14c) Convergence of the flux is partially compromised by junk radiation, while the inertial time derivative of the flux (14d) shows the appropriate 4^{th} order convergence following the junk phase.

this algorithm as part of the Spectral Einstein Code (SpEC). The resulting code supplies a uniform computation of the radiation strain, news function, Newman-Penrose radiative ψ_4^0 curvature component and BMS fluxes in terms of inertial coordinates at \mathcal{I}^+ . It is a stable, convergent, and highly efficient code for determining all the physical attributes of the gravitational radiation field.

Convergence tests were carried out based upon the simulation of a generic precessing binary black hole. These tests showed that the numerical accuracy was limited by the 4^{th} order time integrator, as opposed to the exponential convergence rate expected of the spatial spectral code. The main source of error arose from the

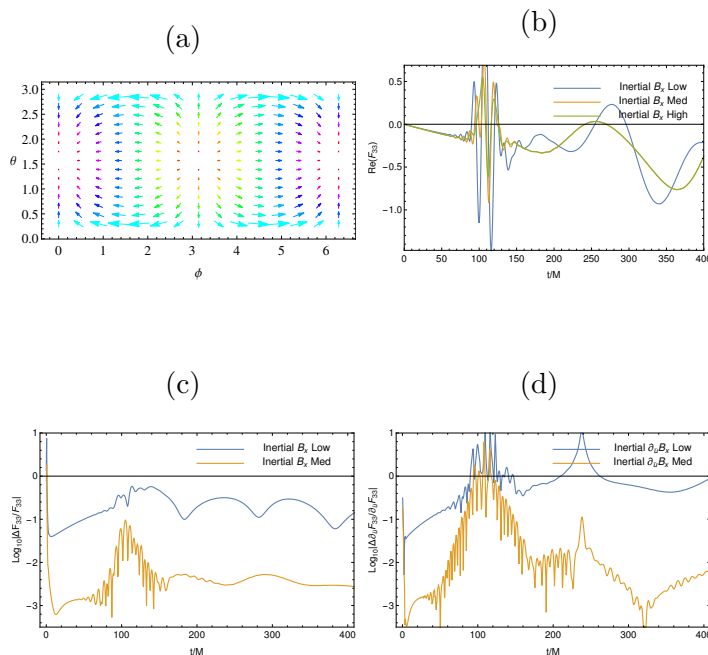


Figure 15: (15a) Vectors illustrate the nature of $\xi_{Bx}^{\tilde{A}}$, while colors illustrate the gradient of $\xi_{Bx}^{\tilde{A}}$, illustrating a boost in the x ($\phi = 0$) direction. (15b) The $(\ell = 3, m = 3)$ spherical harmonic component of the flux. (15c) Convergence of the flux is partially compromised by junk radiation, while the inertial time derivative of the flux (15d) shows the appropriate 4^{th} order convergence following the junk phase.

artificial junk radiation introduced by the binary black hole initial data.

The accuracy for radiation strain, news function N and ψ_4^0 were comparable to computations using a prior version of the SpEC characteristic code. The same was also found for the computation of energy-momentum flux, which is determined by the $\ell = 0$ and $\ell = 1$ components of $|N|^2$.

The computation of the angular momentum and supermomentum fluxes is more complicated than the energy-momentum flux. In addition, there are ambiguities in their underlying construction, which we base here upon the linkage integrals. However, these ambiguities are not as serious in the case of the retarded time

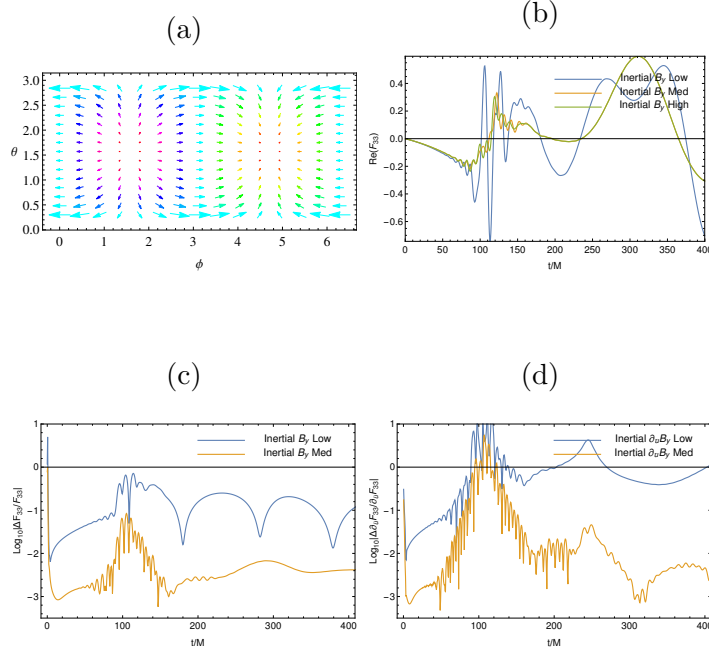


Figure 16: (16a) Vectors illustrate the nature of $\xi_{By}^{\tilde{A}}$, while colors illustrate the gradient of $\xi_{By}^{\tilde{u}}$, illustrating a boost in the y ($\phi = \pi/2$) direction. (16b) The ($\ell = 3, m = 3$) spherical harmonic component of the flux. (16c) Convergence of the flux is partially compromised by junk radiation, while the inertial time derivative of the flux (16d) shows the appropriate 4^{th} order convergence following the junk phase.

derivatives of the linkage flux \dot{F}_{ξ} , which only depend upon a product of ψ_4^0 with the choice of BMS generator, according to (5.34). An idealized strategy for studying, say, angular momentum would be to base its initial value either on the Wald-Zoupas Hamiltonian approach [34] in the infinite past retarded time $u \rightarrow -\infty$ or on its unambiguous definition at spatial infinity, where the initial flux should vanish. The dynamical properties of angular momentum can then be studied by retarded time integrals of \dot{F}_{ξ} . However, in practice this strategy would require binary black hole data devoid of junk radiation, which is not true at least for the generic precessing system simulated here. Following the the initial phase of junk radiation, tests of \dot{F}_{ξ}

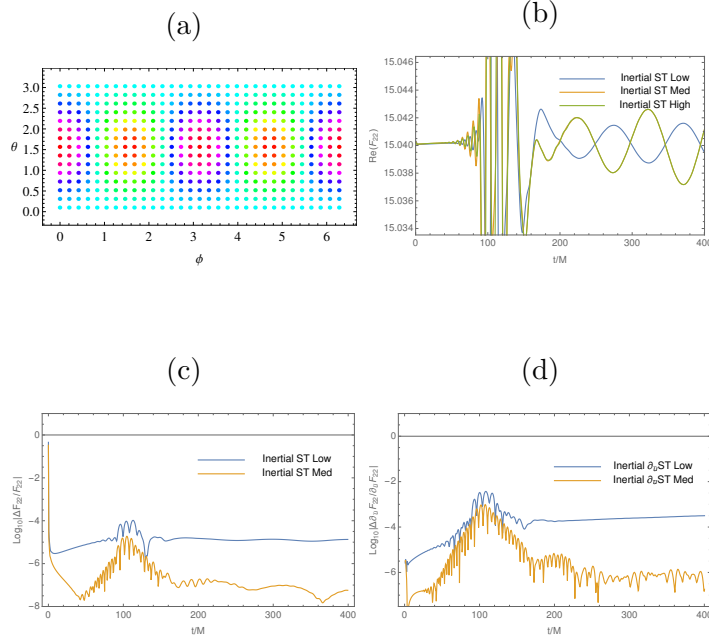


Figure 17: (17a) A color gradient illustrates the nature of ξ_{ST}^u , a $|Y_{22}|$ supertranslation. (17b) The $(\ell = 2, m = 2)$ spherical harmonic component of the flux. (17c) Convergence of the flux is partially compromised by junk radiation, while the inertial time derivative of the flux (17d) shows the appropriate 4^{th} order convergence following the junk phase.

showed clear 4^{th} order convergence. However, the high derivatives involved in the calculation of \dot{F}_ξ magnify the effect of the junk radiation.

These considerations add to other important reasons to develop methods for obtaining binary black hole data which suppress junk radiation. In particular, this would allow application of our code to study the interesting question of how a supertranslation shift between the preferred Poincaré groups at $u = \pm\infty$ might affect angular momentum loss.

Acknowledgments

We thank Nicholas Taylor for his generic precessing binary black hole run that we used to test and baseline code performance. We thank Mark Scheel, Yanbei Chen, and Christian Reisswig for their advice, support, and technical expertise. This research used the Spectral Einstein Code (SpEC)[46]. The Caltech cluster `zwickycacr.caltech.edu` is an essential resource for SpEC related research, supported by the Sherman Fairchild Foundation and by NSF award PHY-0960291. This research also used the Extreme Science and Engineering Discovery Environment (XSEDE) under grant TG-PHY990002. The UCSD cluster `ccom-boom.ucsd.edu` was used during code development. This project was supported by the Sherman Fairchild Foundation, and by NSF Grants PHY-1068881, AST-1333520, and CAREER Grant PHY-0956189 at Caltech. JW’s research was supported by NSF grant PHY-1505965 to the University of Pittsburgh.

References

- [1] B. P. A. et al. (LIGO Scientific Collaboration and V. Collaboration), “Observation of gravitational waves from a binary black hole merger,” *Phy. Rev. Lett.* **116** (2016) 061102.
- [2] S. J. Waldman, “The advanced ligo gravitational wave detector,” Tech. Rep. LIGO-P0900115-v2, LIGO Project, 2011.
- [3] T. Accadia, F. Acernese, F. Antonucci, P. Astone, G. Ballardin, *et al.*, “Plans for the upgrade of the gravitational wave detector VIRGO: Advanced VIRGO,” in *Proceedings of the Twelfth Marcel Grossmann Meeting on General Relativity*, T. Damour, R. T. Jantzen, and R. Ruffini, eds., pp. 1738–1742. 2009.
- [4] **LIGO Scientific Collaboration** Collaboration, H. Grote, “The GEO 600 status,” *Class. Quantum Grav.* **27** (2010) 084003.
- [5] K. Somiya and the KAGRA Collaboration, “Detector configuration of KAGRA—the japanese cryogenic gravitational-wave detector,” *Class. Quantum Grav.* **29** no. 12, (2012) 124007.

- [6] W. Tichy and P. Marronetti, “Binary black hole mergers: Large kicks for generic spin orientations,” Phys. Rev. D **76** (2007) 061502(R).
- [7] C. O. Lousto and Y. Zlochower, “Hangup Kicks: Still Larger Recoils by Partial Spin/Orbit Alignment of Black-Hole Binaries,” Phys. Rev. Lett. **107** (2011) 231102, [arXiv:1108.2009](https://arxiv.org/abs/1108.2009) [gr-qc].
- [8] J. A. González, U. Sperhake, B. Brügmann, M. Hannam, and S. Husa, “Maximum kick from nonspinning black-hole binary inspiral,” Phys. Rev. Lett. **98** (2007) 091101, [gr-qc/0610154](https://arxiv.org/abs/gr-qc/0610154).
- [9] M. Favata, S. A. Hughes, and D. E. Holz, “How black holes get their kicks: Gravitational radiation recoil revisited,” Astrophys. J. **607** (2004) L5–L8.
- [10] J. G. Baker, W. D. Boggs, J. Centrella, B. J. Kelly, S. T. McWilliams, M. C. Miller, and J. R. van Meter, “Modeling kicks from the merger of generic black-hole binaries,” Astrophys. J. **682** (2008) L29, [arXiv:0802.0416](https://arxiv.org/abs/0802.0416).
- [11] J. Healy, F. Herrmann, I. Hinder, D. M. Shoemaker, P. Laguna, and R. A. Matzner, “Superkicks in hyperbolic encounters of binary black holes,” Phys. Rev. Lett. **102** (2009) 041101, [arXiv:0807.3292](https://arxiv.org/abs/0807.3292) [gr-qc].
- [12] H. Bondi, M. G. J. van der Burg, and A. W. K. Metzner, “Gravitational waves in general relativity VII. Waves from axi-symmetric isolated systems,” Proc. R. Soc. Lond. A **269** (1962) 21–52.
- [13] R. K. Sachs, “Gravitational waves in general relativity. VIII. waves in asymptotically flat space-time,” Proc. R. Soc. Lond. A **270** no. 1340, (October, 1962) 103–126.
<http://www.jstor.org/stable/2416200>.
- [14] R. Penrose, “Asymptotic properties of fields and space-times,” Phys. Rev. Lett. **10** no. 2, (1963) 66–68.
- [15] J. Winicour, “Characteristic evolution and matching,” Living Rev. Rel. **15** no. 2, (2012) .
<http://www.livingreviews.org/lrr-2012-2>.
- [16] L. A. Tamburino and J. H. Winicour, “Gravitational fields in finite and conformal Bondi frames,” Phys. Rev. **150** (1966) 1039–1053.
<http://link.aps.org/doi/10.1103/PhysRev.150.1039>.
- [17] R. A. Isaacson, J. S. Welling, and J. Winicour, “Null cone computation of gravitational radiation,” J. Math. Phys. **24** (1983) 1824.
<http://iopscience.iop.org/0264-9381/30/7/075017>.

- [18] N. T. Bishop, R. Gomez, L. Lehner, M. Maharaj, and J. Winicour, “High-powered gravitational news,” Phys. Rev. **D56** (1997) 6298–6309, [arXiv:gr-qc/9708065](#).
- [19] M. C. Babiuc, N. T. Bishop, B. Szilágyi, and J. Winicour, “Strategies for the characteristic extraction of gravitational waveforms,” Phys. Rev. D **79** (2009) 084011, [arXiv:0808.0861](#).
- [20] M. C. Babiuc, B. Szilágyi, J. Winicour, and Y. Zlochower, “A characteristic extraction tool for gravitational waveforms,” Phys. Rev. D **84** (Aug, 2011) 044057, [arXiv:1011.4223 \[gr-qc\]](#). <http://link.aps.org/doi/10.1103/PhysRevD.84.044057>.
- [21] C. J. Handmer and B. Szilágyi, “Spectral characteristic evolution: A new algorithm for gravitational wave propagation,” Classical and Quantum Gravity **32** (2015) 025008, [arXiv:1406.7029](#).
- [22] C. J. Handmer, B. Szilágyi, and J. Winicour, “Gauge invariant spectral characteristic extraction,” [arXiv:1502.06987](#).
- [23] R. Geroch, Asymptotic Structure of Spacetime. Plenum, New York, 1995.
- [24] L. B. Szabados, “Quasi-local energy-momentum and angular momentum in General Relativity: A review article,” Living Rev. Rel. **12** no. 4, (2009) . <http://www.livingreviews.org/lrr-2009-4>.
- [25] A. Ashtekar and R. O. Hansen, “A unified treatment of null and spatial infinity in general relativity. i. universal structure, asymptotic symmetries, and conserved quantities at spatial infinity,” J. Math. Phys. **19** (1978) 1542–1566.
- [26] R. K. Sachs, “Asymptotic symmetries in gravitational theory,” Phys. Rev. **128** (1962) 2851–2864.
- [27] E. T. Newman and R. Penrose, “Note on the Bondi–Metzner–Sachs group,” J. Math. Phys. **7** (1966) 863–870. <http://link.aip.org/link/?JMP/7/863/1>.
- [28] J. Winicour, “Angular momentum in general relativity,” in General Relativity and Gravitation, A. Held, ed., vol. 2, pp. 71–96. Plenum Press, New York, 1980.
- [29] R. Geroch and J. Winicour, “Linkages in general relativity,” J. Math. Phys. **22** (1981) 803.
- [30] J. Winicour, “Global aspects of radiation memory,” Classical and quantum gravity **31** no. 20, (2014) 205003.
- [31] J. Winicour, “Some total invariants of asymptotically flat space-times,” J. Math. Phys. **9** no. 6, (1968) 861–867.
- [32] A. Komar, “Covariant conservation laws in general relativity,” Phys. Rev. **113** (1959) 934–936.

- [33] A. Ashtekar and M. Streubel, “Symplectic geometry of radiative modes and conserved quantities at null infinity,” Proc. R. Soc. Lond. A **376** no. 1767, (1981) 585–607.
- [34] R. Wald and A. Zoupas, “General definition of ” conserved quantities” in general relativity and other theories of gravity,” Phys. Rev. D **61** (2000) 084027.
- [35] T. Dray and M. Streubel, “Angular momentum at null infinity,” Classical and Quantum Gravity **1** no. 1, (1984) 15.
- [36] A. Ashtekar and J. Winicour, “Linkages and hamiltonians at null infinity,” Journal of Mathematical Physics **23** no. 12, (1982) 2410–2417.
- [37] A. D. Helfer, “Angular momentum of isolated systems,” General Relativity and Gravitation **39** no. 12, (2007) 2125–2147.
- [38] R. Penrose, “Quasi-local mass and angular momentum in general relativity,” Proceedings of the Royal Society of London A **381** no. 1780, (1982) 53–63.
- [39] A. I. Nesterov, “Quasigroups, asymptotic symmetries, and conservation laws in general relativity,” Phys. Rev. D **56** no. 12, (1997) R7498.
- [40] N. Bishop and S. Deshingkar, “New approach to calculating the news,” Phys. Rev. D. **68** (2003) 024031.
- [41] N. T. Bishop and C. Reisswig, “The gravitational wave strain in the characteristic formalism of numerical relativity,” Gen. Rel. Grav. **46** (2014) 1843.
- [42] M. Boyle, “Transformations of asymptotic gravitational-wave data,” Phys. Rev. D **93** (2016) 084031.
- [43] A. D. Helfer, “Estimating energy-momentum and angular momentum near null infinity,” Phys. Rev. D **81** (2010) 084001.
- [44] J. Winicour, “Newtonian gravity on the null cone,” J. Math. Phys. **1193** (1983) .
- [45] N. W. Taylor, M. Boyle, C. Reisswig, M. A. Scheel, T. Chu, L. E. Kidder, and B. Szilágyi, “Comparing gravitational waveform extrapolation to Cauchy-characteristic extraction in binary black hole simulations,” Phys. Rev. D **88** (Dec, 2013) 124010, [arXiv:1309.3605](https://arxiv.org/abs/1309.3605) [[gr-qc](https://arxiv.org/abs/1309.3605)]. <http://link.aps.org/doi/10.1103/PhysRevD.88.124010>.
- [46] A. H. Mroue, M. A. Scheel, B. Szilagy, H. P. Pfeiffer, M. Boyle, D. A. Hemberger, L. E. Kidder, G. Lovelace, S. Ossokine, N. W. Taylor, A. Zenginoglu, L. T. Buchman, T. Chu, E. Foley, M. Giesler, R. Owen, and S. A. Teukolsky, “A catalog of 174 binary black hole simulations for gravitational wave astronomy,” Phys. Rev. Lett. **111** (2013) 241104,

arXiv:1304.6077 [gr-qc].

will soon be merged with `master`. Early development exists on the `feature/Characteristic` branch. A graph of Spectral CCE's commit history by `chandmer` is shown in Fig. 6.

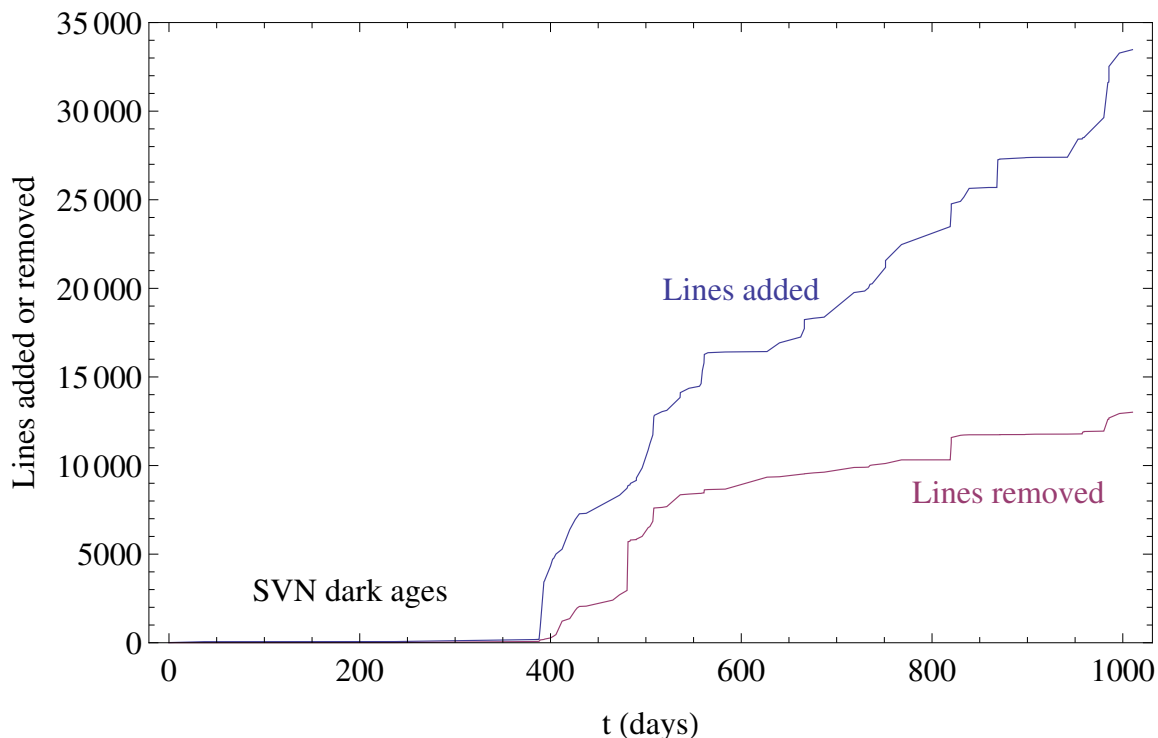


Figure 6: Graph showing history of commits by `chandmer` on various development branches of `SpEC`. Mean number of files per commit: 8.9. Mean line additions: 341.5. Mean line deletions: 132.8. A complete commit history before mid 2013 is not readily available due to version control migration from SVN to `git`.

```
As of September 22, 2016, the most recent git commit was
commit 2af43111da4e2bcb5c200eb7fb96de130f18a476
Author: Casey Handmer <chandmer@caltech.edu>
Date: Fri Sep 11 15:04:55 2015 -0700
Removed superfluous DataBox Items
```

The Spectral CCE code is completely documented and commented with up-to-date references to the relevant equations in the appropriate header files. All compute items can be found in the `Characteristic` directory, used by the driver located in the sub-directory `Tests`.

There is a convention in file nomenclature explained here.

1. `Characteristic*.pp` are compute items that perform hypersurface calculations of

β, Q, U, W , and J_u , according to their names. They operate in a 3D hollow sphere domain composed of the spinsfast grid (with a point on the pole) and a radial interval, typically composed of GaussChebyshevLobatto basis functions.

2. `CharacteristicBoundary*.pp` are compute items that perform calculations on the worldtube. They translate worldtube data from the Cauchy to the Bondi frame. Essentially, they provide an inner boundary condition. These calculations are performed on the spherepack grid, which does not have a point on the pole, before being transformed.
3. `CharacteristicScri*.pp` are compute items and functions that operate at the outer boundary, typically on the spherepack grid. There are also some projection helper compute items that perform changes of basis function.
4. `CharacteristicVol*.pp` are all compute items that transform quantities from the spinsfast to the spherepack grid throughout the domain.
5. `CharacteristicInertial*.pp` are compute items that perform calculations in and related to the inertial coordinate system at \mathcal{I}^+

Additionally, a basic convention allows the description of co- and contravariant tensors in `ascii` font. For example, `MCA` means a Metric in the Cauchy frame that is `contrA`variant. Similarly, `Mconf0d` would be the *derivatives* of a *conformal* Metric that is `cO`variant. In `SpEC`, this would be encoded as a `Tensor<Tensor<DataMesh> >`. Naturally, all compute items' header (`.hpp`) files contain a complete description of the item, its properties, and references to relevant equations in papers.

Chapter 7 – Avenues of future research

At the time of thesis submission, some avenues of future work of varying levels of difficulty exist.

- Flux. While the formalism for the flux was recently completed (at the time of writing) and a complete and convergent implementation exists, further optimization is likely possible.
- MultiVars. A more complete integration with SpEC would use the new MultiVars capability to run CCE simultaneously with the SpEC Cauchy evolution. MultiVars could also evolve ω , the inertial coordinates $x^{\tilde{A}}$, and the fluxes F_{ξ} rather than using the current Variable Step Explicit (VSEX) method in the driver.
- Matching. With simultaneous evolution enabled by MultiVars, the obvious next step is an open boundary condition, or characteristic matching. Matching would enable the dynamical alteration of the worldtube boundary, which will help to deal with initial conditions, junk radiation, and potentially greatly reduce the computational cost of computing the “induction” zone in the Cauchy evolution.

Matching will require some additional formalism beyond reverse engineering the inner boundary algorithm presented in Chapter 3.

Appendix A – Fourier Continuation in SpEC

During 2011 and 2012, I implemented and used a new basis function in SpEC called Fourier Continuation (FC). Developed primarily at the Caltech Applied Math department by Oscar Bruno and his group, Fourier Continuation is a spectrally accurate basis function with the attractive property of evenly spaced gridpoints, allowing a relaxed CFL condition.

By April 2012, it was apparent that SpEC had already abstracted the drawbacks FC was designed to address, and I discontinued its use. It remains an attractive solution for different sorts of problems and may be useful in particular for future simulations that deal with matter. Here, I include a basic description of its properties, method, and implementation in SpEC.

What is FC?

Casey Handmer

January 2012

1 Introduction

This document is written as a companion to and explanation of header notes found in the FC source code in SpEC. As of January 2012, the FC routine was contained within the file

```
Spectral/BasisFunctions/FourierContinuationFftw.*pp
```

in the SpEC repository.

First and foremost, FC stands for Fourier Continuation, a family of relatively new, versatile, and powerful spectral techniques that are finding broad applications in numerical PDE solving. Their primary advantages are $\mathcal{O}(N \log N)$ speeds in calculus operations, equidistant point spacing (and thus relaxed CFL conditions), and their applicability to non-periodic, non-rectangular domains without sacrificing stability.

As the FC method has been modified to work better with SpEC, the remainder of this document explains how and why.

2 Obtaining the FC spectrum as applied in SpEC

Step one in any spectral method is understanding how to transform function values on collocation points in physical space to coefficients in spectral space (phys2spec)

and back again (spec2phys). As the current `SpEC` architecture is restricted to real valued spectral (and physical) quantities, I implemented FC using the Discrete Sine Transform Type IV (DST-IV) and Discrete Cosine Transform Type IV (DCT-IV) transforms wherever appropriate. These transforms, which are special cases of the Fast Fourier Transform (FFT), are their own inverse; however, applying a derivative (or anti-derivative) operation necessitates switching between the two. For reference, their explicit form as implemented in `fftw3`[5] is

$$u_s = 2 \sum_{r=0}^{n-1} u_r \sin \pi/n(r + 1/2)(s + 1/2) ,$$

$$u_s = 2 \sum_{r=0}^{n-1} u_r \cos \pi/n(r + 1/2)(s + 1/2) .$$

Once in spectral form, the derivative or integral may be obtained almost trivially, as explained below.

As stated, however, this transform is useful only for “periodic” domains. The quotation marks are present as the DS/CT-IV transforms actually correspond to functions on a quarter period of the fundamental basis element, and so the periodicity condition instead takes the form that the function has odd symmetry at its left boundary and even symmetry on its right boundary for the DST, and vice versa for the DCT. In either case, or with the more traditional FFT, a function that fails the periodicity condition will not be preserved through the application of `phys2spec`→`spec2phys`, due to the Gibbs phenomenon. In all variants of the FC method as applied to non-periodic functions, then, some method is used to generate a periodic function that can be transformed without rapidly varying ringing at either end of the domain.

For these purposes the extension matrix \mathbf{Q} is applied. This matrix is pictured in Figure 2.

In `SpEC`, \mathbf{Q} is a 6×38 matrix comprising \mathbf{I}_6 , a 6×26 central part that blends each canonical basis vector to zero, and a 6×6 matrix of zeroes. Calculating this matrix is a non-trivial exercise explained in Section 3. For now, we merely assume its existence and explain its properties.

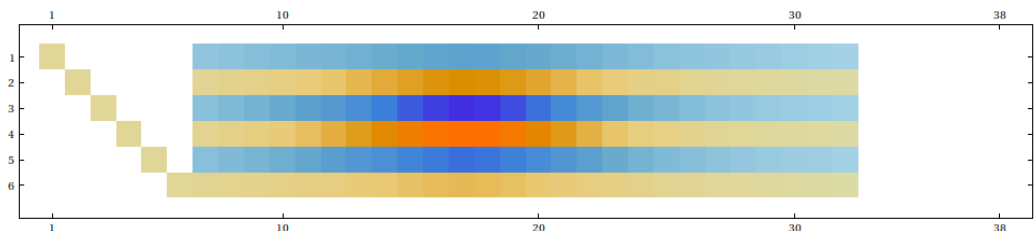


Figure 1: Matrix plot of \mathbf{Q} , the FC extension matrix.

\mathbf{Q} takes any 6 points (nominally consisting of the right hand end of some set of collocation values) and smoothly blends it to zero. Thus applied to either end of an arbitrary set of $n > 6$ collocation values, \mathbf{Q} generates a periodic function to order 6. Higher order \mathbf{Q} matrices are possible, but can lead to instabilities.

In `SpEC`, the DST-IV transform forms the backbone of the method. Thus the extended right end of the collocation points is added to its reverse to make a boundary with even symmetry, and the extended left end of the collocation points is added to the negative of its reverse to create a boundary with odd symmetry. Since the crux of both boundaries necessarily occurs in the middle of the extended region, only 13 points are needed from either end to achieve the desired effect. Thus, the application of the extension algorithm increases the size of the spectral function values by 26 points.

Upon the operation `spec2phys`, these additional points are simply snipped off at either end to return to the original domain. Note that in the `SpEC` implementation of FC, `phys2spec` refers to the DST-IV transform, while `spec2phys` refers to the DCT-IV transform. This means that in the event of an even number of calculus operations, such as the identity or the second derivative, the `phys2spec` function is applied to perform the `spec2phys` operation. To avoid confusion, these operations are referred to by their transform name explicitly.

2.1 Derivative operator

The derivative operator in SpEC is illustrative of the whole system in general, so most of the detail will be included here. The algorithm is:

1. extend collocation values
2. phys2spec (DST-IV)
3. filter (optional for linear ODE/PDE solving)
4. differentiate
5. spec2phys (DCT-IV)
6. truncate to return to original domain

2.1.1 The differentiation function

Obtained via the differentiation of the sine basis, and thus motivating the DCT-IV inverse transform. The normalising factor missing from the fftw3 implementation of the DS/CT-IV transforms, $(2(n + 26))^{-1}$, is also included in this step:

$$df_k[i] = f_k[i] \pi \frac{i + 1/2}{2(n + 26)} \frac{n - 1}{n + 26},$$

where i runs from 0 to $n + 25$. The last fraction term is included to correct for the extension of the domain in spectral space.

2.1.2 The filter function

The filter function ensures stability in nonlinear PDE solving by filtering out poorly resolved noise at high frequencies. In SpEC, it takes the form

$$f_{kfil}[i] = f_k[i] \exp\left(-\alpha \left(\frac{i}{n + 25}\right)^p\right),$$

where $\alpha = 16 \log 10$ and $p = 50$; these values taken from analysis and experimentation are reported in [1] and found to work.

2.2 Second derivative

In `SpEC`, the second derivative operator returns the first derivative as well. The only difference worth noting from the first derivative operator is that the inverse transform for the second derivative is a second application of the DST-IV transform, rather than the DCT-IV used for the first derivative and integral operations. The multiplicative factor used is

$$ddf_k[i] = -f_k[i] \frac{1}{2(n+26)} \left(\frac{\pi(i+1/2)(n-1)}{(n+26)} \right)^2,$$

where, once again, i runs from 0 to $n+25$.

2.3 Integral operator

The integral operator is identical to the derivative operator, and the multiplicative factor is

$$intf_k[i] = -f_k[i] \frac{1}{2(n+26)\pi(i+1/2)} \frac{n+26}{n-1},$$

which is effectively the inverse of the derivative operator! Note that the resulting integral is not normalised, so in `SpEC` the left most value is subtracted from the array such that the value at each point x_i is equivalent to the definite integral of the function from 0 to x_i .

3 Obtaining the matrix \mathbf{Q}

The extension matrix \mathbf{Q} is based on Gram polynomials[4, 6]. Without getting into too much theory, I'm going to give a recipe for its construction, generalisable to arbitrary order, m . Although my construction was somewhat more involved, the method I give here is equally valid.

We begin by constructing the Gram polynomials of order m . They are an orthonormal discrete polynomial basis defined by the usual inner product. Thus the first order is always a vector $\{1/m, 1/m, 1/m \dots\}$ of length m . The discrete values

are defined by the values taken by the continuous polynomials at each of the m discretisation points. For the remainder of this section, the continuous functions will be referred to by $G_i(x)$, where i indexes the order of the Gram polynomial.

Next, we construct a family of trigonometric functions that are periodic on some interval $D > 2 \times (M - m)$, where M is the desired length of the extension matrix \mathbf{Q} . If desired these can be designated even or odd and phase shifted to coincide with the even/odd center of the Gram polynomials they will eventually mimic. In general these functions are not taken to order D ; rather, their order K is minimised to prevent rapidly varying oscillations, which over-resolve the behaviour we are looking for.

We define a set of points to be matched by the trigonometric functions. This is composed of the $G_i(x)$ oversampled by a factor l within their natural domain $[0, 1]$, and a similarly oversampled list of zeros corresponding to the points $M - m + 1$ to M at the other end of our nascent \mathbf{Q} . These values form a rectangular matrix \mathbf{m} of size $m \times (2lm + 2)$.

Next, we sample the periodic trigonometric (incomplete) basis at each point corresponding to the long side of our oversampled matrix \mathbf{m} , and for each individual trig basis element, yielding a matrix \mathbf{A} of size $2K \times (2lm + 2)$.

Applying Singular Value Decomposition between \mathbf{A} and \mathbf{m} yields a matrix of size $2K \times m$; this is a set of coefficients that, when applied to the trigonometric basis function, gives a set of m highly accurate, smooth functions which take each $G_i(x)$ Gram polynomial and blends it to zero. Note that this is best done using a symbolic algebra program to extremely high precision (> 50 digits), or else the whole exercise is basically pointless.

The trig function is sampled at each point in its domain of length D to give a matrix of size $D \times m$. This matrix is multiplied by the (inverse of the) original $m \times m$ Gram basis matrix to convert the fitted Gram polynomials on the left hand edge to the identity matrix.

Finally, the matrix is truncated to length M as desired, and should now have the

same general character as the matrix in Figure 2, with an identity segment, a curvey segment, and a zero segment. This is the extension matrix \mathbf{Q} .

3.1 MCMC optimisation, testing

One aspect I glossed over above is the choice of m , M , K , D , and l , as well as other optional parameters a sufficiently enthusiastic person could dream up. Already there is a rather slow step (SVD), a high dimensional parameter space, and no obvious figure of merit.

To cut to the chase, the parameters that are used in the current version of FC in SpEC are

$$m = 6, M = 38, K = 24, D = 68, l = 7.$$

To give you an idea of how discretisation can mess up the optimisation process, the second best set of parameters I found was

$$m = 6, M = 38, K = 25, D = 74, l = 37!$$

Although I experimented with a number of direct optimisation methods that used steepest descent, the most efficient implementation came from my favourite pet problem smasher, an MCMC approach using the Metropolis-Hastings (MH) “Good enough while you sleep” algorithm[7].

For those who lack access to google, a summary of the MH algorithm is presented here.

1. initialise $params$, $cost$, and anything else that it needs.
2. augment $params$ with a small random increment; $paramstar = params + random$.
3. evaluate $coststar(paramstar)$.
4. perform evaluation $cost/coststar < random(0,1)$,
if *true*, $params = paramstar$, $cost = coststar$.

5. loop over 2-4 until optimal condition is found.

Obviously, this routine will minimise the cost. Variants which maximise cost are not too difficult to imagine. It is also customary to have a step to save the “best yet” parameter set, as the chain can and does wander quite far from the optimal solution. One primary difficulty in setting up the MH algorithm is choice of appropriate *paramstar* trials. In general some percentage change on the existing parameters is a good way to regulate step size. For calculating \mathbf{Q} , all the parameters are discrete, so it’s not such a big issue. Similarly, the range of the random numbers used in step 4 can be modified, depending on how confident you are that local minima or maxima do not present problems.

The largest non-triviality of any MH optimisation algorithm, however, is determining how to condense all the details down to a single cost. Experimentation revealed that integration always worked better than differentiation, so my cost function focused on the first derivative operator as outlined above. To begin with, I calculated the exact value of the function and first derivative of $G_i(x)$ on the domain $[0, 1]$ divided into 6 to 12 (m to $2m$) discretization points, forming two arrays comprising 324 function and derivative values on 42 different test domains. The FC derivative operator was applied to each of the 42 test domains and the largest absolute error returned, forming the cost function. My reasoning was that the Gram polynomials formed a natural basis on which to test the derivative operator, and that over-sampling them was an efficient way of testing the accuracy of the algorithm for small numbers of points. In general, the accuracy of the FC derivative operator is spectral within the domain and $m - 1^{th}$ on the outer m boundary values[1], so smaller domains are more likely to be problematic. It is also similar to the tests used within SpEC.

This cost function proved the most versatile of the variations I tried, and was eventually minimised to $\mathcal{O}(10^{-9})$ for the largest error on the domain.

In general the optimiser was run until no further improvements occurred. The number of steps taken to reach this level varies depending on the problem from tens

to tens of millions. Fortunately the MH algorithm generalises to higher dimensional parameter spaces very efficiently.

4 Multiple domains, sub-patches, optimised performance

Parallisation is readily achieved within FC by subdividing the domain into separate regions (not necessarily rectangular or even regular) and passing each domain to a different processor. Boundary information is passed by ghost zones (not yet implemented for FC in SpEC), in which the outer 3 points of any given subdomain are drawn from the interior of an adjacent subdomain, to generate a “common” zone of 6 points. The passing of ghost zone point value information can be made efficient if each axis is passed in turn. Other implementations use up to 12 points to accurately transmit internal data. It is not known if SpEC requires that level of precision. It is known that implicit time stepping lends greater stability to the evolution, permitting narrower common volumes between subdomains.

According to analysis carried out in [1], extremely large domains on a single processor benefit from further subdivision into “sub-patches”. Appropriate implementation of sub-patches is theorised to reduce the FC cost from $\mathcal{O}(N\log N)$ per dimension to $\mathcal{O}(N)$. Analysis suggests the maximum efficient size of a sub-patch domain with a \mathbf{Q} matrix of length 38 is 210 points. A 3D domain of linear length 210 is extremely large for SpEC, however, so this will probably remain in the realm of speculation.

As in most spectral methods, higher dimensional application of the FC algorithm performs derivatives along each axis sequentially. If filtering of the base data is required, this sequential differentiation remains the most efficient way to implement it.

4.1 External and internal domain boundary conditions, overlaps, etc

In `SpEC`, FC(6) is the only currently implemented form of the FC algorithm. Therefore both external and internal (i.e., subdomain) boundaries are of length 6, though other lengths appear in the literature. For boundaries, BCs are ideally satisfied by injection, though currently `SpEC` uses Bjørhus conditions[3]. For internal domain boundaries, information is carried across through the use of ghost zones, currently implemented in the Hydro part of `SpEC`, but not tested with FC. In this case, the 3 point deep outer most layer of each computational subdomain is extended with an exterior 3 point deep layer drawn from adjacent subdomains to ensure high accuracy near the boundary.

5 Explicit time stepping? Implicit time stepping?

For explicit 4th order Adams-Bashforth (AB4) [2] time-stepping, [1] has shown a CFL condition of $\Delta t = 0.136\Delta x$. All indications are that 4th order Runge-Kutta (RK4) explicit time-stepping is similar.

The CFL condition places a limit on the largest time step (and thus overall speed) possible when simulating hyperbolic systems, based on the smallest spacing of collocation points Δx_{min} . As FC's points are equidistantly spaced, the CFL condition is optimal.

Chebyshev-Gauss-Lobatto (CGL) basis functions are a very popular, polynomial-based spectral method. Like many polynomial-based spectral methods, CGL uses unequally spaced points, so that $\Delta x \propto N^{-2}$. As a result, for domains with large numbers of points N , the CFL condition scales sub-optimally as N^2 , rather than FC's N .

This issue is addressed in `SpEC` by the use of lots of smaller subdomains. For larger domains, these incur a developmental and computational overhead that favor the use

of FC. For smaller domains, FC's 26 extra spectral points consume computational resources, disfavoring the method.

Although SpEC uses explicit RK4 time stepping, FC has been successfully demonstrated with both implicit and explicit methods, and thus possesses the needed versatility should the time stepping system be changed.

6 Conclusion – May 2015

Although the FC method is a powerful new method for solving PDEs, we found that its principal strengths (low dispersion, stability, relaxed CFL condition) were not strongly required for spectral CCE. In particular, spectral CCE did not require a large radial domain. In comparison testing, we found CGL methods were more accurate and no slower, and switched to using them for the remainder of the project.

References

- [1] Albin, Nathan, and Oscar P. Bruno. *A spectral FC solver for the compressible Navier-Stokes equations in general domains I: Explicit time-stepping*. Journal of Computational Physics **230** (2011) pp. 6248-6270.
- [2] Bashforth, Francis. *An Attempt to test the Theories of Capillary Action by comparing the theoretical and measured forms of drops of fluid. With an explanation of the method of integration employed in constructing the tables which give the theoretical forms of such drops, by J. C. Adams*. Cambridge University Press. 1883.
- [3] Bjørhus, Morten. *The ODE Formulation of Hyperbolic PDEs Discretized by the Spectral Collocation Method*. SIAM Journal of Scientific Computing **16** (3) (1995) pp. 542-557.

- [4] Chebyshev, Pafnuty. *Sur l'interpolation*. Zapiski Akademii Nauk **4** (1) (1864) pp. 539-560.
- [5] Frigo, Matteo, and Steven G. Johnson. *The design and implementation of FFTW3*. Proceedings of the IEEE **93** (2) (2005) pp. 216-231.
- [6] Gram, Jørgen P. *Ueber die Entwicklung reeller Functionen in Reihen mittelst der Methode der kleinsten Quadrate*. Journal für die reine und angewandte Mathematik **94** (1883) pp. 41-73.
- [7] Gregory, Phil. *Bayesian Logical Data Analysis for the Physical Sciences*. Cambridge University Press. 2005.

FINIS